Determination of the signaling pathways and subcellular targets in response to nanosecond pulsed electric fields

Lynn Carr

Thèse de doctorat

Université de Limoges

Université de Limoges

École Doctorale Bio-Santé (ED 524)

Faculté des Sciences et Techniques - XLIM Equipe BioEM

Thèse pour obtenir le grade de

Docteur de l'Université de Limoges

Discipline : Biologie, médecine et santé

Présentée et soutenue par

Lynn Carr

Le 15 décembre 2016

Determination of the signaling pathways and subcellular targets in response to nanosecond pulsed electric fields

Thèse dirigée par Rodney O'Connor et co-dirigée par Sylvia M. Bardet

JURY :

Rapporteurs :

Mme. Marie Pierre ROLS	**Directeur de Recherche CNRS** Université de Toulouse – Laboratoire IPBS-CNRS UMR 5089
M. Michal CIFRA	**Professeur** Czech Academy of Sciences – Bioelectrodynamics Research Team – Institute of Photonics and Electronics, Prague

Examinateurs :

M. Michel MALLAT	**Directeur de Recherche INSERM** Hôpital de la Salpêtrière – INSERM U 1127 – Paris
M. Yann PERCHERANCIER	**Chargé de Recherche CNRS** Université de Bordeaux – Equipe BioEM – IMS – UMR 5218
M. Philippe LEVEQUE	**Directeur de Recherche CNRS** Université de Limoges – Equipe BioEM – XLIM – UMR 7252

Encadrants :

M. Rodney O'CONNOR	**Enseignant - Chercheur** Ecoles des Mines de Saint-Etienne
Mme. Sylvia BARDET	**Maître de Conférences** Université de Limoges – Equipe BioEM – XLIM – UMR 7252

Dedicated to my amazing Mum and Dad – thank you for all your support, good advice and love xx

In loving memory of Annie – always loved and always missed

With thanks to everyone who has contributed to this thesis by sharing their scientific knowledge and by giving their practical help or emotional support

TABLE OF FIGURES :

Abbreviations

$[Ca^{2+}]_i$:	Intracellular Ca^{2+} concentration
$\Delta\Psi_m$:	Mitochondrial membrane potential
3D-SIM:	3D structured illumination microscopy
CaViar:	Dual function Ca^{2+} and voltage reporter
CCE:	Capacitative calcium entry
CICR:	Calcium induced calcium release
CsA:	Cyclosporine A
EB3:	End-binding protein 3
EGTA:	Ethylene glycol-bis(2-aminoethylether)-N,N,N′,N′-tetraacetic acid
EP:	Electric pulses
ER:	Endoplasmic reticulum
GBM:	Glioblastoma multiforme
GECI:	Genetically encoded calcium indicator
GFP:	Green fluorescent protein
HBSS:	Hank's balanced salt solution
IP_3:	Inositol-1,4,5-trisphosphate
IP_3R:	Inositol-1,4,5-trisphosphate receptor
MAP:	Microtubule associating protein
mPTP:	Mitochondrial permeability pore
MT:	Microtubules
MTOC:	Microtubule-organising centre
nsPEF:	Nanosecond pulsed electric field
P2X7R:	P2X7 receptor
PARP:	Poly ADP ribose polymerase
PI:	Propidium iodide
PIP_2:	Phosphatidylinositol-4,5-bisphosphate
PLC:	Phospholipase C
PLD:	Phospholipase D
PM:	Plasma membrane
PS:	Phosphatidylserine
RFP:	Red fluorescent protein
ROI:	Region of interest
SERCA:	Sarcoplasmic/endoplasmic reticulum Ca2+-ATPase
TMRE:	Tetramethylrhodamine, ethyl ester
TRP:	Transient receptor potential channel
VDAC:	Voltage-dependant anion channel

Chapter 1:

General introduction

1. General Introduction

1.1. The cell's membranes

Eukaryotic cells have both external and internal membranes. The external, or plasma, membrane encases the cell cytoplasm whilst the internal membranes surround the various intracellular organelles. These membranes are vital in controlling what passes into and out of both the cell and its organelles.

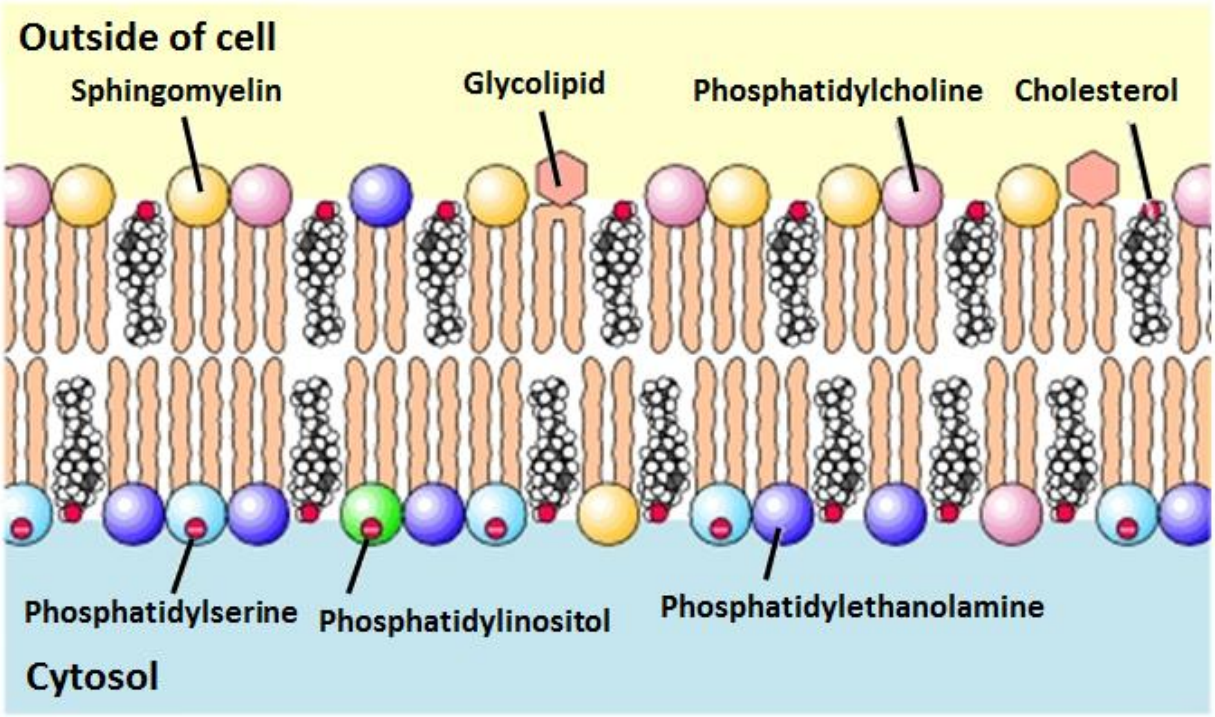

Figure 1. Lipids of the plasma membrane.

The cells plasma membrane is made up of five different phospholipids. Their hydrophobic tails are buried into the membrane with their hydrophilic head groups facing the aqueous cytosol or extracellular matrix. This arrangement forms a barrier between the outside of the cell and the inside. From Cooper, 2000[1].

The main structure of the membranes is a phospholipid bilayer, which is around 5 nm thick, into which many proteins are inserted that have numerous roles including molecule recognition, activation of cellular signalling and transmembrane transportation, as shown in Figure 2. The plasma membrane (PM) contains five major phospholipids: phosphatidylcholine, phosphatidylserine, phosphatidylethanolamine, sphingomyelin and phosphatidylinositol. As shown in Figure 1 these phospholipids have an asymmetric distribution, the negative charge of the head groups of phosphatidylserine and

phosphatidylinositol results in the cytosolic facing side of the PM having a negative charge. Cholesterol is also an important membrane component, regulating temperature based permeability to small molecules[1]. Glycolipids are also found on both the PM and the intracellular membranes, with around two-thirds being found on organelle membranes. They are made up of a sugar head group and a lipidic tail and play a role in cell-cell interactions, signal transduction and protein anchoring[2].

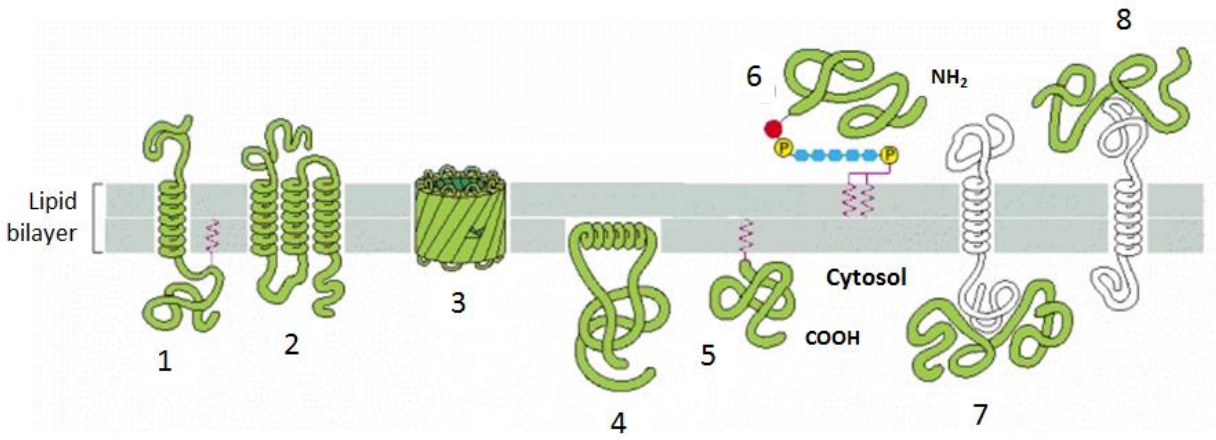

Figure 2. Different types of membrane associated proteins.

Proteins associate with the membrane in different ways. Transmembrane proteins (1,2,3) have a hydrophobic portion, usually α-helical, that inserts into the membrane with hydrophilic tails extending into both the extra and intracellular spaces. These proteins often play a role in transforming external stimuli into internal signals (for example G-protein coupled receptors) or as channels (3) (for example aquaporins). Others are anchored to the membrane by an α-helical domain (4) or by direct covalent attachment (5) or indirect attachment via an oligosaccharide linker (6) to a fatty acid. Others are bound by interaction with other membrane bound proteins (7,8). From Alberts *et al.* 2000[3].

1.2. The cell as an electric circuit

The cell can be considered as an electrical circuit with the plasma and organelle membranes acting as insulators and the extracellular media, the cytoplasm and the organelle interiors acting as conductive electrolytes (Figure 3). The cell membranes however are not perfect insulators due to the presence of protein channels and pumps. In the PM ion pumps transport ions against their concentration gradient, in an active process requiring ATP, to maintain

intracellular concentrations of Na^+, Ca^{2+} and Cl^- that are lower than the extracellular concentrations and a K^+ intracellular concentration that is higher than the extracellular concentration. In addition to the pumps, resting membranes also contain many open K^+ channels that allow the passive movement of potassium ions through the membrane from the inside outwards. This results in an accumulation of negative charge on the inside of the cell close to the membrane and a positive charge on the outside[4]. This difference in charge creates a difference in voltage across the membrane of between 50 and 70 mV.

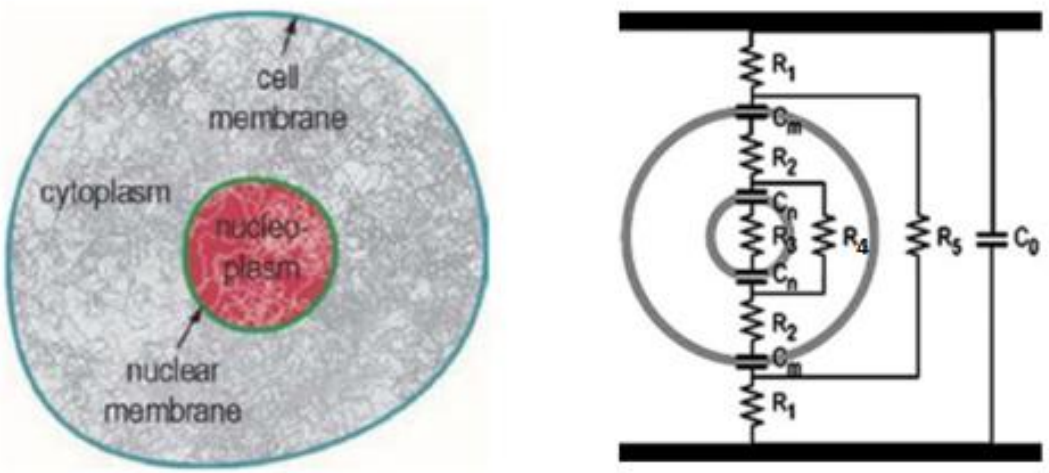

Figure 3. The cell as an electrical circuit.

Left shows a cross section of a cell as would be seen with light microscopy. Right is a model of the cell shown between two electrodes. The capacitance, or ability to store electrical charge, of the PM and the nuclear membrane are shown as C_m and C_n respectively and the total capacitance of the system as C_0. The resistance of the extracellular media, cytoplasm and nucleoplasm are shown as R_1, R_2 and R_3 respectively. R_5 is the total resistance of the cell. From Schoenbach *et al.* 2004[5].

1.3. Effect of an electric field on cell membranes

Exposure of a cell to an external electrical field results in a redistribution of charge within the cell and its accumulation in the membrane as shown in Figure 4. Where the electrical field has its strongest effect is described by Schwan's equation (Figure 5). This accumulation of charge causes an induced transmembrane voltage that is superimposed onto the resting transmembrane voltage. Increased transmembrane voltage leads to the opening of voltage gated channels and when the transmembrane voltage is in excess of 200-300 mV structural rearrangements and breakdowns of the membrane occur resulting in the formation of pores[6].

Whether these pores persist or reseal is dependent on the magnitude and the duration of the induced transmembrane voltage. This has been termed electroporation.

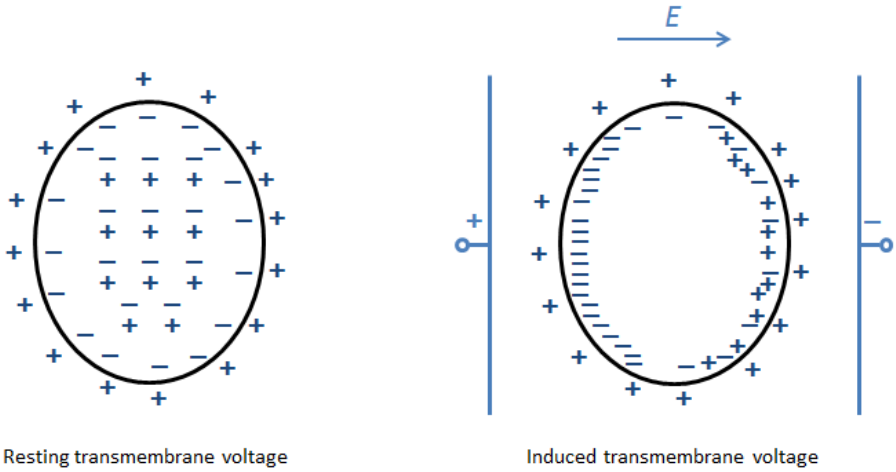

Figure 4. Effect of an electric field on the resting transmembrane voltage.

The resting transmembrane voltage is due to an ionic imbalance between the extra and intracellular environment that results in an accumulation of negative charge on the inside of the cell close to the membrane and a positive charge on the outside. Applying an electric field causes a redistribution of charge within the cell that gives an induced transmembrane voltage that is superimposed onto the resting transmembrane voltage. Adapted from Puchihar *et al.* 2009[7].

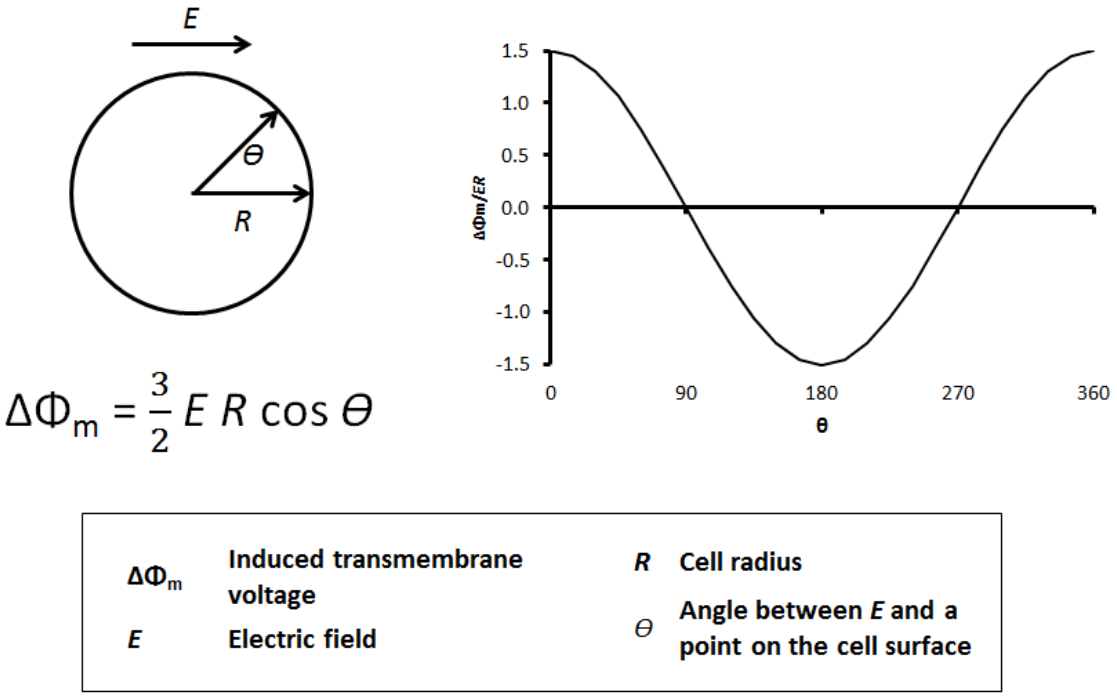

Figure 5. Schwan's equation.

Schwan's equation states that voltage is proportional to the cell's radius and the applied electric field. It has maximal and minimal effects where the membrane is perpendicular with the field (θ = 0° and 180°) and in between these points it varies proportionally to the cosine of θ. Schwan's equation is only strictly true for a spherical cell, for more complex cells, like those used in our experiments, more complex models have to be applied.

1.4. Clinical applications of electroporation

1.4.1. Electrochemotherapy

Electroporation has been exploited for several clinical applications. Its use in the treatment of cancer has been in practice for several decades, in the form of electrochemotherapy, with the results of the first clinical trial published in 1993[8]. In electrochemotherapy highly cytotoxic drugs that have low cell membrane permeability, such as bleomycin[9] and cisplatin[10], are introduced into cancerous cells by the pores formed during electroporation. To do this the drug is injected into the tumour and either needle[8] or plate[10] electrodes are placed in or around the area to be treated and pulses of µs duration, with an electric field strength of 1.2-1.3 kV/cm are applied. As the drugs used are largely impermeable to non-electroporated cells the result is a localised treatment with side-effects that are much reduced when compared to systemic chemotherapy treatments. The development of a commercialised pulsing system, the

Cliniporator sold in Europe by IGEA (Italy), and a standard operating procedure[11] has led to an increase in the availability of this treatment to patients.

1.4.2. Electrogenetherapy

Electroporation is widely used in the laboratory to introduce DNA into cells, via the permeabilised PM, during transfection. This technique is also being developed for use as a therapeutic treatment called electrogenetherapy. The idea behind electrogenetherapy is that the foreign DNA that is inserted into the cells integrates with the patient's DNA and is expressed to produce a protein that was lacking in, or is beneficial to, the patient. Examples of electrogenetherapy treatments that are in the *in vivo* stage of development include: the expression of a protein that neutralises inflammatory tumour necrosis factor-α in rheumatoid arthritis[12]; the expression of proteins, by tumour cells, that activate an immune response against the tumour[13]; and the expression of a protein that protects motor neurons from ischemic death in Amyotrophic lateral sclerosis[14]. It has also been trialled in humans for the treatment of melanoma[15].

1.5. nsPEF verses other PEF

Whilst electrochemotherapy and electrogenetherapy use electric pulses of µs duration increasing interest is being shown for shorter pulses of ns duration. These nanosecond pulsed electric fields (nsPEF) generally have a pulse duration of between 1-300 ns, an electric field strength of 10-100 kV/cm[16] and are generally considered as non-thermal. When applied to cells *in vitro* they have been shown to induce cell death that is widely believed to follow an apoptotic pathway, whereas longer pulses of the same intensity (µs-ms) result in cell death via necrosis (Figure 6). Research in the field focuses largely on the application of nsPEF as a treatment for cancer. Work in both animal models and humans has shown that nsPEF can reduce the size of tumours[17–19], whilst also stimulating an immune response against the cancer cells[20].

Similar to longer pulses nsPEF has an effect on the cell's PM with the formation of nanometre sized pores, nanopores, that are much smaller than those created by longer pulses[21,22]. Unlike other PEF, nsPEF is also able to cause poration of organelle membranes[23] such as the mitochondria resulting in their depolarisation[22,24] (Figure 7). Other reported effects of nsPEF include: phosphatidylserine (PS) externalisation[25], cytochrome C release from the

mitochondria[26], cleavage of poly ADP ribose polymerase (PARP)[27], DNA fragmentation[28]; caspase activation[21,27–30] and transient spikes in intracellular calcium concentrations[31–33].

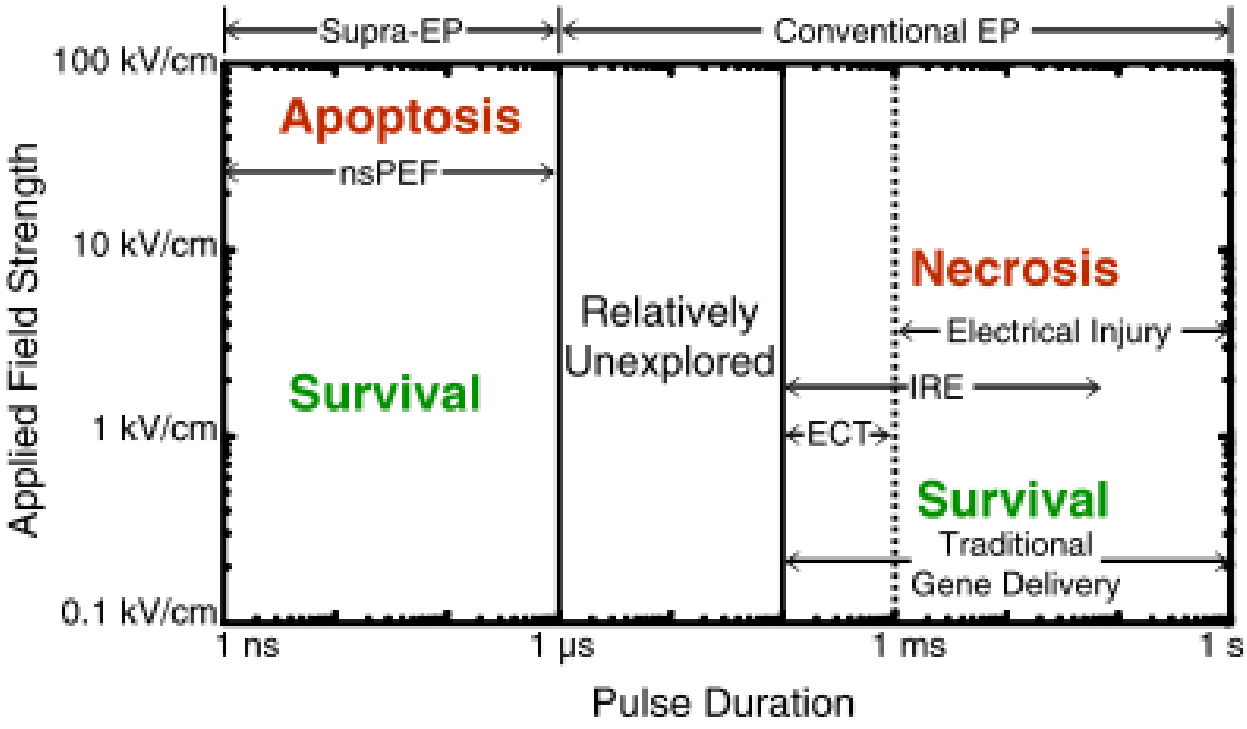

Figure 6. Comparison between the effects of electric pulse strength and duration on cell survival.

Both nsPEF and conventional electric pulses (EP) cause cell death, by apoptosis and necrosis respectively, if applied at high enough field strengths. Lower field strength conventional EPs are used for electrochemotherapy (ECT) and reversible and irreversible electroporation (IRE). From Weaver *et al.*[34].

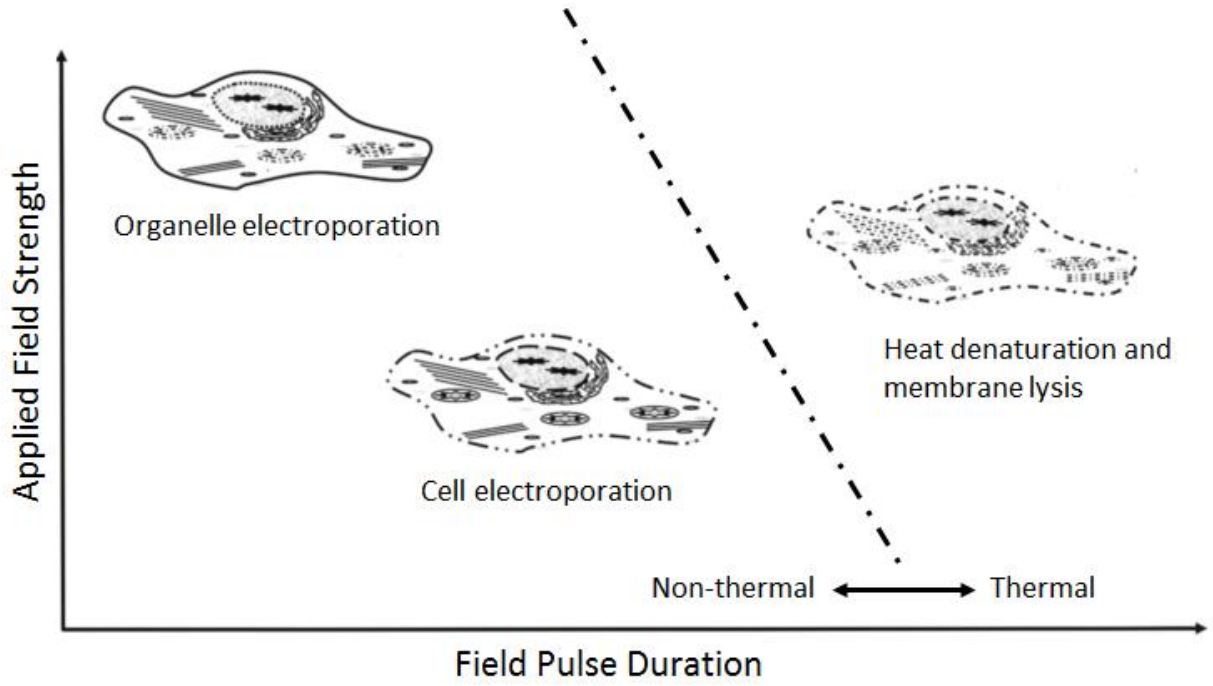

Figure 7. Effect of pulse strength and duration on temperature change and its cellular impact.

When applied to cells non-thermal nsPEF results in the poration of organelles. Longer, low field strength pulses result in the electroporation of the cells membrane, whereas longer, higher field strength pulses have a thermal effect leading to denaturation and lysis of the cell. From Lee[6].

1.6. nsPEF generator setup

In the BioEPIX lab at XLIM we use an nsPEF generator that delivers 10 ns pulses, with adjustable amplitudes from 4.5 kV to 10 kV and a rise time of 2 ns. The pulse is delivered via a coaxial cable with delivery and pulse parameters confirmed by display on an oscilloscope. A 50Ω load is attached to the delivery device to match the output impedance of the generator (Figure 8).

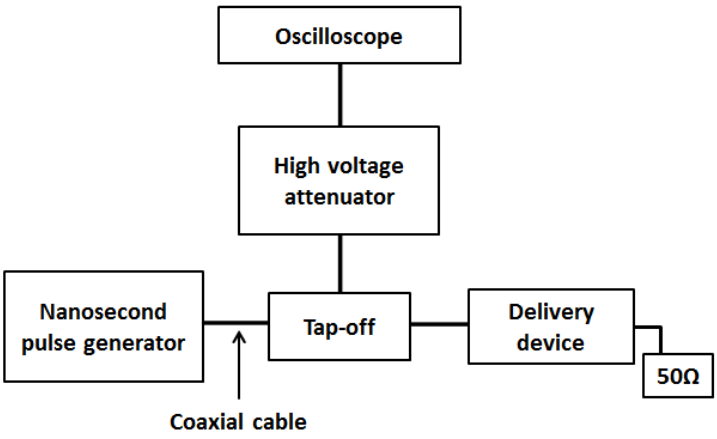

Figure 8. The nsPEF generator and pulse delivery setup.

For the work in this thesis two different nsPEF delivery devices were available. The first was a transverse electromagnetic (TEM) cell that had been adapted to deliver nsPEF and to allow real-time visualisation, by microscope of cells in a petri dish[35,36] and the second consisted of positionable, steel electrodes that could be lowered into the imaging dish[37] (Figure 9). The steel electrode system was chosen as it was more adapted to future *in vivo* work envisaged by the lab. Numerical simulations showed that the cells in the area between the electrodes, which are monitored in real-time by microscope, have a fairly homogenous electric field distribution with amplitudes in the range of 35-45 kV/cm (Figure 10).

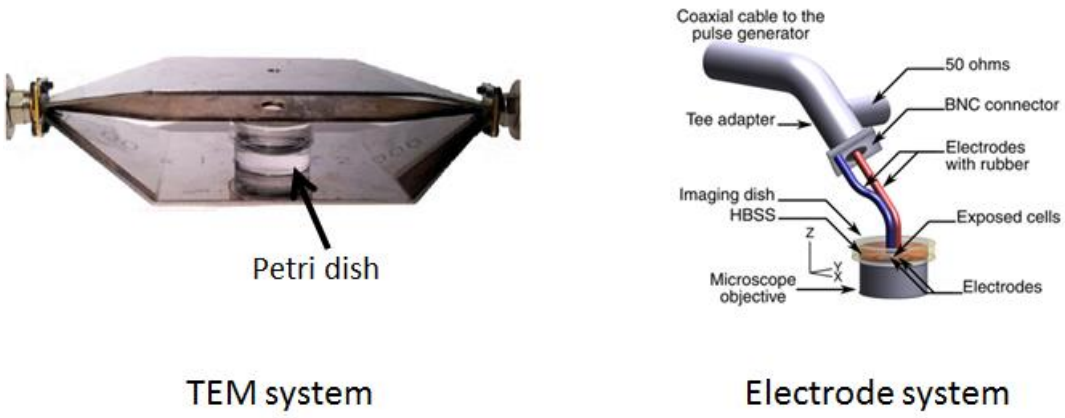

Figure 9. The two available nsPEF delivery devices.

An nsPEF delivery device based on a TEM cell and a steel electrode based device were both available for the work in this thesis. The electrode system was chosen for its suitability for future work.

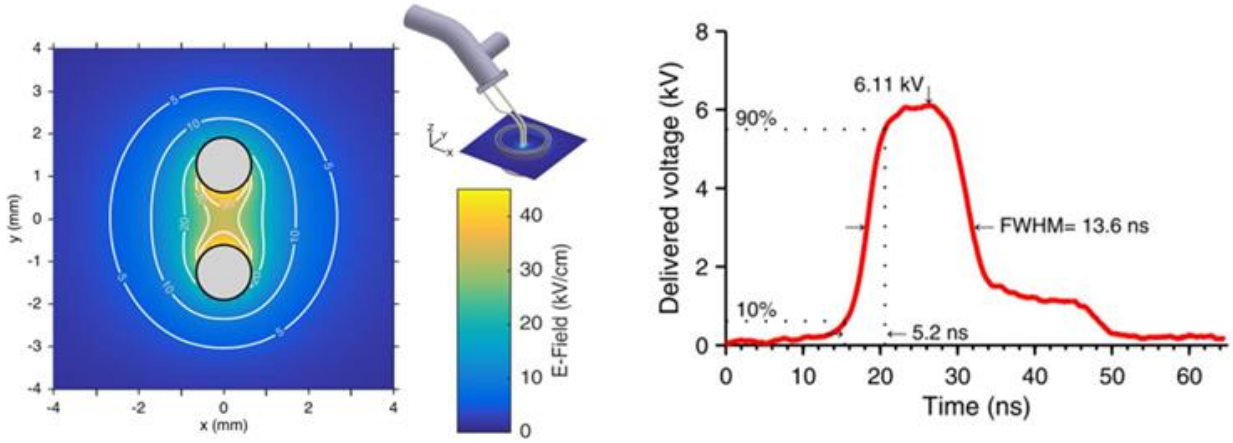

Figure 10. Dosimetry of the steel electrode system.

The image on the left is a numerical simulation showing the spatial distribution of the electric field magnitude between the electrodes immersed in the biological sample, at the level of the coverslip, for a 6.1 kV delivered pulse. The image on the right shows the time-domain pulse profile for the nsPEF used in this thesis with a 13.6-ns pulse full width at half magnitude (FWHM) duration with a 6.1 kV maximum amplitude, as measured by the oscilloscope.

1.7. nsPEF as a cancer treatment

nsPEF has been proposed as an alternative cancer treatment to chemotherapy[38]. Advantages of nsPEF over established chemical treatments include: focused rather than systemic treatment resulting in reduced side effects; treatment durations are short so the opportunity for resistant mutations to occur is reduced[39]; non-inflammatory cell death by apoptosis which occurs even in cells containing apoptosis evading mutations[30,40,41]; targets not only the fast dividing cancer cells but also the slower dividing cells of the tumour microenvironment thus reducing the chances of tumour recurrence and metastasis[39]; possible induction of an anti-tumour immune response[20].

Transition of the nsPEF technology from research into the clinic is being pioneered by the company Pulse Biosciences in Burlingame, California. They are currently targeting cancers of the skin with a completed human pilot trial showing promising results for treating basal cell carcinomas[19].

1.8. nsPEF as a potential treatment for glioblastoma multiforme

Glioblastoma multiforme (GBM) is a common and aggressive tumour of the glia affecting the central nervous system. It is highly invasive and resistant to all current treatments, with the median survival time for patients being 14.6 months[42]. Current standard treatment includes surgical resection, chemotherapy and radiotherapy[43]. Treatment of GBM, and other brain tumours, by electrochemotherapy is currently under investigation. Preclinical trials in rats with glioma suggest that the treatment is safe and effective with 9 out of the 13 treated rats showing tumour regression and disappearance[44]. A limited phase 1 trial in humans has also been undertaken[45].

Given the need for an effective GBM treatment and the encouraging results using electrochemotherapy our group at XLIM is interested in the application of nsPEF to GBM. My PhD work has focused on the *in vitro* effects of nsPEF on a human glioblastoma cell line (U87-MG) in a first step towards assessing its suitability as a treatment. Determining how nsPEF acts on a subcellular level, in glioblastoma cells, will hopefully lead to a greater understanding of how to optimise nsPEF dosing (number and strength of pulses and frequency of delivery) and, later, permit rational decisions to be made concerning the use of any adjuvant therapies.

Chapter 2:

General effects of nsPEF on U87-MG cells

2. General effects of nsPEF on U87-MG cells

2.1. Introduction

Many different effects of nsPEF on cells have been published which have recently been summarised in a systematic review by Napotnik *et al.*[46]. Comparing these effects between studies is however difficult as many different exposure systems, field strength, pulse duration, repetition rates and cell types are used. To date the studies involving glioblastoma are limited[47]. The work in this chapter aims to characterise the effects of our nsPEF exposure system on the U87-MG human glioblastoma cell line by looking at three of the main reported nsPEF effects: membrane permeabilisation, changes in intracellular calcium and loss of mitochondrial membrane potential.

2.1.1. Permeabilisation of the plasma membrane

An influx of cell membrane impermeable dyes has been used to show that nsPEF causes permeabilisation of the cell membrane. Whilst it is generally believed that nsPEF directly induces the formation of nanometre sized pores on the plasma membrane the possibility that trans-membrane protein channels are opened has also been investigated.

2.1.1.1. Nanoporation of the plasma membrane by nsPEF

Molecular dynamics simulations propose that the application of nsPEF to cells results in the formation of temporary nano-sized pores in the plasma membrane. They predict the formation of ion-conductive pores, on the anodic side of the cell, within 5-6 ns following pulse application[48–50]. Pore formation occurs in several steps. When exposed to an external electric field a voltage on the plasma membrane is induced. This voltage has the effect of lowering the energy needed for membrane lipid rearrangement[51]. As a result defects in the hydrophobic lipid layer can form when water, which due to its dipoles orientates in the electric field, applies pressure on the membrane. Water then extends into the membrane, with the hydrophilic lipid head group following the water to form the pore [52]. The formation of pores is dependent on field strength, pulse duration and repetition rate[53,54]. Pore size has been estimated as being 1 – 1.5 nm[55–57].

Nanoporation of the cell membrane has been studied experimentally by looking at the uptake of the membrane impermeable dyes propidium iodide (PI), YO-PRO-1 and Ethidium Homodimer-1 (EthD-1). Early work looking at nsPEF induced nanoporation using EthD-1 showed that nanoporation was a short lived event with pores remaining open less than 5

minutes following 3, 60 ns, 60 kV/cm pulses to the human T-lymphocyte cell line Jurkat. The extent of poration varied between cell types. Small cells, such as Jurkat, were shown to be the least resistant (15-fold increase of PI fluorescence in 70% of cells following 3, 60 ns pulses), with larger cells, such as monocytes, being more resistant (4-fold increase of PI fluorescence in 30% of cells following 3, 60 ns pulses)[26]. Further examination of Jurkat cells showed that increasing pulse duration, pulse number and/or electric field caused an increased uptake of EthD-1[17]. Pulse type has also been shown to affect the extent of nanoporation with a larger influx of PI and increased membrane instability seen with monopolar nsPEF than with bipolar nsPEF[58]. In contrast, other investigations studying Jurkat and human promyelocytic leukemia HL-60 cells have failed to show the uptake of PI following nsPEF treatment[32,33]. Here, the authors suggest that either the electric fields used in their experiments were too low to induce poration or that the pores formed were too small to allow uptake of PI. More recent experiments looking at uptake of extracellular Ca^{2+} and PI, following single 600 ns pulses, in N1-S1 rat hepatoma cells support these theories. Intracellular concentrations of Ca^{2+} (Van der Waals diameter = 0.462 nm[55]), which is smaller in size than PI (Van der Waals dimensions 0.78 x 1.62 x 1.39 nm[56]) were found to increase significantly for electric fields at and above 10 kV/cm, whereas significant PI increase was only observed for electric fields above 50 kV/cm [24]. YO-PRO-1 (dimensions 1.68 x 0.94 x 0.89 nm[59]), which is also smaller than PI, has been used to show the effect of pulse number on pore size in Jurkat cells. The application of 5 pulses (4 ns, 10mV/m, 1 kHz repetition rate) was enough to cause a significant uptake of YO-PRO-1, whereas 20 pulses needed to be applied to show a measurable increase in PI fluorescence[22]. The number of pores formed has also been linked to number of pulses with increasing numbers of 60 ns pulses causing increased uptake of both YO-PRO-1 and PI[57].

2.1.1.2. Opening of transmembrane pores by nsPEF

Nanoporation due to nsPEF treatment is experimentally assessed by the uptake of dyes that are impermeable to the plasma membrane. There are however several membrane receptor channels present on the cell that, upon activation, are able to gate the entry of these dyes into the cell. These include the P2X7 receptor (P2X7R) and members of the transient receptor potential (TRP) channels family. As such the activation of these channels by nsPEF has also to be considered as an alternative to nanoporation. In further support gadolinium which is known to block a range of ion channels, including certain TRP channels, also blocks nsPEF membrane permeabilisation[60].

The P2X7R, which is expressed on U87 cells[61], is a ligand gated cation channel located on the plasma membrane, whose functions include the regulation of membrane potential and intracellular calcium levels. Part of the P2 family of purinergic receptors it is activated by ATP, ADP, UTP and UDP[62]. Brief activation of P2X7R by ATP leads to the opening of an ion channel that allows the passage of mono and divalent cations (Na^+, K^+ and Ca^{2+}). A more prolonged activation leads to secondary permeability which is the formation of a pore that allows the uptake of larger cations including the fluorescent dye YO-PRO-1[63]. This secondary permeability has been linked to the coupling of activated P2X7R to pannexin-1[64]. Pannexin-1 is a transmembrane protein that oligomerises to form hexameric membrane channels[62] that is believed to release ATP and be larger enough to allow the passage of cationic and anionic molecules of up to 800–900 Da[65]. Brief activation of P2X7R also results in several morphological changes that resemble those seen following nsPEF treatment including membrane blebbing, phosphatidyl serine exposure, loss of mitochondrial membrane potential and cytoskeletal disruption[66].

The TRP family are made up of units of six transmembrane domains with intracellular C- and N- termini. The majority of TRP channels are found on the plasma membrane and in order to form a functional ion channel the assembly of four of these units is needed[67]. Three different TRPs have been shown to dilate sufficiently to allow the passage of YO-PRO-1: transient receptor potential vanilloid 1 (TRPV1)[68], transient receptor potential melastatin 8 (TRPM8)[69] and transient receptor potential ankyrin 1 (TRPA1)[70]. Their implication in the nsPEF response is considered due to their voltage dependent-gating which could be activated by the pulse. In addition these three TRPs have their activities modulated by interaction with phosphatidylinositol-4,5-bisphosphate (PIP_2) and through phosphorylation by protein kinase C and A[67,71], all of which are linked to the phospholipase C (PLC) pathway that is activated by nsPEF[72]. TRPV1 also uses its C-terminal to stabilizes microtubules with its activation leading to rapid microtubule depolymerisation[73], similar to the nsPEF effect that we report in the following chapter.

2.1.2. Nanoporation of organelles by nsPEF

The membranes of organelles can be charged by an external electric field in the same way as the plasma membrane is. Theoretical models suggest that this can also lead to their poration[48,51,74,75]. These models show that the duration of the electric field exposure needed to cause poration is much less for organelles than it is for the plasma membrane, with a 7 µm

cell typically needing a charging time of around 105 ns whereas a 1 µm organelle would only need around 15 ns[76]. This suggests that our 10 ns pulse should target intracellular membranes in addition to the plasma membrane. Experimentally, the poration of granule membranes in eosinophil cells was demonstrated to occur following the application of both 60 ns and 10 ns pulses[77,78]. As discussed in section 2.1.4 nsPEF induced mitochondrial membrane permeabilisation has also been reported[22].

2.1.3. Calcium

An increase in intracellular Ca^{2+} concentration ($[Ca^{2+}]_i$) following application of nsPEF has been widely shown. However, it is still unclear whether the source of this calcium is from intracellular stores, such as the endoplasmic reticulum (ER), or from extracellular calcium that enters through plasma membrane nanopores.

2.1.3.1. Calcium influx though nanopores in cellular membranes

N1-S1 cells, in a Ca^{2+} containing buffer, pulsed with a single 600 ns, 40 kV/cm pulse show an increase in $[Ca^{2+}]_i$ whereas the same treatment of cells in a buffer containing the Ca^{2+} chelator EGTA failed to show an increase in $[Ca^{2+}]_i$[24]. This suggests that extracellular calcium is the source of the increase. However, these cells were analysed by flow cytometry 10 minutes after pulse application. As calcium signals can be rapid and transient it is possible that this time frame was not well adapted to accurately capture calcium changes. Indeed, $[Ca^{2+}]_i$ measured in Fura-2 loaded HL-60 cells, over the time period of 5 – 300 seconds following a single 60 ns, 30 kV/cm pulse, showed a rapid and sustained increase of $[Ca^{2+}]_i$ in cells in a Ca^{2+} buffer and a rapid, but transient, increase in cells in an EGTA buffer[33]. Live cell imaging of Calcium Green loaded Jurkat cells showed a uniform increase in fluorescence across the cell, within seconds, following 10, 30 ns, 2.5 MV/m pulses[32]. This uniformity suggests an intracellular source of calcium. The same study backs up this argument by showing similar post-pulse $[Ca^{2+}]_i$ increases in cells in Ca^{2+} and in EGTA buffer. They show also that this increase could be reduced by prior depletion of calcium in the endoplasmoic reticulum (ER) using thapsigargin, which is an ER calcium pump inhibitor. It is however unclear, for these supporting results, at which time point the calcium increase was measured and whether, in agreement with White et al. (2004)[33], the increases observed were transient or sustained.

2.1.3.2. Activation of capacitative calcium entry or calcium induced calcium release

The difference between sustained and transient increases in $[Ca^{2+}]_i$ observed, respectively, in Ca^{2+} and EGTA buffers has been further examined[33]. Ca^{2+} was added to HL-60 cells, in an EGTA buffer, 1 minute-post pulse, when the $[Ca^{2+}]_i$ had returned to resting levels. $[Ca^{2+}]_i$ increased rapidly. These results mirrored those obtained for cells under the same conditions and treated with uridine-5'-triphosphate (UTP) instead of nsPEF. UTP is a purinergic agonist that causes the release of internal calcium stores via inositol-1,4,5-trisphosphate (IP_3) signalling. Low calcium in Ca^{2+} storing organelles triggers the opening of plasma membrane Ca^{2+} channels in a process called capacitative calcium entry (CCE). The authors conclude that nsPEF causes CCE to occur and that the sustained increase seen in Ca^{2+} containing buffer is due to Ca^{2+} entering through plasma membrane channels rather than through nanopores.

The CCE theory is however refuted by Semenov et al. (2013)[31]. They showed in Chinese hamster ovary (CHO) cells that, in a Ca^{2+} buffer, single 60 ns pulses at intensities over 9 kV/cm cause a rapid, low (200-350 nM) and sustained increase in $[Ca^{2+}]_i$. At intensities over 19 kV/cm the rise was again rapid reaching concentrations of 1–3 µM, before returning to resting levels within 2-3 minutes. When EGTA buffer was used an intensity of 19 kV/cm was needed to induce a rise in $[Ca^{2+}]_i$, again the rise was rapid and returned to resting levels within 50-100s. In addition they looked at the possibility of calcium induced calcium release (CICR) playing a role in the increase in $[Ca^{2+}]_i$. CICR is the cells natural way of propagating calcium signals and thus increasing cellular response time. Calcium and IP_3, that is produced during nsPEF stimulation[72], bind to IP_3 receptors (IP_3R) and ryanodine receptors, which are Ca^{2+} release channels on the ER membrane. Opening these channels increases the local Ca^{2+} concentration and thus results in the activation and opening of adjacent receptors and potentially the opening of Ca^{2+} releasing mitochondrial permeability transition pores [79]. CHO cells do not have ryanodine receptors and on blocking the IP_3R following a 60 ns, 30 kV/cm pulse $[Ca^{2+}]_i$ was found to only rise to between 400-500 nM. The authors interpreted these results as the cell's plasma membrane being more susceptible to nanoporation by nsPEF than the ER membrane (thresholds for poration at 9 kV/cm and 19 kV/cm respectively for the 60 ns pulse), with the nanoporation being a short lived event. During nanoporation the $[Ca^{2+}]_i$ remains within physiological levels. The $[Ca^{2+}]_i$ increases seen with the lower intensity pulses fail to provoke a cellular response, including clearance of Ca^{2+}, resulting in the sustained signal. When $[Ca^{2+}]_i$ reach a critical level (~300 nM) CICR is induced leading to the µM

range concentrations seen with the higher intensity pulses. CICR is self-limiting ending when the channels close and/or the ER Ca^{2+} stock is depleted. Ca^{2+} is then returned to the ER by sarcoplasmic/endoplasmic reticulum Ca2+-ATPase (SERCA) [80]. This could explain return to resting levels of $[Ca^{2+}]_i$ seen with the higher intensity pulses.

2.1.4. nsPEF causes loss of mitochondrial membrane potential ($\Delta\Psi_m$)

Given that poration of both the plasma and ER membranes are thought to be a result of nsPEF treatment, the poration of the mitochondrial membrane has also been proposed. This was demonstrated when mitochondrial membranes of Jurkat cells were shown to be more susceptible to permeabilisation than the plasma membranes following 5, 4 ns, 10 MV/m pulses[23]. This permeabilisation is linked to a decrease in $\Delta\Psi_m$. $\Delta\Psi_m$, as measured by tetramethylrhodamine, ethyl ester (TMRE) a dye that sequesters in active mitochondria, was found to decrease in E4 squamous carcinoma cells by 10 minutes post-pulse (10, 300 ns pulses, between 0 and 60 kV/cm)[81]. Earlier time points however were not reported so it is difficult to determine from this result whether the loss of $\Delta\Psi_m$ is due to a direct effect of nsPEF or is the downstream result of other changes in the cell. Another study, using Jurkat cells, looked at a shorter time scale and showed that when delivering 4 ns, 10 MV/m pulses, at a 1 kHz repetition rate, higher pulse numbers ($\geq$30) caused a decrease in $\Delta\Psi_m$ within 30 seconds of pulse application (~10% decrease as compared to pre-pulse levels, for 30 pulses) which had decreased further by 3 minutes (~50% decrease as compared to pre-pulse levels, for 30 pulses). At lower pulse numbers (10) there was no change in $\Delta\Psi_m$ after 30 seconds and a 20% decrease after 3 minutes[22]. This study linked the loss in $\Delta\Psi_m$ to mitochondrial membrane permeabilisation using cobalt-quenched calcein stained cells, but again the authors could not confirm if the permeabilisation was a direct effect of nsPEF or a secondary effect of another process. Beebe et al. (2012)[24], however, call into question the theory of nsPEF nanoporation of mitochondrial membrane. They show in N1-S1 cells that loss of $\Delta\Psi_m$, following a single 600 ns, 80 kV/cm pulse, is both time and calcium dependant, whereas nanoporation would cause an immediate and calcium independent loss of $\Delta\Psi_m$.

Low energy status in nsPEF treated cells, as measured by ATP levels and AMP-activated protein kinase activity, has been reported and linked to the loss of mitochondrial activity [82,83]. nsPEF with short rise and fall times have a more detrimental effect on $\Delta\Psi_m$, linked to decrease in cell viability, than those with long rise and fall times[24]. As changes to $[Ca^{2+}]_i$ were similar with both short and long rise and fall times the authors concluded that intracellular

membranes are more sensitive to short rise and fall times than plasma membranes. They concluded also that loss of $\Delta\Psi_m$ plays an intrinsic part in nsPEF related cell death.

2.1.5. Objectives

From the published material it is evident that the impact that nsPEF will have on a cell is dependent on the type of exposure system, the field strength applied, the pulse's duration, the repetition rate and cell types used. The objective of this chapter is therefore to assess the sensitivity of our cell of interest, U87 glioblastoma, to our nanopulse generating system and application method. We also aim to determine a pulse application regime that will have an effect on our cells and compare these effects to previously published data.

2.2. Material and methods

2.2.1. Cell line and culture

The human glioblastoma cell line U87-MG (ATCC HTB-14) was cultured in T75 flasks at 37°C, 5% CO_2 in MEM medium (Gibco, 10370-047) supplemented with 10% FBS (Gibco, 10500), 2 mM L-glutamine (Dutscher, X0550-100), 1.1 mM glucose (Gibco, 19002-013), 100 U/ml penicillin and 100 µg/ml streptomycin (Gibco, 15070-063). On reaching 80% confluence, cells were detached from the surface of the flask by washing twice with PBS (Gibco, 14190) and then incubating for 3-5 minutes at 37°C with trypsin (Gibco, 25200-056). Trypsin activity was stopped with the addition of an equal quantity of defined trypsin inhibitor (Gibco, R-007-100) and then centrifuged for 10 minutes at 600g. The resulting cell pellet was resuspended in MEM for use in experiments and for reseeding flasks.

2.2.2. Preparation of poly-L-lysine coated coverslips

For microscope analysis cells were adhered to 22 mm round, glass coverslips (Dutscher, 140541DD) that were coated in poly-L-lysine (P9155, Sigma). For coating, coverslips were first washed in 100% ethanol and then rinsed in sterile PBS before being placed, individually, in 35 mm plastic petri dishes. 2 ml of PBS containing 5µg/ml of poly-L-lysine was added to each petri dish and incubated at 37°C for at least 2 hours. After incubation the liquid was aspirated from each petri dish and replaced with 2 ml of a cellular suspension containing 1.8 x 10^5 cells/ml. Cells were then cultured for 24 - 48 hours before use in imaging.

2.2.3. Live cell imaging

Cells were observed by epifluorescence using a Leica DMI6000 microscope with a 100x objective. Fluorescent excitation was provided by a Spectra 7 light engine (Lumencor). Emitted light was filtered and captured on an electron-multiplying charge-coupled device camera (EMCCD; Photometrics Evolve 512, Roper) with 512 x 512 pixels. The system was controlled by, and images were captured with, Metafluor (version 7.8, Molecular Devices). Protocols for each experiment were first optimised to minimize illumination in order to reduce photobleaching.

2.2.3.1. Measurement of plasma membrane permeability

For measurement of cell membrane poration coverslips were removed from their dishes, sandwiched into plastic imaging chambers and covered in 1 ml of 1 µM of YO-PRO-1 (Life Technologies, Y3603) in room temperature HBSS (NaCl 121 mM, KCl 5.4 mM, $MgCl_2$ 0.8 mM, $NaHCO_3$ 6 mM, D-glucose 5.5 mM, HEPES 25 mM, $CaCl_2$ 1.8 mM, pH 7.3). The coverslips were imaged immediately using an excitation of 475/25 nm and emission at 525/50 nm with an exposure time of 35 ms and 10% source intensity. For P2X7R experiments cells were incubated for 30 minutes at 37°C with either 10 µM A-438079 (Sigma, A9736) or 1 mM probenecid (Sigma, P8761) in HBSS. For TRP experiments cells were incubated for 10 minutes at 37°C with 1 µM A-784168 (Tocris, 4319), 10 µM M8B (Sigma, SML0893) or 30 µM AP18 (Sigma, A7232) in HBSS.

2.2.3.2. Measurement of changes in intracellular calcium

For measurement of intracellular calcium levels cells were incubated for 30 minutes at room temperature, in the dark, in HBSS or Ca^{2+} free HBSS (NaCl 121 mM, KCl 5.4 mM, $MgCl_2$ 0.8 mM, $NaHCO_3$ 6 mM, D-glucose 5.5 mM, HEPES 25 mM, EGTA 4 mM, pH 7.3) containing 1.25 µM Fura Red, AM (Life Technologies, F3020) or 0.5 µM FLUO-4, AM (Life Technologies, F14201), 0.02% pluronic acid (Life Technologies, P3000MP), then washed three times in the corresponding HBSS and incubated a further 30 minutes at room temperature in the dark. To deplete intracellular calcium stores cells were incubated with 1 µM of thapsigargin (Sigma, T9033) in Ca^{2+} free HBSS for the final 30 minute incubation before imaging. Cells loaded with Fura Red were imaged with an excitation of 475/25 nm and emission at 615/25 nm with an exposure time of 25 ms and 5% source intensity. For

FLUO-4 excitation was 475/25 nm and emission 525/50 nm with an exposure time of 10 ms and 5% source intensity.

2.2.3.3. Measurement of mitochondrial membrane potential

Mitochondrial membrane potential was measured by incubating cells with 10 nM Tetramethylrhodamine, methyl ester (TMRM) (Interchim, FP-21089A) at room temperature, in the dark for 30 minutes, and washing three times in HBSS before imaging. For the sodium free experiments cells were loaded with TMRM in normal HBSS and washed with and imaged in a HBSS variant made of: KCl 5.4 mM, $MgCl_2$ 0.8 mM, $CaCl_2$ 1.8 mM, $CHKO_3$ 6 mM, Glucose 5.5 mM, HEPES 25 mM, 146 mM choline chloride, pH 7.3. Cells were imaged with an excitation of 542/27 nm and emission at 615/25 nm with an exposure time of 10 ms and 5% source intensity.

2.2.4. Exposure of cells to nsPEF

10 ns pulses, with an electric field strength of 44 kV/cm (unless otherwise stated), were applied to cells using an nsPEF generator (FPG 10-1NM-T, FID Technology, Germany) with 50 Ω output impedance. A high-voltage measurement device (tap-off 245 NMFFP-100, Barth Electronics Technology, USA) connected to an oscilloscope (DPO 4104, Tektronix, USA) was used to visualize the time-domain measurements of the pulse[84–86]. Pulses were applied by positioning an electrode delivery system with a micromanipulator (Sutter MP285) comprising of two steel electrodes, separated by a gap of 1.2 mm and with 50 Ω impedance in parallel[37].

2.2.5. Image analysis

Images were analysed using Image Analyst MKII (Image Analyst Software). Background was subtracted from the stack of images by manually drawing a region of interest (ROI) in a zone that did not contain cells and subtracting the grey level in this area from the rest of the image. ROIs were then drawn to include the entire cell of interest and fluorescence intensity data for the ROIs were generated by Image Analyst MKII.

2.2.6. Statistical analysis

Statistical analyses were performed with OriginPro 2016 software. Datasets were first tested for normal distribution using Q-Q plots and a Levene's test was used to assess the homogeneity of variance. Changes in fluorescence intensity were statistically tested over time (repeated measures) and between independent treatments (between groups) using a mixed-

model two-way repeated measures analysis of variance (ANOVA). The source of significant differences identified by ANOVAs was found using pair-wise post-tests that were Bonferroni corrected. Effects were considered statistically significant when the probability of falsely rejecting the null hypothesis was less than 0.05 ($p<0.05$).

2.3. Results

2.3.1. Effect of nsPEF on plasma membrane permeability

2.3.1.1. nsPEF causes YO-PRO-1 uptake in a dose dependent manner

The first reported nsPEF effect that we tested was membrane poration. To do this we used the fluorescent dye YO-PRO-1, a cell impermeable dye that is only able to enter the cell when the plasma membrane is compromised. By looking at YO-PRO-1 uptake at different pulse application regimes (1 pulse, 10 pulses at 1 Hz, 10 Hz or 100 Hz and 100 pulses at 1 Hz, 10 Hz or 100 Hz) we were able to determine that poration occurs and that it is dependent on both pulse number and frequency of application (Figure 11a). The effect of frequency is most clearly demonstrated by the results for 100 pulses, where YO-PRO-1, for the 1 Hz application, follows a slower sigmoidal uptake compared to the rapid uptake for 10 and 100 Hz. By considering the area under the curve for the entire imaging period (Figure 11b) we see a total YO-PRO-1 uptake with a dose-response effect for increasing pulse numbers and for increasing frequencies within the same number of pulses. This effect appears to reach a plateau between 100 pulses delivered at 10 Hz and 100 pulses delivered at 100 Hz. YO-PRO-1 entry into the cell was not uniform and instead had a polar entry before diffusing across the cell (Figure 11c).

A.

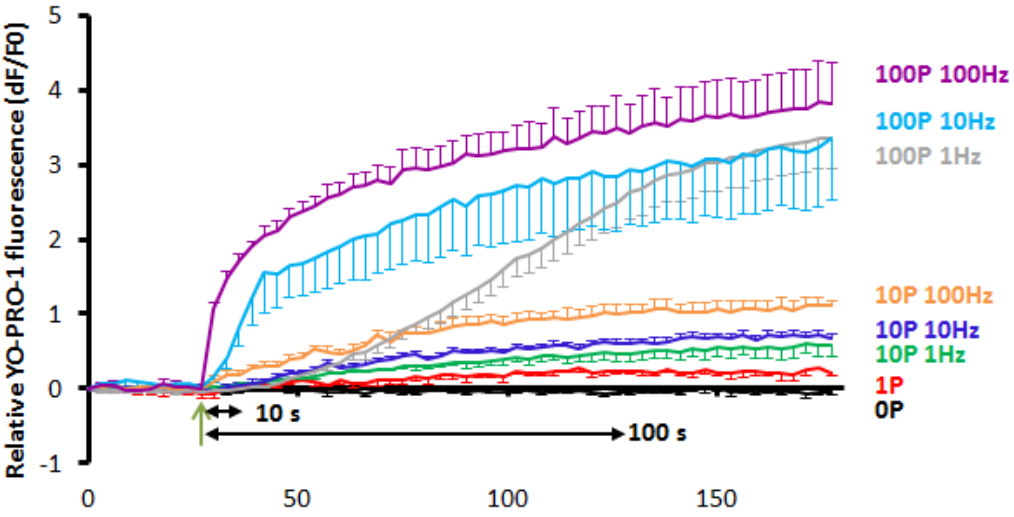
Relative YO-PRO-1 fluorescence (dF/F0)
5
4
3
2
1
0
-1
0
50
100
150
10 s
100 s
100P 100Hz
100P 10Hz
100P 1Hz
10P 100Hz
10P 10Hz
10P 1Hz
1P
0P

B.

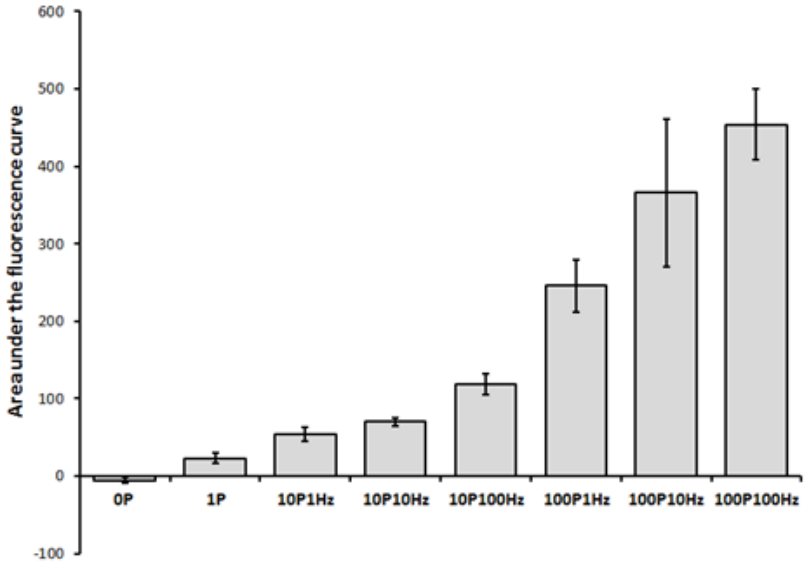
Area under the fluorescence curve
600
500
400
300
200
100
0
-100
0P
1P
10P1Hz
10P10Hz
10P100Hz
100P1Hz
100P10Hz
100P100Hz

C.

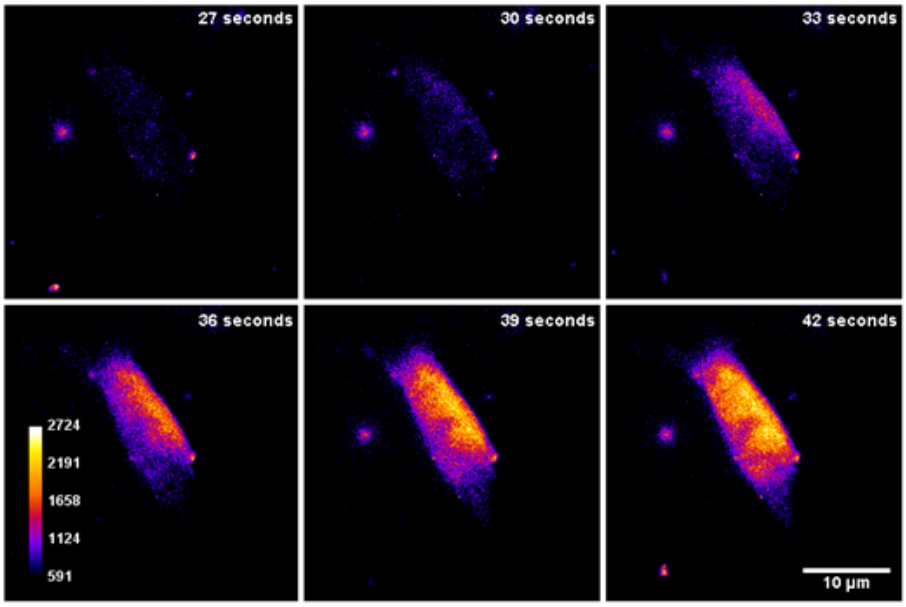
27 seconds
30 seconds
33 seconds
36 seconds
39 seconds
42 seconds
2724
2191
1658
1124
591
10 µm

Figure 11. Temporal and spatial uptake of YO-PRO-1 as a function of pulse number and frequency.

a: Change in fluorescence over time from live cell imaging experiments on YO-PRO-1 uptake into U87 cells following application of 10 ns pulses at varying pulse numbers and repetition rate frequencies. The start of pulse application is represented by a green arrow. The 10 s line shows the pulse duration for 100 pulses 10 Hz and 10 pulses 1 Hz. The 100 s line shows the pulse duration for 100 pulses 1 Hz. Error bars show S.E. 0P n = 5, 1P n = 4, 10P 1 Hz n = 4, 10P 10 Hz n = 7, 10P 100 Hz n = 4, 100P 1 Hz n = 7, 100P 10 Hz n = 4, 100P 100 Hz n = 4. b. Total area under the fluorescence curves for each pulse regime based on the results in part a. Error bars show S.E. c: Representative live cell images of YO-PRO-1 cellular uptake following 100, 10 ns pulses at 10 Hz. The pulse train was applied just after the image capture at 27 seconds (first image in sequence). The images are pseudocoloured for contrast and the colour calibration bar represents arbitrary units of fluorescence.

2.3.1.2. Determination of how YO-PRO-1 enters the cell

There are four membrane receptors that are known to form pores/channels which can gate YO-PRO-1: P2X7R, TRPV1, TRPA1 and TRPM8. Whilst nanoporation is a widely accepted result of nsPEF treatment it is also possible that one or more of these pores may be implicated to some extent in the observed permeability. To determine their involvement we used different pharmacological inhibitors of the receptors to see if they decreased YO-PRO-1 uptake.

2.3.1.2.1. P2X7R

The P2X7R was inhibited by incubation (30 minutes at 37°C in HBSS) with 1 mM of Probenecid or 10 µM of A-438079. Applying one pulse to untreated cells caused a 0.2 fold increase in YO-PRO-1 fluorescence which started gradually after the pulse application (Figure 12). A similar increase in fluorescence occurred in the cells that had been treated with A-438079. The cells treated with probenecid, however, failed to show an increase in fluorescence after pulse application, reflecting the results of cells that had not been pulsed.

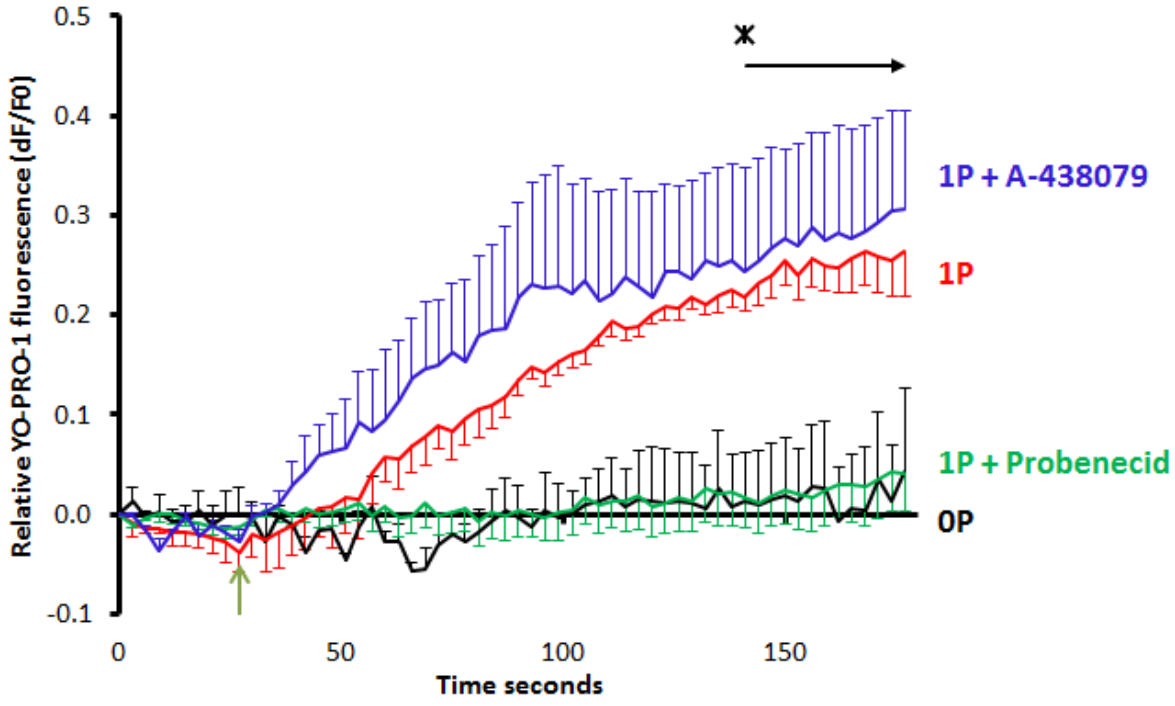

Figure 12. The effect of P2X7 antagonist/inhibitors on YO-PRO-1 uptake following application of 1, 10 ns pulse.

1 pulse was applied to cells incubated with 10 µM A-438079 (blue line, n=4) or 1 mM probenecid (green line, n=4) or no inhibitor (red line, n=4). The black line denotes the non-pulsed control (n=3). Error bars show S.E. and the light green arrow indicates pulse application. Asterisk indicates a significant difference between the 0 pulse response and that of 1 pulse and 1 pulse with A-438079 as well as a significant difference between 1 pulse and 1 pulse with probenecid, as reported by two-way repeated measures ANOVA with Bonferroni tests, $F(4.61, 15.35) = 5.82$, $p < 0.05$.

To see if the inhibitory effect of probenecid held true at higher pulse numbers we next looked at YO-PRO-1 uptake following the application of 100 pulses at 10 Hz. We found the same increase in fluorescence in cells treated with or without probenecid (Figure 13).

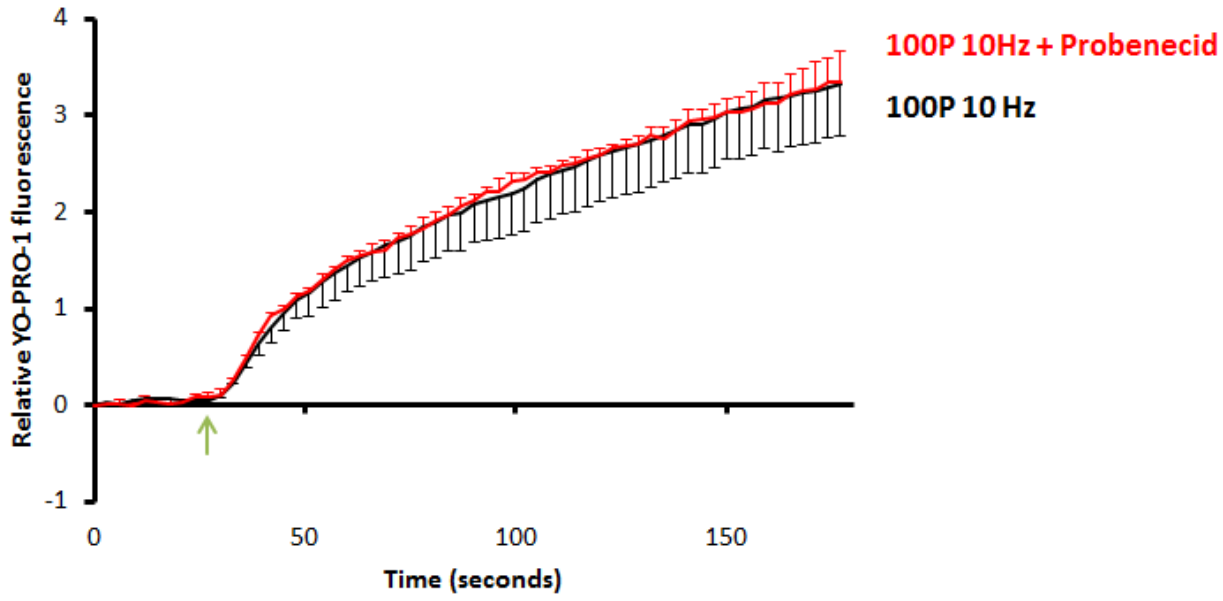

Figure 13. The effect of P2X7 blocker probenecid on YO-PRO-1 uptake following application of 100, 10 ns pulse at 10 Hz.

100, 10 ns pulses were applied at 10 Hz to cells incubated with 10 1 mM probenecid (red line, n=3) or no inhibitor (back line, n=3). Error bars show S.E. and the light green arrow indicates pulse application. There was no significant difference between the two conditions as reported by two-way repeated measures ANOVA with Bonferroni tests, $F(1.27, 5.09) = 0.02$, $p > 0.05$.

2.3.1.3. TRP channels

The TRP channels were inhibited by incubating cells (10 minutes at 37°C in HBSS) with one of the following inhibitors: 1 µM of A-784168 (TRPV1), 10 µM of M8B (TRPM8) or 30 µM AP18 (TRPA1 inhibitor). When 100 pulses were applied at 1 Hz there was found to be no difference in YO-PRO-1 uptake under any of the pharmacological treatments when compared to the untreated cells (Figure 14).

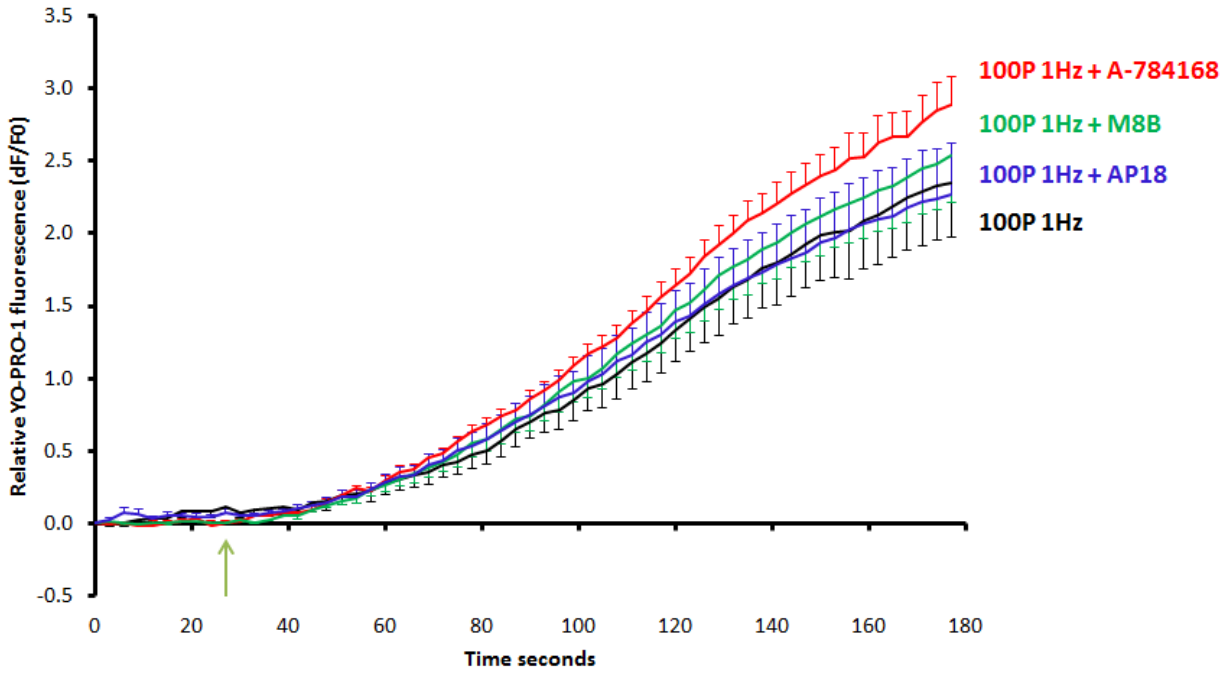

Figure 14. The effect of different TRP channel inhibitors on YO-PRO-1 uptake following application of 100, 10 ns pulses applied at 1 Hz.

Pulses were applied to cells incubated with 1 µM A-784168 (TRPV1 inhibitor, red line, n = 4 over 3 independent experiments), 10 µM M8B (TRPM8 inhibitor, green line, n = 9 over 5 independent experiments), 30 µM AP18 (TRPA1 inhibitor, blue line, n = 8 over 6 independent experiments) or no inhibitor (black line, n = 7 over 4 independent experiments). Error bars show SE and the light green arrow indicates start of pulse application. There is no significant difference between any of the tested conditions, as measured by two-way repeated measures ANOVA with Bonferroni tests, $F(3.07, 24.60) = 0.49$, $p > 0.05$.

2.3.2. Effect of nsPEF of intracellular calcium levels

2.3.2.1. Effect of 1 pulse on intracellular calcium levels using FLUO-4

Preliminary experiments to investigate the effect of nsPEF on intracellular calcium levels within the cell were carried out using the calcium indicator FLUO-4, AM. This indicator shows an increase in fluorescence on binding calcium. U87 cells loaded with the dye were exposed to a single 10 ns pulse after recording a 5 minute base line with image captures every 30 seconds (Figure 15). Of the five separate pulsed experiments only one cell responded with an increase in intracellular calcium. Whilst the control shows that the imaging conditions caused some loss of fluorescence, either due to photobleaching or clearance from the cell

through anion transporters[87], they had been sufficiently optimised to avoid light induced calcium responses[88].

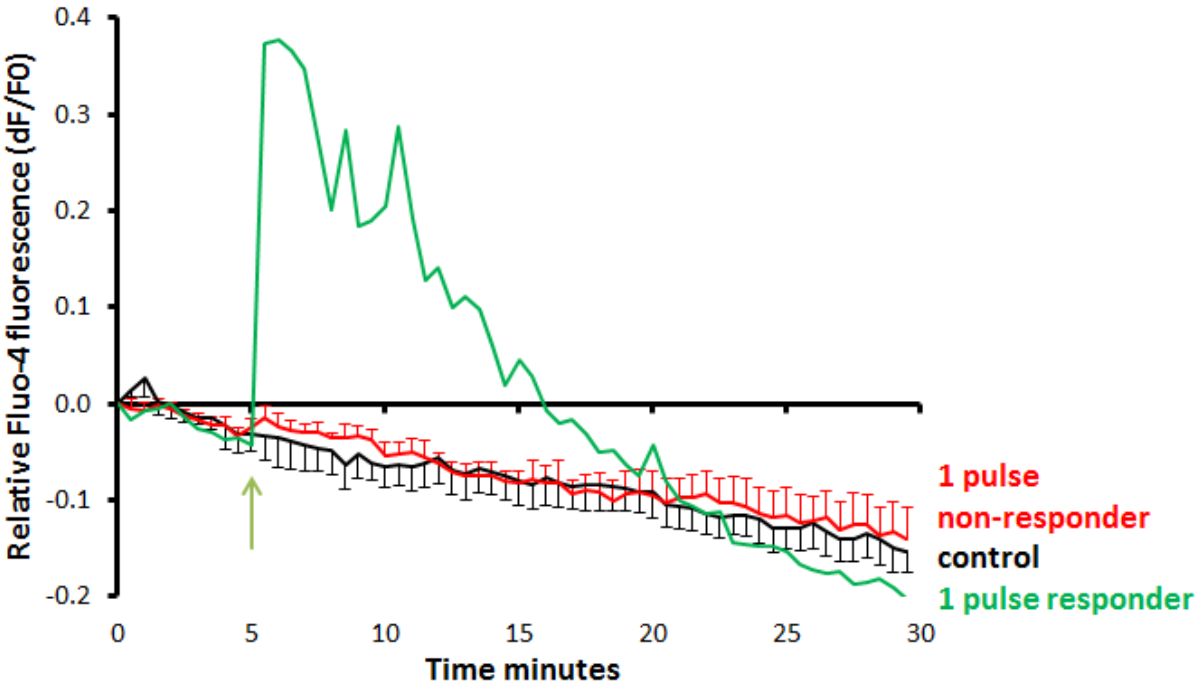

Figure 15. The effect of 1, 10 ns pulse on intracellular calcium in U87 cells.

The black line denotes averages for control experiments (n = 4), where no pulses were applied. The red line denotes averages for pulsed, non -responding experiments (n = 4) and the green line for the responder (n=1). Pulse application is denoted by the green arrow. Error bars show S.E.

2.3.2.2. The effect of 100, 10 ns pulses applied at 10 Hz on intracellular calcium levels using FLUO-4

There were two obvious reasons that would explain the lack of a consistent post-pulse change in intracellular calcium. The first is that the response was too rapid to be caught by the relatively slow imaging protocol. The second is that one pulse was not sufficient to elicit a reproducible effect. We therefore optimised a faster imaging protocol, taking one image every second, and applied a higher number of pulses (100 pulses at 10 Hz). This resulted in a rapid, repeatable, almost 6-fold, increase in intracellular calcium following the pulse and elimination of photobleaching (Figure 16). The calcium response continued to increase throughout the pulse application period before plateauing at the end of this period and beginning to slowly decrease.

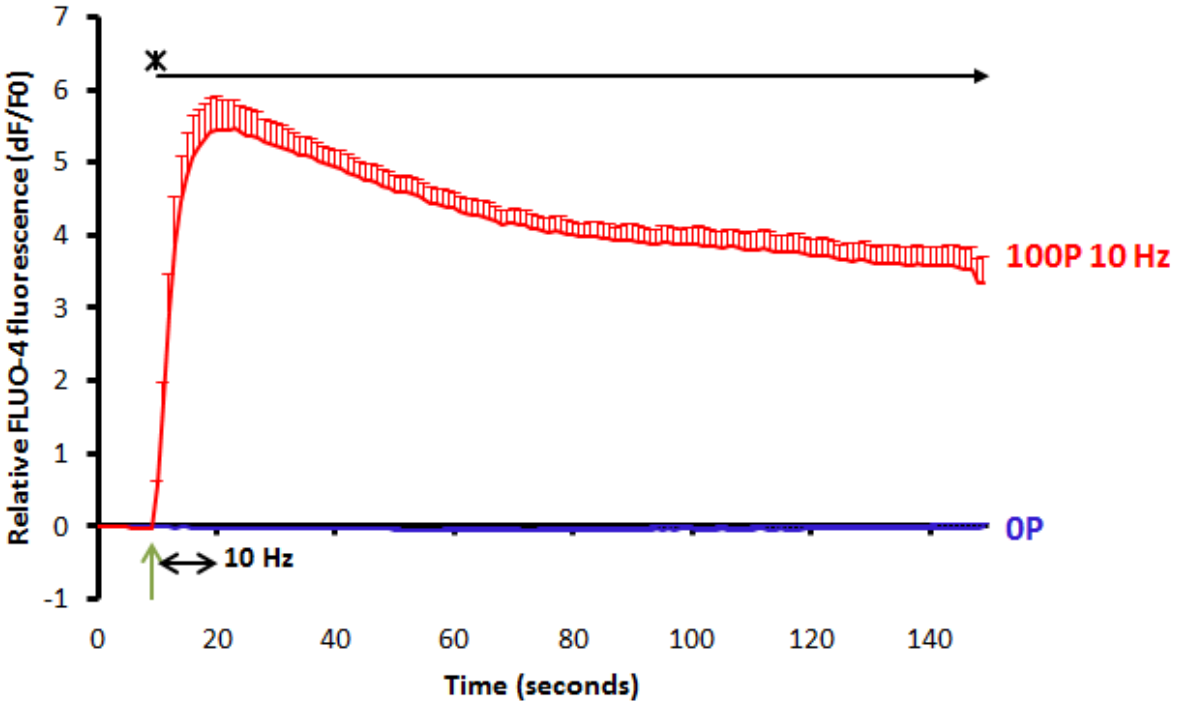

Figure 16. The effect of 100, 10 ns pulse applied at 10 Hz on intracellular calcium in U87 cells.

The blue line denotes averages for control experiments (n = 3), where no pulses were applied. The red line denotes averages for 100 pulses applied at 10 Hz (n = 3). The start of pulse application is denoted by the green arrow and the duration is shown by the black double ended arrow. The asterisk indicates a significant difference between the 100 pulse at 10 Hz response and 0 pulse control as reported by two-way repeated measures ANOVA with Bonferroni tests, $F(1.57, 6.26) = 124.94$, $p < 0.05$. Error bars show S.E.

2.3.2.3. Effect of 100P applied at 10 Hz on intracellular calcium levels using Fura Red, AM

In an attempt to carry out a more quantitative assessment of the intracellular calcium concentrations we used the ratiometric dye Fura Red, AM. This indicator has a dual excitation and ratiometric confocal imaging has previously been demonstrated using 457 nm to excite the non-calcium bound form of the dye and 488 nm to excite the calcium-bound form[89] with emissions for both collected on a 585 nm longpass filter. When intracellular calcium concentrations increase both fluorescent levels decrease, however the ratio of F_{457}/F_{488} increases. This method also allows for the correction of photobleaching and other imaging artefacts. However, due to equipment limitation and budgetary constraints, we were unable to exploit the dual excitation with the LED illumination system and the filter sets available to us.

We were, however, able to excite and image the calcium bound form and induce a reproducible increase in intracellular calcium by using 100 pulses applied at 10 Hz (Figure 17). A 0.5 fold decrease in Fura Red fluorescence, representing an increase in intracellular Ca^{2+} concentration, was observed in the first 3 seconds following the start of pulse application. A minimum, and stable, level of fluorescence was reached by 9 seconds with the timing of this stabilisation corresponding with the end of the pulse application period. The control experiments also showed a degree of photobleaching which is likely to mask any recovery of calcium levels in the pulsed experiments.

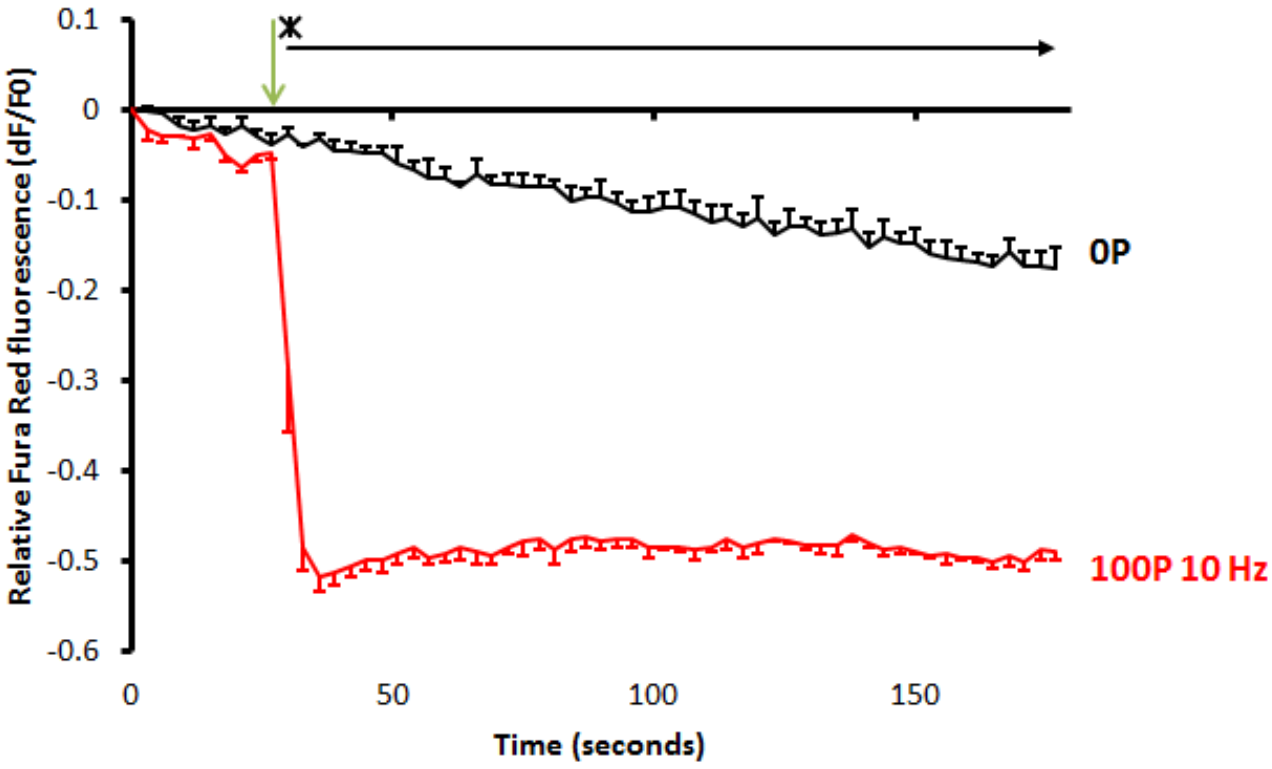

Figure 17. Change in Fura Red fluorescence in U87 cells subjected to 100 pulses delivered at 10 Hz.

Pulsed experiments are represented by the red line (n = 3) and non-pulsed controls by the black line (n = 3). A decrease in Fura Red fluorescence denotes an increase in calcium concentration. The asterisk indicates a significant difference between the pulsed and control experiments as reported by two-way repeated measures ANOVA with Bonferroni tests, $F(1.96, 7.83) = 172.06$, $p < 0.05$. Error bars show S.E and the green arrow the start of pulse application.

2.3.2.4. Identifying the source of the calcium increase

The increased calcium in the cell, following nsPEF treatment, has previously been attributed to both extracellular and intracellular sources. Having confirmed permeabilisation of the plasma membrane an influx of extracellular calcium seemed likely but intracellular calcium stores, such as the E.R. could also add to the effect. To determine the contribution of each source we pulsed Fura Red loaded cells in a calcium-free HBSS containing the calcium chelator EGTA which would give an indication of extracellular influx. We also pulsed cells which had had their intracellular stores depleted with thapsigargin in the same calcium free HBSS. Thapsigargin is an inhibitor of the sarco/endoplasmic reticulum Ca^{2+} ATPase (SERCA) which transfers calcium from the cytosol into the ER. The difference in response between the two conditions would give us an indication of the contribution of the intracellular stores. We found that both conditions gave a similar response when 100 pulses were applied at 10 Hz with the elimination of the decrease in Fura Red fluorescence observed previously in the presence of calcium (Figure 18).

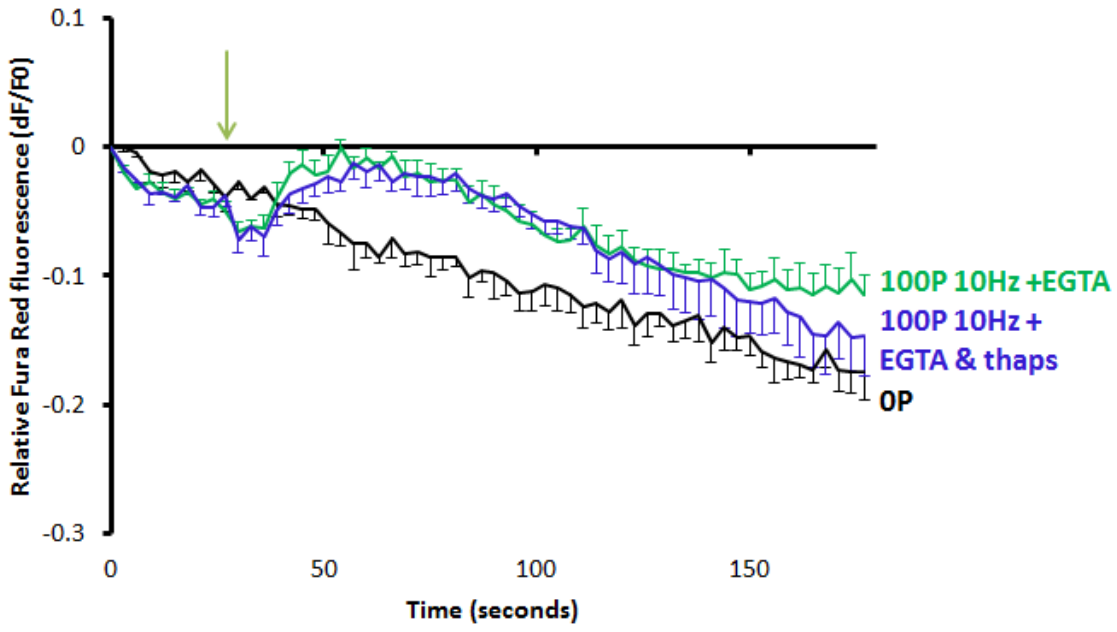

Figure 18. Change in Fura Red fluorescence in calcium depleted U87 cells subjected to 100 pulses delivered at 10 Hz.

In calcium free HBSS (green line, n = 3) or in calcium free HBSS with thapsigargin depleted intracellular stores (blue line, n = 3). The non-pulsed control is shown by the black line (n = 3). A decrease in Fura Red fluorescence denotes an increase in calcium concentration. The green arrow denotes the start of pulse application and error bars show S.E.

We observed also a slight increase in fluorescence 6-9 seconds after the start of pulse application which appeared to be a result of cell contraction rather than due to a decrease in calcium concentration. To confirm that the increase is just an artefact, the experiment was repeated using FLUO-4 (Figure 19). No significant differences were found in the fluorescence responses between either of the calcium free pulsed conditions or the control. There was also no post pulse change in fluorescence supporting the idea of minor cell contraction.

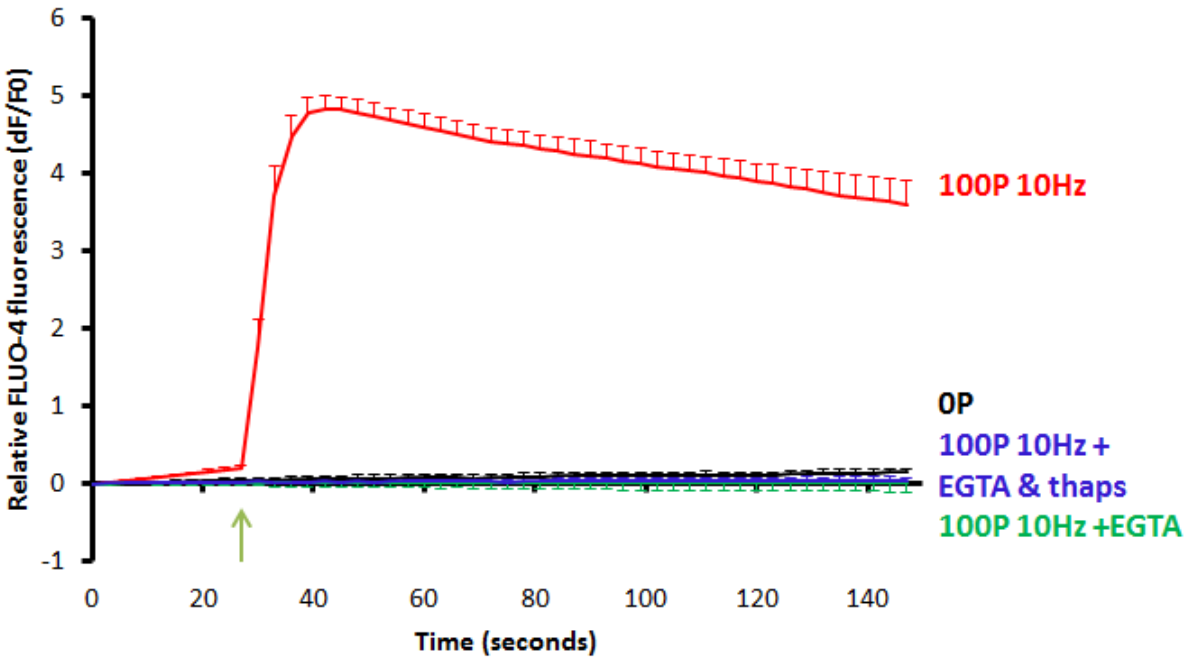

Figure 19. Change in FLUO-4 fluorescence in U87 cells subjected to 100 pulses delivered at 10 Hz.

In normal HBSS (red line, n = 8) a calcium free HBSS (green line, n = 3) or in calcium free HBSS with thapsigargin depleted intracellular stores (blue line, n = 3). The non-pulsed control is shown by the black line (n = 4). There were no significant differences between the non-pulsed condition and either of the pulsed calcium free conditions, as measured by two-way repeated measures ANOVA with Bonferroni tests, $F(2.75, 9.63) = 0.87$, $p > 0.05$. The green arrow denotes the start of pulse application and error bars show S.E.

2.3.3. Effect of nsPEF on the cell mitochondrial membrane potential

We next sought to confirm that our nsPEF system could cause a loss of $\Delta\Psi_m$. U87 cells were loaded with TMRM and subjected to 100 pulses applied at 10 Hz with an electric field strength of 44 kV/cm. This resulted in the immediate onset of a gradual reduction in TMRM

fluorescence, indicating a gradual loss of $\Delta\Psi_m$ (Figure 20). Lowering the electric field strength demonstrated that this effect had a dose-response relationship. At lower field strengths the depolarisation was reduced and occurred more slowly, with no depolarisation occurring for pulses of 16.5 kV/cm (Figure 21).

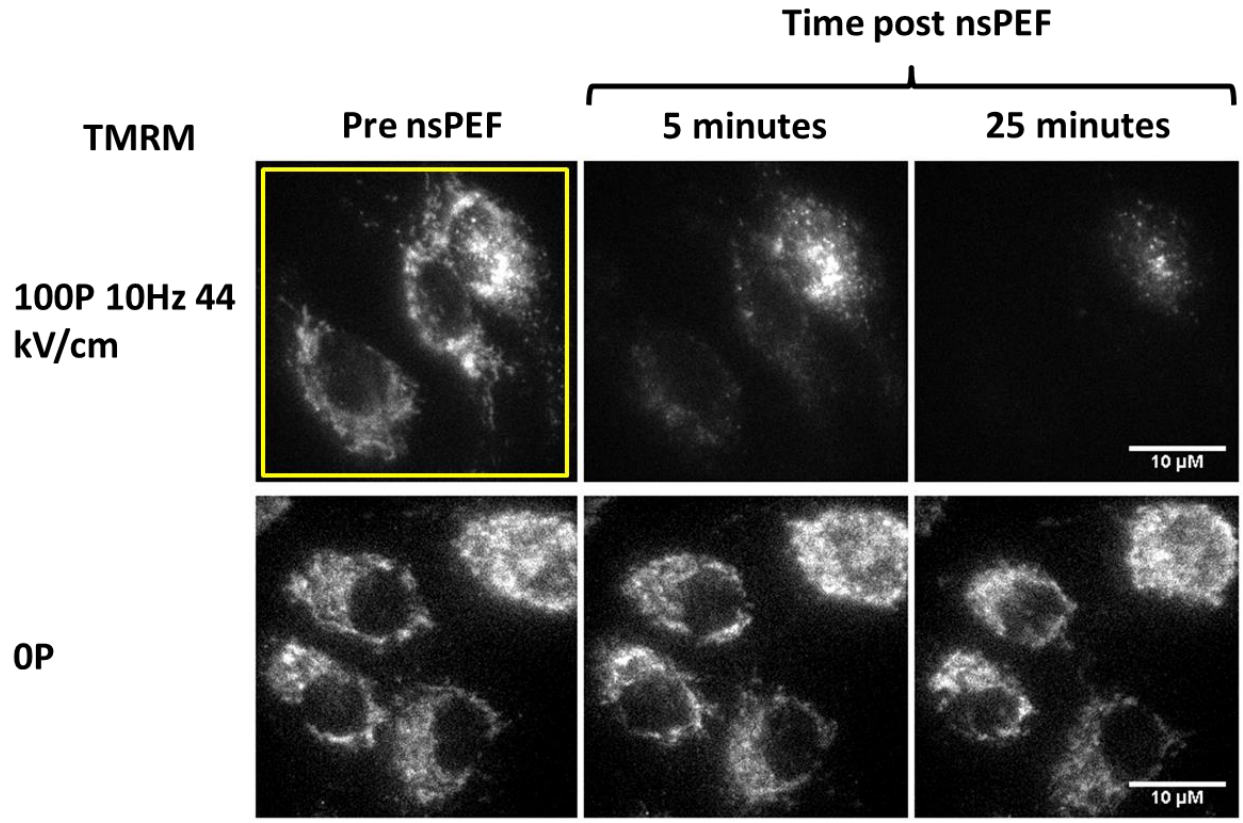

Figure 20. Effect of nsPEF on mitochondrial membrane potential.

Representative live cell images showing the effect of 100, 10 ns, 44 kV/cm pulses on $\Delta\Psi_m$ as measured by TMRM fluorescence, compared to a non-nsPEF treated control. TMRM fluorescence decreases with loss of $\Delta\Psi_m$. The yellow square shows the ROI used to measure TMRM fluorescence.

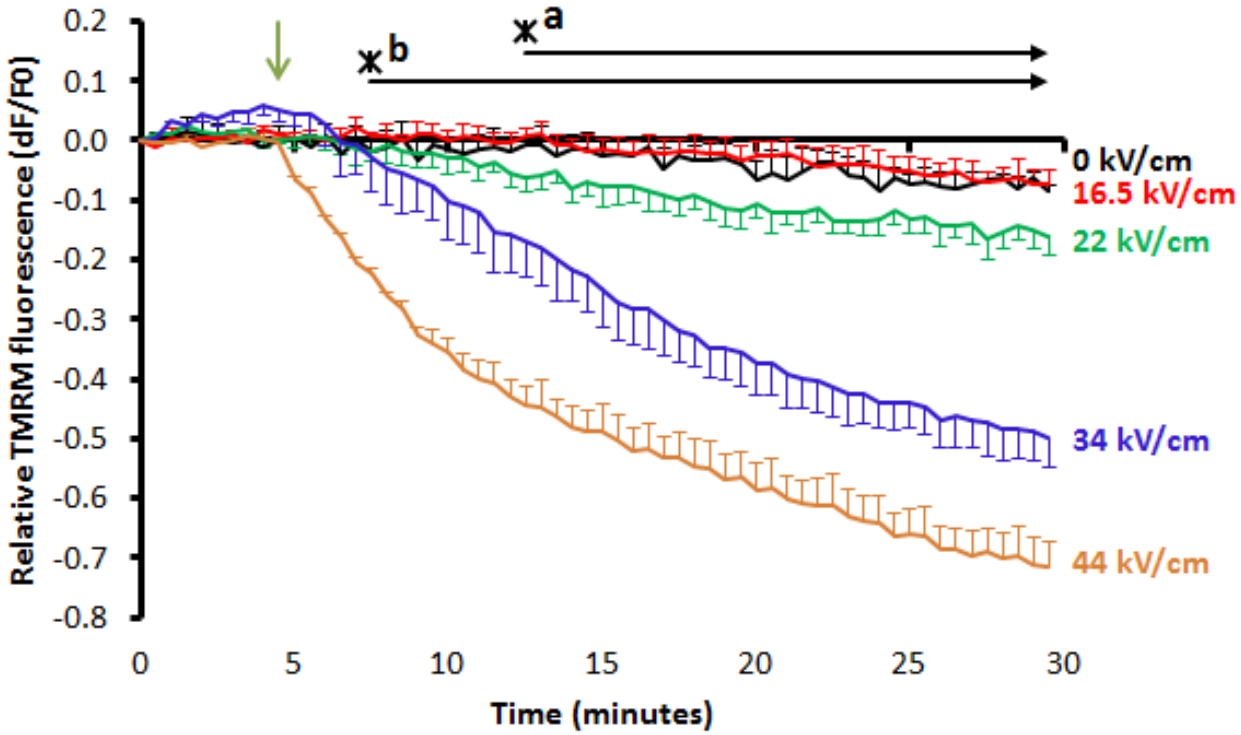

Figure 21. Effect of different electric field strengths on mitochondrial membrane potential.

100, 10 ns pulses delivered at a frequency of 10 Hz applied to U87 cells loaded with TMRM with electric field strengths of 0 kV/cm (black line, n = 3), 16.5 kV/cm (red line, n = 3), 22 kV/cm (green line, n = 3), 34 kV/cm (blue line, n=3) and 44 kV/cm (orange line, n = 4). There was a significant difference between 44 and 0 kV/cm and between 34 and 0 kV/cm as well as between 34 and 44 kV/cm, two way repeated measures ANOVA with Bonferroni test, $F(8.41, 23.12) = 46.82$, $p < 0.05$. The green arrow denotes the start of pulse application and the error bars show S.E.

One potential cause of this depolarisation is the increased levels of Ca^{2+} within the cell. When intracellular Ca^{2+} levels rise, mitochondria take up Ca^{2+} via their calcium uniporter. If Ca^{2+} concentrations within the mitochondrial matrix become too elevated the mitochondrial permeability pore (mPTP) opens to release the excess. This mPTP opening results in loss of $\Delta\Psi_m$[90]. To see if calcium influx was the cause of our depolarisation we measured $\Delta\Psi_m$ in cells pulsed in a Ca^{2+} free HBSS in order to prevent the post-pulse increase in intracellular Ca^{2+}. We found that this did not have an impact on the loss of $\Delta\Psi_m$ (Figure 22).

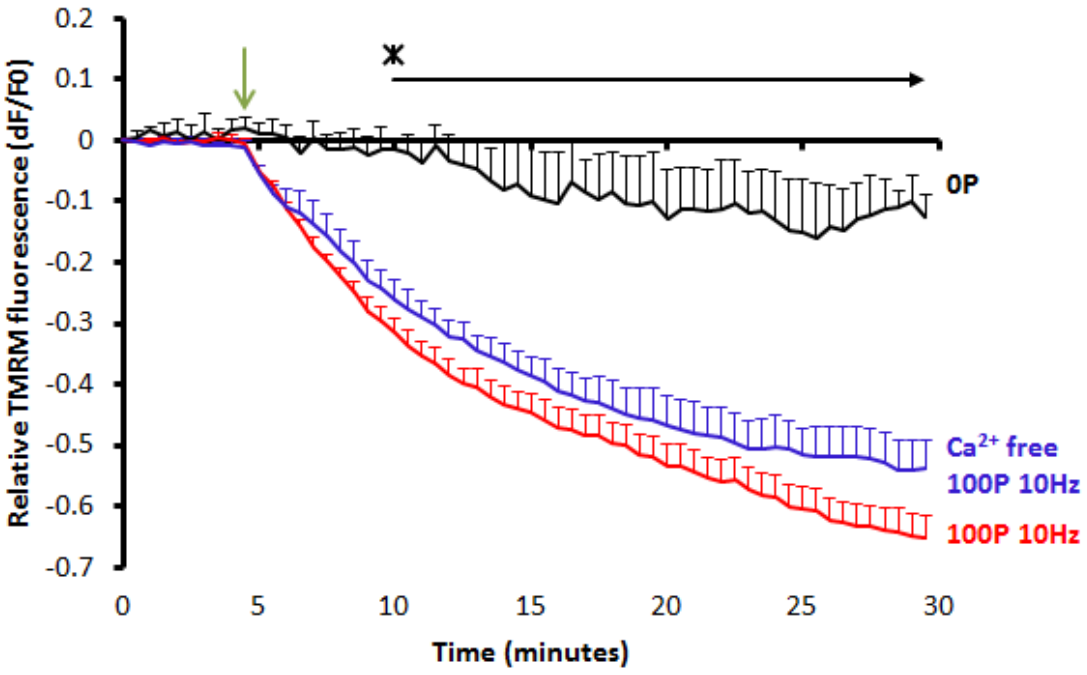

Figure 22. Loss of $\Delta\Psi_m$ is not caused by calcium.

100, 10 ns pulses delivered at a frequency of 10 Hz applied to U87 cells loaded with TMRM in either Ca^{2+} HBSS (red line, n = 7) or in Ca^{2+} free HBSS (blue line, n = 4) and the non-pulsed control (black line, n = 3). Asterisk indicates a significant difference between pulsed conditions and control and no significant difference between the two pulsed conditions, two way repeated measures ANOVA with Bonferroni test f (4.23, 18.35) = 11.49, $p < 0.05$. The green arrow indicates the start of pulse application and error bars show S.E.

Sodium influx has also been shown to cause depolarisation of the mitochondria[91]. Similar to the influx of extracellular calcium post pulse there is also likely to also be an influx of sodium. To ensure that this sodium is not responsible for loss of $\Delta\Psi_m$, cells loaded with TMRM were pulsed in a sodium free buffer which was osmotically balanced with choline. Following application of 100 pulses at 10 Hz no significant difference was found between the response in the presence of sodium and that in the absence of sodium (Figure 23).

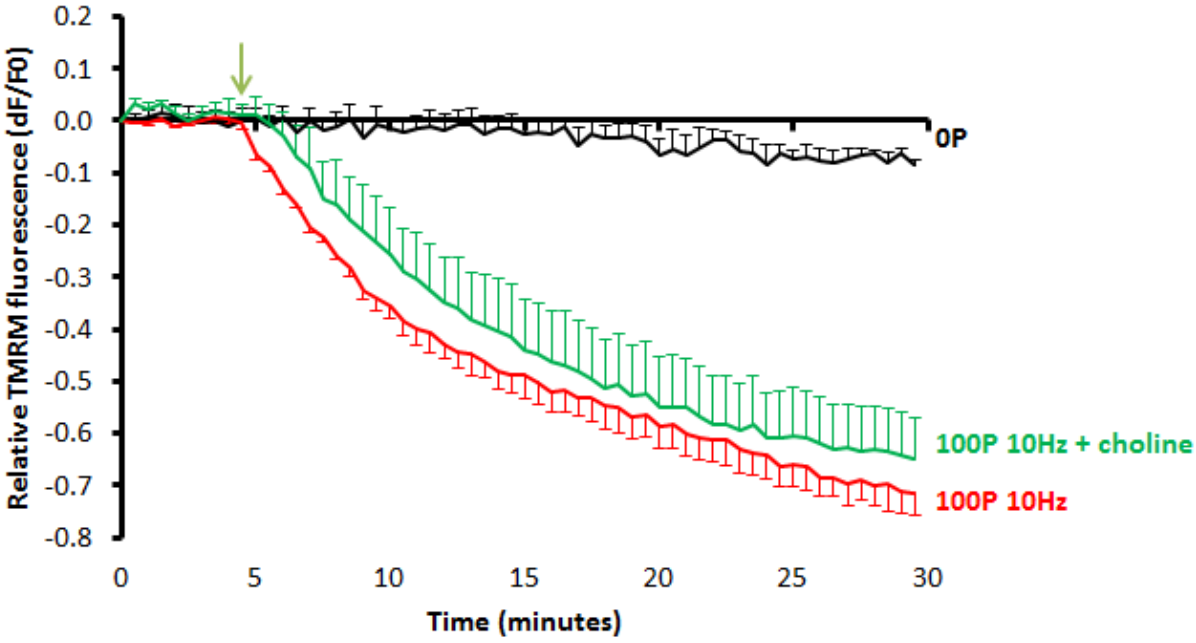

Figure 23. Effect of sodium on mitochondrial membrane potential following nsPEF treatment.

100, 10 ns pulses delivered at a frequency of 10 Hz applied to U87 cells loaded with TMRM and pulsed in normal HBSS (red line, n=4) or in choline HBSS (green line, n=4). The black shows the non-pulsed controls (n=3). There was no significant difference between either of the pulsed conditions as measured by two-way repeated measures ANOVA with Bonferroni tests, $F(3.05, 12.21) = 22.42$, $p > 0.05$. The green arrow denotes the start of pulse application and the error bars show S.E.

2.4. Discussion

The effect of our nsPEF exposure on plasma membrane poration in U87 cells is largely in agreement with previously published work. We found that one pulse was sufficient to allow limited uptake of the dye and, in agreement with published data[17,57], increasing the number of pulses resulted in more dye uptake. Dye uptake occurred most rapidly in the period during/ immediately after pulse application before plateauing. This suggests that the uptake is either actively facilitated by the pulse, for example by electrophoretic transport[92], or that the duration that the pores are open is limited[17]. Confirmation of the duration of pore opening could be determined by infusing YO-PRO-1 into the imaging buffer at different post-pulse time points. The increased dye uptake with increasing pulses suggests that either there is an increased number of pores and/or that there is an increase in pore size. Whilst we did not further investigate this published data supports the idea of increasing numbers of pores[57].

Whilst total YO-PRO-1 uptake has previously been shown to depend on frequency of application[93], we have shown that there is also a relationship between frequency and rate of YO-PRO-1 uptake, best demonstrated by the results for 100 pulses where 1 Hz application resulted in a sigmoidal curve and the 10 and 100 Hz applications in hyperbolic curves. This can perhaps be explained by the pulse being shorter than the charging time of the plasma membrane, which is estimated to be around 100 ns[76]. Work in our lab has shown that the change in membrane voltage potential following the application of a single 10 ns pulse only returns slowly (minutes) to resting values, and that application of a second pulse causes a cumulative effect on the voltage potential. It could be imagined therefore that a certain number of pulses, attained more rapidly with the faster frequencies, are needed for an appreciable level of poration to occur. The polar entry of YO-PRO-1 agrees with published data[93] and suggests that the membrane nearest to the electrodes is more prone to poration.

Nanoporation following nsPEF is a widely accepted phenomenon within the nanopulse community, as such there has been little investigation into the possibility of other explanations for the uptake of membrane impermeable dyes. We looked at the possibility of involvement of the P2X7R and certain TRP channels, using different inhibitors of the channels. We were able to block YO-PRO-1 uptake following 1 pulse with the P2X7R inhibitor probenecid. Probenecid is believed to have a dual action on P2X7R with evidence of a direct inhibitory effect[63] as well as blocking Pannexin-1 channels[94], which are thought to be implicated in the receptors secondary permeability state that gates YO-PRO-1. This mode of action, involving Pannexin-1 inhibition, is different to A-438079, a competitive antagonist of P2X7R[95], which perhaps explains why it failed to block dye uptake. At higher pulse numbers (100 pulses at 10 Hz) probenecid failed to have any effect on uptake suggesting the possibility of different mechanisms of dye entry with a dilation of P2X7R channels at low pulse numbers and nanoporation occurring at higher pulse numbers. Both the need to inhibit Pannexin-1 and too high pulse numbers could explain Vernier *et al.*[93] results where they ruled out P2X7R's involvement after applying 30, 4 ns pulses at 1 kHz to cells incubated with brilliant blue, a non-competitive antagonist of P2X7R.

Whilst the preliminary results presented here were unable to show any effect of TRP inhibitors on YO-PRO-1 uptake further work could be envisaged including monitoring uptake following the application of a single pulse and perhaps using a combination of inhibitors in case more than one TRP channel is involved.

The initial strategy we used to investigate post pulse changes in intracellular calcium, applying a single pulse and imaging every 30 seconds, proved to be inadequate to capture any reproducible result. The application of one 600 ns, 40 kV/cm pulse has been shown to cause an increase in intracellular calcium that persists 10 minutes after pulse application[24] and a single 60 ns pulse of 30 kV/cm results in an increase lasting for at least 150 seconds[33]. It is therefore possible that for a single pulse a longer pulse duration than our 10 ns or a higher electric field is needed to elicit a change, supported by data that shows a 112 kV/cm, 10 ns pulse is needed to produce the same calcium response as a 12 kV/cm 60 ns pulse[54].

By increasing the number of pulses to 100 applied at 10 Hz we were able to induce a rapid and sustained rise in calcium levels as measured by two different calcium indicators. The presence of EGTA to the extracellular buffer completely eliminated this calcium response, with the additional depletion of intracellular calcium stores with thapsigargin showing the same effect as with EGTA alone. This suggests that the source of calcium was extracellular and not intracellular. Whilst this is in agreement with some published data[24] it is at odds with others that show evidence of calcium release from intracellular stores in addition to influx from the extracellular buffer[31–33,96] and a study that shows 10 ns pulses are more efficient at releasing intracellular stores than longer pulses[54]. The pulse conditions used in our experiments were however more intense, 100 pulses at 10 Hz, when compared to those used in the cited studies where generally a single pulse was applied. As shown by our earlier results the pulse conditions we used caused more membrane permeabilisation than a single pulse, it is therefore possible that there was an influx of EGTA following the pulse that would have masked any intracellular release. Repeating these experiments with a lower number of pulses may reveal an intracellular calcium source. Of the two calcium indicators used FLUO-4 was more adapted to our needs as it allowed faster imaging without photobleaching. An imaging system that allowed the exploitation of Fura Red's ratiometric qualities would give further useful data by allowing the quantification of the calcium concentration within the cell, as previously done by Semenov *et al.*[31] with Fura-2.

Applying 100 pulses at 10 Hz to U87 cells caused the immediate onset of a gradual decrease in $\Delta\Psi_m$ that showed a dose-response relationship with applied electric field. A similar electric field dependent effect has been shown with 600 ns pulses, using a single time point measurement[24]. Here, as with our results, a threshold electric field value (30 kV/cm) had to be attained in order to cause $\Delta\Psi_m$ dissipation. The same study also showed that dissipation was dependent on both time and calcium. They propose that this effect is not due to nanoporation

of the mitochondrial membrane, which would cause an immediate loss in $\Delta\Psi_m$, but instead due to increased calcium uptake into the mitochondria, in response to increased intracellular levels, resulting in the opening of the mitochondrial permeability transition pore. Whilst our results showed time dependency, they are not calcium dependent suggesting a different mechanism is involved. We also looked at the possibility of sodium causing the loss of $\Delta\Psi_m$[91] but found no link perhaps reflecting a lack of sodium influx following nsPEF that has been previously reported[32].

Mitochondrial depolarisation has been shown to occur at lower pulse counts than plasma membrane permeabilisation[23] further investigating this with our pulse system could be an interesting future experiment. The nsPEF induced loss of $\Delta\Psi_m$ has been shown to be associated with increased mitochondrial membrane permeability[22] which results in the release of cytochrome C[81] and therefore a key step in nsPEF induced apoptosis. Further investigation into this could also be envisaged.

In general our pulse generating system was able to reproduce similar responses in our U87 cells as those that have previously been published. A pulse application regime of 100, 44 kV/cm, 10 ns pulses applied at 10 Hz was found to induce reproducible results in all cellular responses of interest.

Chapter 3:

The effect of nsPEF on microtubules

3. The effect of nsPEF on microtubules

3.1. Introduction

nsPEF have been shown experimentally to have a direct effect on protein structure with a resulting effect on the protein's function[97]. Microtubules (MT) form part of the cytoskeleton and are filamentous, polar, protein structures. Purified MT have been shown to align with an electric field[98,99] and, in cells, electric fields can disrupt microtubule polymerisation[100]. Theoretical simulations also suggest that MT possess electromechanical properties in the microwave range[101]. Many of the downstream events following MT depolymerisation parallel those seen following nsPEF treatment. Given all this it was therefore of interest to us to see if nsPEF had an effect on MT stability.

3.1.1. Microtubule function

Microtubules are essential to many cellular functions. They play a key role in cell division in both spindle formation and cytokinesis. They provide a track for cellular transport of vesicles and proteins and are also involved in changes of cell shape leading to cell motility and migration[73,102]. The depolymerisation of MT is also a key event in apoptosis[103].

3.1.2. Microtubule structure and dynamics

Microtubules are hollow, cylindrical, protein structures that are composed of repeating α and β- tubulin heterodimers. The heterodimers, with a molecular weight of 110 kDa[104], bind head to tail to form strands called protofilaments. In mammalian cells 13 of these protofilaments self-assemble to make a MT (Figure 24). Forming part of the cell cytoskeleton, along with microfilaments and intermediate filaments, they are highly dynamic structures subject to constant lengthening and shortening. In interphase cells they are nucleated by γ-tubulin in microtubule-organising centres (MTOCs) and grow out towards the cell periphery. The protofilaments are polarised structures with the β- tubulin monomer pointing towards the growing plus-end and the α- tubulin monomer forming the negative-end that points towards the MTOC.

Each β- tubulin monomer contains a GTP binding site. Heterodimers with GTP bound to the β- tubulin monomer are able to attach to growing MT in a process called polymerisation. If

the GTP on the heterodimers at the MT growing tip is hydrolysed to GDP then the MT begin to rapidly depolymerise[105,106]. The dynamics between polymerisation and depolymerisation can be altered chemically. The drugs vinblastine, nocodazole and colchicine are microtubule-destabilising agents which prevent polymerisation of MT and at high enough concentrations cause depolymerisation. Paclitaxel is a microtubule-stabilising agent which blocks MT depolymerisation and at high concentrations enhances polymerisation (Figure 25).

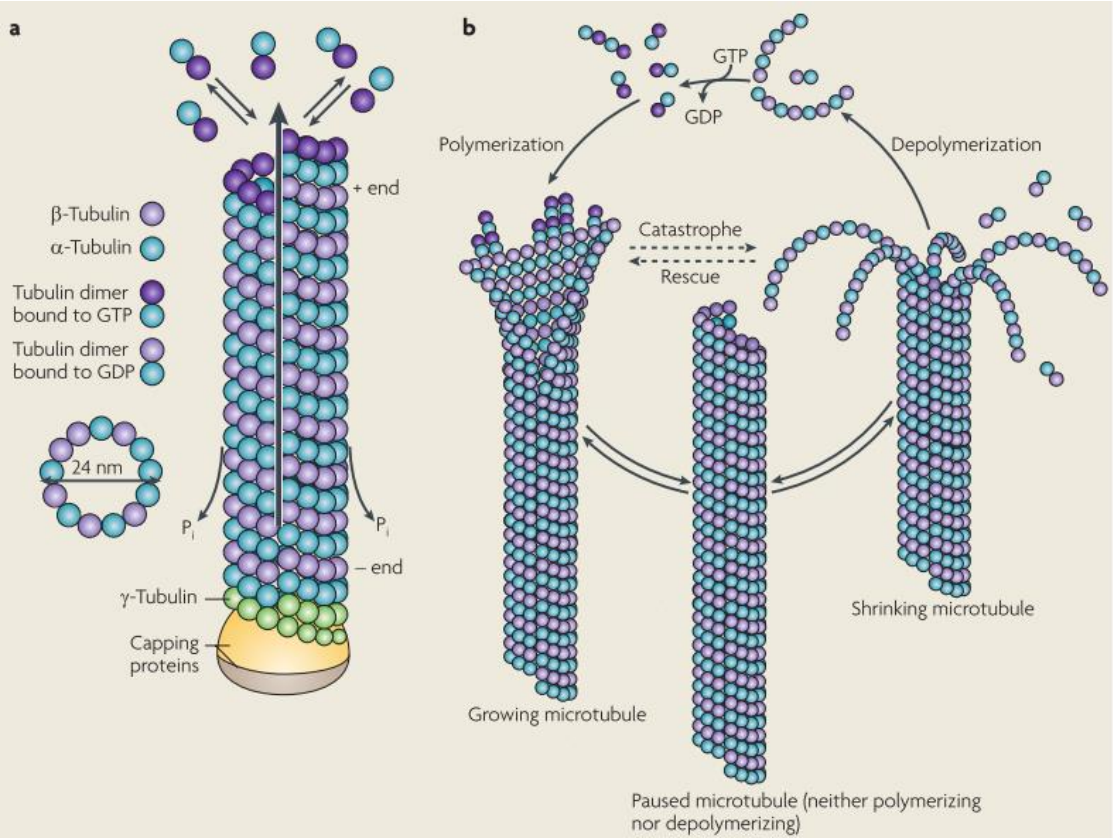

Figure 24. Structure and dynamics of microtubules.

MT are nucleated in the MTOC from γ-tubulin that has been stabilised by a complex of capping proteins. MT are made up of 13 protofilaments that have been formed from heterodimers of α and β- tubulin. They are dynamic structures which are constantly shrinking and growing. Growth is dependent on the maintenance of a bound GTP to the plus-end, terminal β- tubulins. Hydrolysation of these GTPs to GDP results in the rapid onset of depolymerisation (Figure from: Conde & Cáceres 2009[106]).

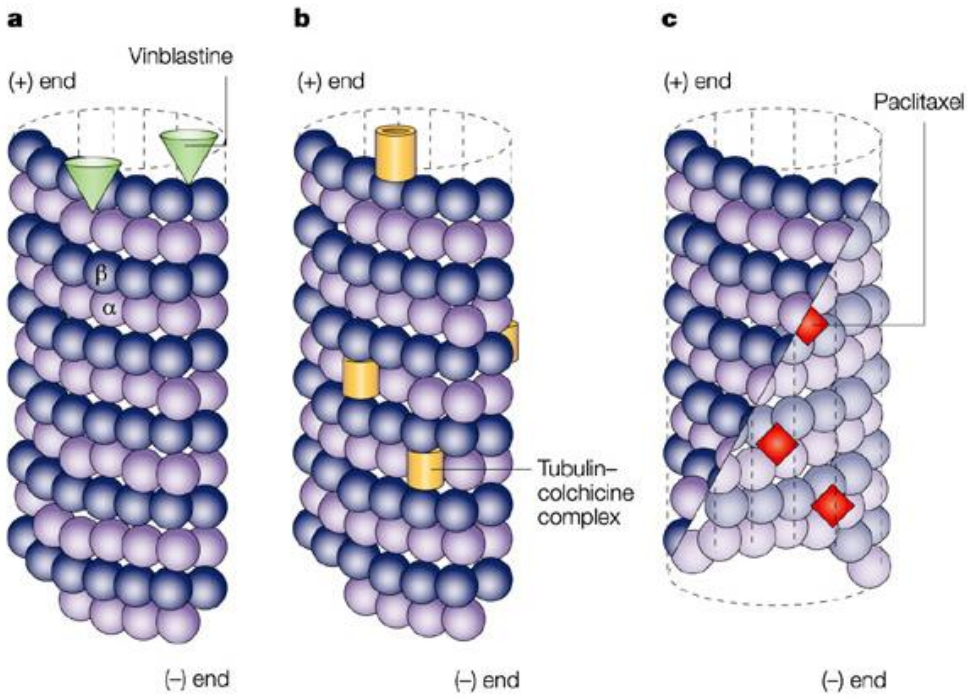

Figure 25. Binding sites for microtubule stabilising and destabilising drugs.
a: Vinblastine binding site; b: colchicine binding site; c: paclitaxel binding site (Figure from: Jordan & Wilson 2004[107]).

3.1.3. Microtubule associating proteins

The dynamic nature of MT needs to be tightly regulated in order for them to carry out their many cellular roles. This regulation is carried out by a large range of microtubule associating proteins (MAPs). MAPs can be divided into several categories: structural/stabilising, severing/destabilising, motor proteins and plus TIP. Structural MAPs include the neuronal proteins MAP2 and tau and the non-neuronal protein MAP4. By binding to MT they help hold the protofilaments together, suppressing catastrophes and increasing growth speeds[105,108,109]. These proteins are regulated by their phosphorylated state, with phosphorylation causing their release from the MT[109]. Structural MAPs also provide space around the MT to allow cellular transport along the microtubule by the motor proteins dynein, dynactin and some kinesins. MAPs that destabilise MT include the non-motor kinesin-13 family which enzymatically promote catastrophe and stathmin which sequesters free tubulin thus reducing the amount available for polymerisation[108,109]. Severing MAPs such as katanin, spastin and fidgetin are enzymes that cut the MT lattice with roles in mitosis and cilia biogenesis[110]. Plus TIP proteins

bind to the growing tip of the MT and have roles in promoting polymerisation (XMAP215), stabilising the newly formed microtubule (EB family) or providing MT stabilisation by forming an interaction with the cell cortex[108,109,111].

3.1.4. Role of microtubules in apoptosis

As summarised in Figure 26, MT have an important role in apoptosis. As an early event in the execution phase of apoptosis the interphase microtubule network is depolymerised and subsequently replaced by a novel, densely packed microtubule array that features rigid cellular spikes. This array facilitates cell blebbing, fragmentation and provides anchorage for phagocytic cells[112,113]. Depolymerisation leads to the release of proteins that are normally sequestered on microtubules, some of which are linked to apoptosis. These include: (1) Protein phosphatase 2A which dephosphorylates and inactivates the anti-apoptotic protein Bcl-2[112,114]; (2) Pro-apoptotic Bim, whose release causes the activation of Bax[115]; (3) Pro-apoptotic Bak[115]. Both Bax and Bak are able to integrate into the mitochondrial membrane where they form homo-oligomers which cause the loss of membrane integrity and subsequent loss of mitochondrial membrane potential[116].

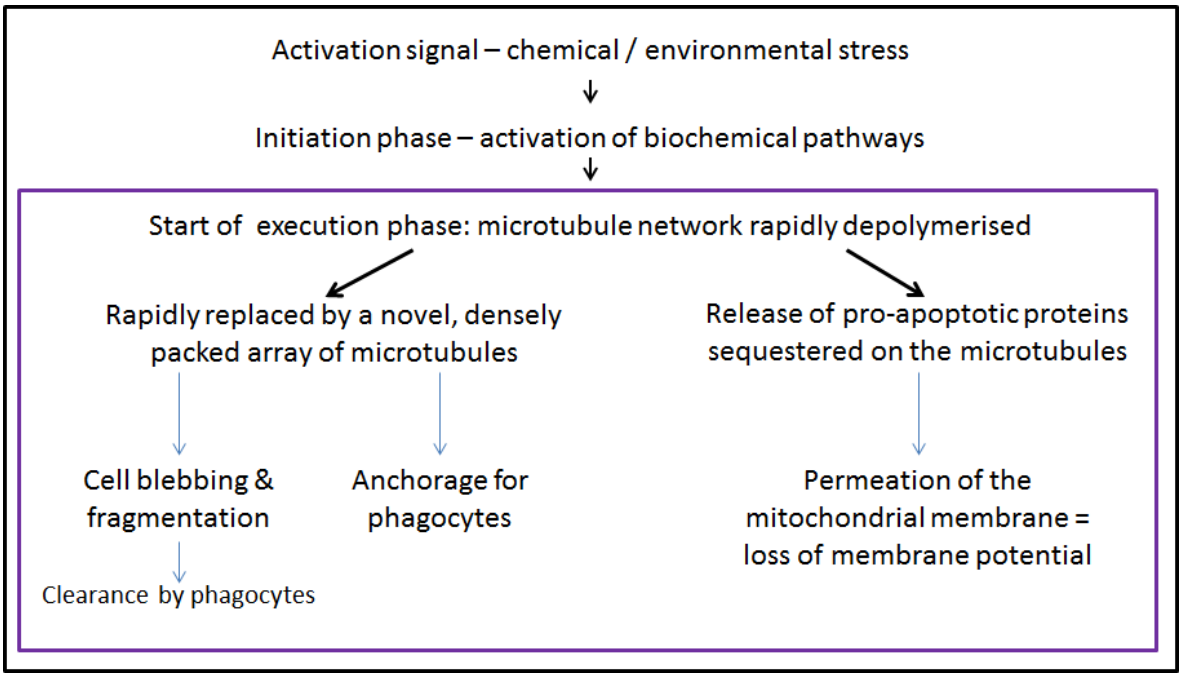

Figure 26. Summary of the role of MT in apoptosis.

The execution phase is denoted by the purple box.

3.1.5. Effect of electric fields and nsPEF on microtubules

Microtubules have a large surface area and a high negative electrostatic charge density which together give the potential to interact with electric fields[117]. It has been shown, *in vitro,* that purified microtubules will align with and can be moved by an electric field[98,118,119] and that electric fields can disrupt microtubule polymerisation in cells[100]. Microsecond pulses, such as those used for electroporation, when applied to cultured endothelial cells, have been shown to cause a breakdown of the microtubule network within five minutes of pulse application[120]. This breakdown was more pronounced at higher voltages (60 V) and was transient with recovery seen within two hours.

Given this, it is therefore probable that nsPEF could have an effect on microtubules. In plants, nsPEF have indeed been shown to cause a loss of the cortical microtubule network[121]. This breakdown was linked to a direct effect of nsPEF on a plasma membrane signalling hub formed from a KCH kinesin, that crosslinks microtubules to actin, and phospholipase D (PLD). Cortical microtubules are, however, plant specific and whilst depolymerisation of microtubules, post nsPEF application, has recently be shown in animal cells, it was believed to be due to influx of calcium, which destabilises microtubule, as opposed to a direct effect of the pulse[122].

Whilst breakdown of the microtubule-actin crosslinks has been proposed to explain the effect in the plant model, the involvement of phospholipases may also of interest. In plants PLD activation has been shown to cause microtubule depolymerisation [123], whereas in animal cells the same effect is seen when PLC is activated by carbachol stimulation of the M1 Muscarinic acetylcholine receptor (hM1)[124,125]. This effect has been linked to either the increase of calcium caused by PLC activation or the activation of GTPase, by the α subunits of G proteins, which results in loss of the GTP cap on the plus end of growing microtubules[126]. Interestingly, CHO cells exposed to a single 600 ns pulse have recently been shown to exhibit hM1-like signalling[127].

3.1.6. Microtubule depolymerisation and membrane poration

Disruption of the microtubule network has been shown to have an effect on membrane permeability. A link between sonoporation-mediated plasma membrane permeabilisation and MT depolymerisation has been demonstrated[128] and cells have been shown to become more permeable when their MT are disrupted by a mechanical force[129]. Pore resealing is also

dependent on microtubule integrity[130]. Microtubules form interactions with many membrane associated proteins including certain TRP channels[131,132], septins[133] and metabotropic glutamate receptors[134]. It therefore seems possible that breaking these interactions could result in channel opening or pore formation.

3.1.7. Microtubule depolymerisation and increase in intracellular calcium levels

Increases in cytosolic calcium have been observed following chemical-induced depolymerisation of microtubules. On addition of nocodazole, dendrites, loaded with the Ca^{2+} indicator dye FLUO-3, showed an immediate, but slow, increase in fluorescence. The increase, which corresponds to an increase in $[Ca^{2+}]_i$, continued over the 7 minute experimental period [135].

Whilst Ca^{2+} may simply enter the cells through microtubule depolymerisation-induced plasma membrane pores it is also possible that Ca^{2+} channels are opened by MT depolymerisation. The opening of Ca^{2+} influx channels in the plasma membrane during CCE (see section 2.1.3.2) is dependent on two families of proteins STIMs and Orias. The STIMs (STIM 1 and 2) are Ca^{2+} sensors that, under normal conditions, are located diffusely throughout the ER but reposition to the regions of the ER that are close to the plasma membrane when the concentration of Ca^{2+} in the ER drops. Proximity to the plasma membrane allows STIMs to interact with and activate Orias, which are the pore-forming subunits of the CCE channels[136]. A proportion of STIM1 present in the ER is thought to be located in vesicular sub-compartments that move along MTs powered by kinesin, a plus-end directed motor protein. Depolymerisation of MT by nocodazole, in a GFP-STIM1 DT40 chicken B-cell line, caused the formation of STIM1 puncta, reminiscent of those seen during CCE, near the plasma membrane[137,138]. It was later shown in STIM1 overexpressing HEK 293 cells that the formation of these puncta, induced by nocodazole, was able to induce activation of CCE. However, the same treatment in cells with normal expression of STIM1 did not result in CCE activation[139]. However, many cancer cell lines, including the human glioblastoma cell line used in this study, have an increased expression of STIM1[140].

3.1.8. Effect of calcium on microtubule dynamics

Calcium itself has been shown to cause the depolymerisation of MT. Work using purified tubulin, polymerised *in vitro*, suggests that calcium increases the catastrophe rate but not the

growth rate of MT. It is proposed that Ca^{2+} is able to affect the rate of GTP hydrolysis on the plus end GTP cap[141].

Ca^{2+} also activates a family of cysteine proteases called calpains. Tubulin is one of the substrates of calpains I and II. These proteases are able to prevent the *in vitro* polymerisation of purified tubulin and are able to cause the depolymerisation of *in vitro* purified microtubules[142]. Increases in $[Ca^{2+}]_i$ induced by nsPEF have been shown to cause a 1.7 fold increase in basal calpain activity when tested an hour after pulse exposure[81].

3.1.9. The effect of microtubule depolymerisation on mitochondrial membrane potential

Microtubule depolymerisation has been shown to cause a decrease in $\Delta\Psi_m$ and as demonstrated in the previous chapter (Figure 21) our nsPEF pulse regime also causes loss of $\Delta\Psi_m$.

In brain stem pre-Bötzinger complex neurons (excitable cells) taxol and nocodazole which respectively stabilize and depolymerize MT were found to cause loss of $\Delta\Psi_m$. Taxol caused an almost instantaneous loss of $\Delta\Psi_m$ whereas nocodazole caused a more gradual decrease in $\Delta\Psi m$[135]. By using inhibitors of the mitochondrial permeability transition pore (mPTP) the authors propose that for both drugs, loss of $\Delta\Psi_m$ is due to opening of mPTP, an event which also leads to the release of mitochondrial proapototic factors such as cytochrome C.

Similar results have been shown in the non-excitable Hep G2 human liver carcinoma cell line, where the treatment of cells with either colchicine or nocodazole caused a decrease in $\Delta\Psi m$[143]. In contrast, they found that taxol caused an increase in $\Delta\Psi_m$. They concluded that free tubulin regulates $\Delta\Psi_m$ by binding to voltage-dependant anion channel (VDAC) and blocking the ATP/ADP exchange through this channel[144,145]. Other cancer cell lines, A549 adenocarcinomic human alveolar basal epithelial cells and UM-SCC-1 upper aerodigestive tract carcinoma cells tested in the same study also linked MT depolymerisation to loss of $\Delta\Psi_m$. Reduction in oxidative phosphorylation and a decrease in mitochondrial outer membrane permeability, leading to a release of apoptotic signals are proposed implications of the VDAC closure by tubulin[146].

As discussed previously (section 3.1.4) MT depolymerisation also leads to the release of proapoptotic proteins that are normally sequestered on the MT. Pores formed by these proteins in the mitochondrial membrane could also explain loss of $\Delta\Psi_m$.

3.1.10. Live cell imaging of microtubules and their dynamics

3.1.10.1. End binding proteins

End binding proteins (EBs) are conserved in plants, yeast and mammals[147], with a mammalian expression of three different EBs (EB1, EB2 and EB3)[148]. They bind to the plus tips of growing microtubules and as such when fused with a fluorescent protein, such as GFP, they give a comet-like appearance that can be used to visualise microtubule growth dynamics[149,150]. EB proteins are made up of an N-terminal calponin homology domain, that binds to the microtubule, a C-terminal coiled-coil domain which allows dimerization of EB molecules and an acidic C-terminal tail[151,152]. This acidic tail binds to most other known plus tip proteins associating them with the microtubules[151].

EB proteins bind to microtubules through electrostatic interactions preferring tubulin in its GTP state over its GDP state[153], with an average of 270 EB1 dimers bound to the plus tip of growing microtubules in mammalian cells[154]. They bind to microtubules between the protofilaments, with each EB protein forming a contact with four tubulins and this crosslinking of tubulin makes the plus tip less susceptible to depolymerisation[155]. Microtubules with longer EB binding regions are more stable and microtubule catastrophe occurs when less than 15-30% of the binding region is occupied[111]. Under normal growth conditions EB proteins have been estimated to bind to the microtubule tip for about 8 seconds, resulting in faster growing microtubules having longer EB comets[150].

3.1.10.2. Tubulin

The visualisation of microtubules themselves is achieved through the incorporation of fluorescent tubulin units. This can be done by the covalent attachment of rhodamine or Cy3 to tubulin subunits which are then micro-injected into the cell. The labelled subunits are then polymerised into the microtubules before imaging[156–158]. A second method is to use cells that express, either stably or transiently, tubulin that is fused to a fluorescent protein such as GFP or RFP[159].

3.1.10.3. Using super-resolution microscopy to visualise microtubules

Resolution is defined as the minimum distance necessary between two-point source objects for them to be distinguished from each other. The resolution obtained by an optical microscope is limited by the diffraction of the waves of light as they pass through the aperture at the rear focal plane of the objective. The resolution limit was described by the Rayleigh criterion as: $r = \frac{0.61\,\lambda}{N\,A}$; where r is the resolution, λ is the wavelength of light and NA is the numerical aperture of the objective (Figure 27).

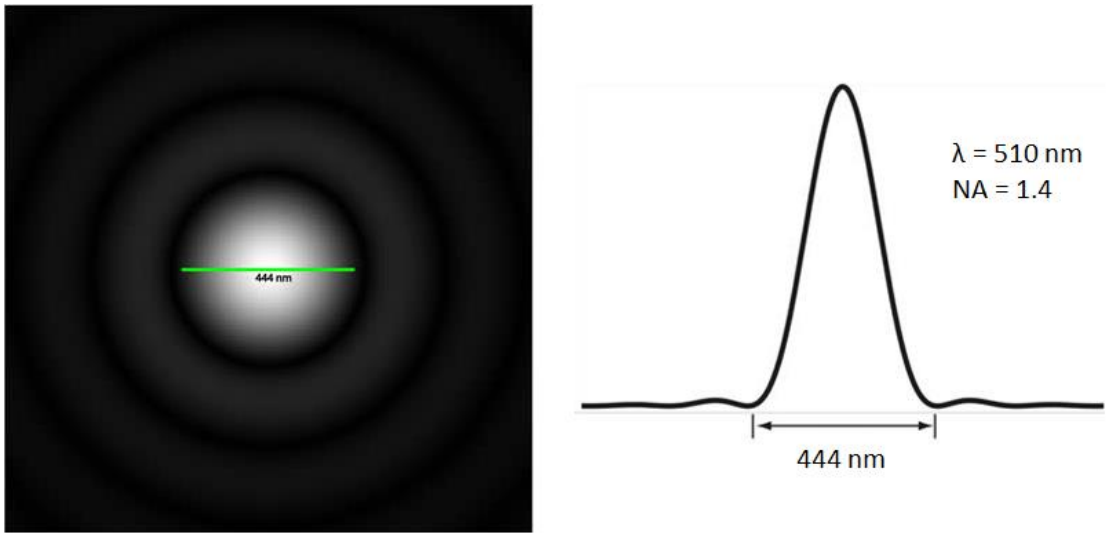

Figure 27. The effect of light diffraction on resolution.
The image on the left shows how diffraction affects the transmitted light from a single GFP molecule resulting in a pattern of a fuzzy circle and rings which are known as Airy disks. The profile pattern of this Airy disk is shown on the right. Using Rayleigh criterion based on an objective with a 1.4 numerical aperture the resolution is 222 nm. Image from[160].

With a standard optical microscope the resolution is therefore limited to 200 nm in the x-y dimension and 500-700 in z dimension[161]. Microtubules have a diameter of 25 nm and within the cell are tightly packed so the microscope set up at XLIM is unable to resolve them clearly. For better microtubule visualisation part of this thesis was carried out at the Advanced Imaging Centre at the Janelia Research Campus in Virginia, using a 3D structured illumination microscope (3D-SIM). 3D-SIM is one of several recent advances that allows super resolution microscopy, in the case of 3D-SIM resolutions of 100 nm (x-y) and 300 nm (z) are attained using a wide-field microscope[162,163]. In 3D-SIM a grid pattern is introduced into the focal plane and the interference of the grid with the diffusion of light from the

biological sample creates a Moiré fringe pattern that is collected by the objective. Due to this change in diffraction the Moiré pattern contains information about the sample that would not normally be seen (Figure 28) and this information is computationally extracted using algorithms developed by the group at Janelia. By rotating the grid 15 times, for each z stack, and combining the information contained in each of these 15 images the improved resolution is achieved.

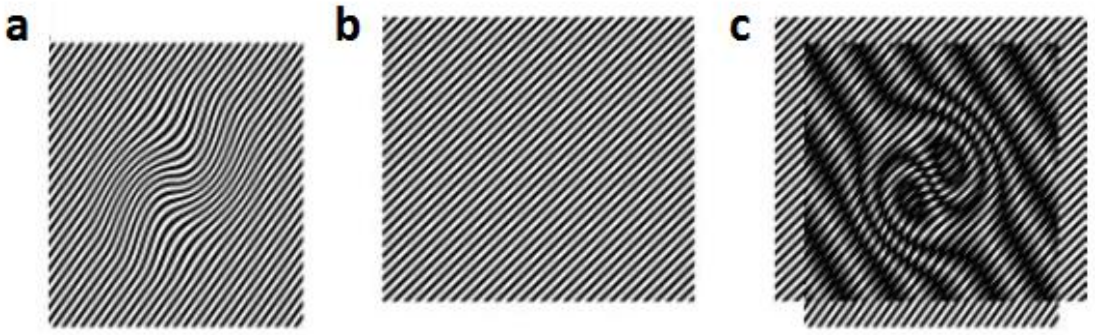

Figure 28. Improving resolution with Moiré fringes.
The improved resolution in 3D-SIM is based on the properties of Moiré fringes. A grid (b) is introduced into the focal plane and interferes with light emitted from the sample (a) resulting in a Moiré pattern (c) that contains otherwise unseen details about the sample. Image from[164].

3.1.11. Objectives

Microtubules are the main target of numerous chemotherapy treatments that work as antimitotics. These drugs, however, come with a range of side effects including neuropathies, immunosuppression, myelosuppression and gastrointestinal toxicity, some have even been linked to an increased expression of multidrug resistant proteins leading to tumour resistance[165]. Given that microtubule growth[100] and orientation[98,118,119] can be manipulated by electric fields, and supported by previous nsPEF studies into microtubules[121,122], this chapter aims to further explore the effects of nsPEF on the microtubule network and its growth dynamics. The disruption of the microtubule network by nsPEF could potentially be exploited as a locally administered antimitotic with reduced systemic side effects and lower resistance.

3.2. Material and methods

3.2.1. Cell culture

The human glioblastoma cell line U87 and U87 stably transfected with EB3-GFP and tubulin-RFP (U87-EB3-GFP-tubulin-RFP) were cultured in T75 flasks at 37°C, 5% CO_2 in MEM medium (Gibco, 10370-047) supplemented with 10% FBS (Gibco, 10500), 2 mM L-glutamine (Dutscher, X0550-100), 1.1 mM glucose (Invitrogen, 19002-013), 100 U/ml penicillin and 100 µg/ml streptomycin (Gibco, 15070-063). On reaching 80% confluence, cells were detached from the surface of the flask by washing twice with PBS (Gibco, 14190) and then incubating for 3-5 minutes at 37°C with trypsin (Gibco, 25200-056). Trypsin activity was stopped with the addition of an equal quantity of defined trypsin inhibitor (Gibco, R-007-100) and then centrifuged for 10 minutes at 600g. The resulting cell pellet was resuspended in MEM for use in experiments and for reseeding flasks.

3.2.2. Cell transfection

U87 cells were transfected using LentiBrite ™ EB3-GFP Lentiviral Biosensor and LentiBrite ™ RFP-Tubulin Lentiviral Biosensor (Merck Millipore, 17-10208 and 17-10205). U87 cells were seeded into a 35 mm sterile dish containing 2 ml of complete MEM medium at a density that gave 70% confluence after an overnight culture. The day following seeding the medium was replaced with fresh medium and stock from both lentiviruses was added to give a multiplicity of infection of 20 for each. Remaining lentiviral stock was aliquoted and stored at -80°C. Cells were cultured with medium being changed every 24 hours. On reaching confluence cells were transferred to and maintained in a T75 flask.

For wide-field imaging of mNeonGreen EB3 (Allele Biotechnology), cells were transiently transfected using Xfect Transfection Reagent (Clontech, 631318). Cells were seeded onto a 6 well dish so as to be at 50%-70% confluence the day of transfection. Following the manufacturer's protocol, for each well to be transfected, 5 µg of plasmid DNA was mixed with 100 µl Xfect Reaction Buffer, followed by 1.5 µl of Xfect Polymer. After an incubation of 10 minutes at room temperature the DNA / reagent mix was added dropwise to the well, mixed gently and incubated overnight under cell culture conditions. The culture media was replaced the following day and cells were plated onto imaging slides for use 48 hours after transfection.

For 3D-SIM experiments U87 cells were transiently transfected by electroporation with either mNeonGreen EB3, mEmerald tubulin or mEmerald-mito-7 (both from the Davidson collection). For transfection 2 µg of the desired DNA plasmid was mixed with 2 µl of cold salmon sperm DNA (Invitrogen, 15632011) and stored on ice. The salmon sperm DNA acted as a carrier during electroporation to increase protein expression[166]. A confluent T75 flask of U87 cells were detached by trypsin and spun down, as described in section (add document location). The resulting cell pellet was re-suspended in 400 µl of cold, serum free, Opti-MEM (Gibco, 31985062). 200 µl of this cell suspension was added to the tube containing the DNA, mixed once gently and incubated on ice for 5-10 minutes. The mixture was then gently transferred to a 0.4 mm Gene Pulser Electroporation Cuvette (Bio-Rad, 1652088) taking care to avoid introducing bubbles. After placing the cuvette into the ShockPod cuvette chamber of the Gene Pulser Xcell electroporating system (Bio-Rad, 1652660) cells were porated using an exponential decay pulse of 190 V and 950 µF capacitance. Following the pulse 2 ml of room temperature MEM was added to the cuvette and the cells were plated onto poly-D-lysine coated FluoroDishes (WPI, FD35PDL-100) and cultured for 24 – 48 hours before imaging.

3.2.3. Preparation of cells for wide-field live cell imaging

Cells were plated at a density of 1.8 x 10^5 cells/ml into 35 mm dishes, each containing a 22 mm poly-L-lysine (Sigma, P9155) coated glass coverslip (Dutscher, 140541DD), and incubated overnight. For imaging coverslips were removed from their dishes, sandwiched into plastic imaging chambers and covered in 1 ml of room temperature HBSS (NaCl 121 mM, KCl 5.4 mM, $MgCl_2$ 0.8 mM, $NaHCO_3$ 6 mM, D-glucose 5.5 mM, HEPES 25 mM, with either $CaCl_2$ 1.8 mM (Ca^{2+} HBSS) or EGTA 4 mM (Ca^{2+} free HBSS), pH 7.3). For measurement of intracellular calcium levels U87 cells were incubated for 30 minutes at room temperature, in the dark, in HBSS (Ca^{2+} or Ca^{2+} free) containing 1.25 µM Fura Red, AM (Life Technologies, F3020) or 0.5 µM FLUO-4, AM (Life Technologies, F14201), 0.02% pluronic acid (Life Technologies, P3000MP), then washed three times in the corresponding HBSS and incubated a further 30 minutes at room temperature. For measurement of cell membrane poration 1 µM of YO-PRO-1 (Life Technologies, Y3603) in Ca^{2+} HBSS was added just before imaging. To deplete intracellular calcium stores cells were incubated with 1 µM of thapsigargin (Sigma, T9033) in Ca^{2+} free HBSS for 30 minute before imaging. Microtubules were stabilised or destabilised by the addition of 10 µM paclitaxel (taxol) (Sigma, T7191) or

10 µM of colchicine (Sigma, C9754) 10 minutes before imaging. Mitochondrial membrane potential ($\Delta\Psi_m$) was measured by incubating cells with 10 nM TMRM (Interchim, FP-21089A) at room temperature, in the dark for 30 minutes, and washing three times in HBSS before imaging.

3.2.4. Preparation of cells for 3D-SIM live cell imaging

Before imaging culture medium was removed from the FluoroDish and replaced with 2 ml of Live Cell Imaging Solution (Life Technologies, A14291DJ) supplemented with 5.5 mM of glucose.

3.2.5. Wide-field live cell microscopy

Cells were observed by epifluorescence using a Leica DMI6000 microscope with a 100x objective. Fluorescent excitation was provided by a Spectra 7 light engine (Lumencor). Emitted light was filtered and captured on an electron-multiplying charge-coupled device camera (EMCCD; Photometrics Evolve 512, Roper) with 512 x 512 pixels. The system was controlled by, and images were captured with, Metafluor (version 7.8, Molecular Devices). Protocols for each experiment were first optimised to minimize illumination in order to reduce photobleaching. GFP (excitation: 475/25 nm; emission: 525/50 nm) and RFP (excitation: 542/27 nm; emission: 615/25 nm) had exposure times and source intensities of 50 ms, 10% and 20 ms, 25% respectively. Cells showing good expression of both GFP and RFP were chosen for imaging. Fura Red (excitation: 475/25 nm; emission: 615/25 nm) had an exposure time of 25 ms and 5% source intensity. FLUO-4 (excitation: 475/25 nm; emission: 525/50 nm) had an exposure time of 10 ms and 5% source intensity. YO-PRO-1 (excitation: 475/25 nm; emission: 525/50 nm) used an exposure time of 35 ms and 10% source intensity. TMRM (excitation: 542/27 nm; emission: 615/25 nm) had an exposure time of 10 ms and 5% source intensity. mNeonGreen (excitation: 475/25 nm; emission: 525/50 nm) had an exposure time of 50 ms and 10% source intensity. In all experiments a 2 x binning was used.

3.2.6. 3D-SIM

3D-SIM imaging experiments were performed on a custom system constructed at the Advanced Imaging Center of the Janelia Research Campus (Janelia HHMI, Ashburn, VA). The 3D-SIM microscope was based around a Zeiss AxioObserver microscope. A 488 nm

laser (Sapphire 488-500, Coherent) was used for fluorescence excitation. The laser was rapidly shuttered with an acousto-optic deflector (AA Opto Electronic) and the structured illumination was accomplished with a ferroelectric spatial light modulatator (SXGA-3DM; Fourth Dimension Displays). Fluorescent emission was collected with a Zeiss C-Apochromat water immersion objective (magnification of 63×, N.A. = 1.2) and Z sections were sampled with an axial step size of 125 nm. A sCMOS camera (Orca Flash 4.0, Hamamatsu) was used as the detect fluorescence after a dichromatic beam splitter (ZT405/488/561TPC-22.5deg; Chroma). All the system components were controlled with custom software written in Labview (National Instruments) and provided by the Janelia AIC. Complete details of the 3D-SIM microscope, method of structured illumination and the reconstruction algorithm have been described elsewhere[162,163,167].

3.2.7. *In vitro* polymerisation of rhodamine labelled tubulin

Purified, rhodamine-labelled microtubules were prepared using a Fluorescent Microtubule Biochem kit (Cytoskeleton Inc., BK007R). The lyophilised, rhodamine tubulin vial (20 µg) was reconstituted with 4 µl of cold General Tubulin Buffer containing 0.01 volumes of GTP and 1 µl of Microtubule Cushion Buffer and stored on ice. The lyophilised, unlabelled tubulin vial (1 mg) was reconstituted with 180 µl of cold General Tubulin Buffer and 20 µl of Microtubule Cushion Buffer and stored on ice. 2.5 µl of the unlabelled tubulin was mixed into 1 µl of the rhodamine tubulin and polymerised by incubating at 37°C for 20 minutes. Unpolymerised, reconstituted tubulin was aliquoted and snap frozen in liquid nitrogen before storage at -80°C. Following polymerisation microtubules were stabilised by immediately adding 100 µl of General tubulin buffer, containing 20 µM taxol, warmed to 37°C. The stabilised microtubules were then kept at room temperature for up to 24 hours or aliquoted and snap frozen in liquid nitrogen before storage at -80°C.

3.2.8. Imaging of rhodamine labelled microtubules

Microtubules were imaged in eight-electrode µ-slides (Ibidi, 82000). For imaging 2 µl of the stabilised microtubules were diluted in a mixture containing 20 µl of antifade, 200 µl of General tubulin buffer and 20 µM taxol, warmed to 37°C. This was added to the slide and imaged immediately. Polymerised microtubules were observed with the microscope set up described in section 3.2.5. The rhodamine was excited at 542/27 nm with an emission of

615/25. Images were taken every second for 100 captures, exposure time and laser intensity were 20 ms and 50% respectively and a 2 x binning was used.

3.2.9. Exposure of cells to nsPEF

100, 10 ns pulses, with an electric field strength of 44 kV/cm, were applied to cells at a frequency of 10 Hz using an nsPEF generator (FPG 10-1NM-T, FID Technology, Germany) with 50 Ω output impedance. A high-voltage measurement device (tap-off 245 NMFFP-100, Barth Electronics Technology, USA) connected to an oscilloscope (DPO 4104, Tektronix, USA) was used to visualize the time-domain measurements of the pulse[84–86]. Pulses were applied by positioning an electrode delivery system with a micromanipulator (Sutter MP285) comprising of two steel electrodes, separated by a gap of 1.2 mm and with 50 Ω impedance in parallel[37].

3.2.10. Image analysis

For wide-field live cell imaging experiments images were analysed using Image Analyst MKII (Image Analyst Software). Background was subtracted from the stack of images by manually drawing a region of interest (ROI) in a zone that did not contain cells and subtracting the grey level in this area from the rest of the image. Unless otherwise stated ROIs were then drawn to include the entire cell of interest and fluorescence intensity data for the ROIs were generated by Image Analyst MKII. Cell area was determined by drawing a free hand ROI around the perimeter of the cell and the corresponding area was calculated using ImageJ.

3D-SIM data was visualised using ImageJ (NIH). Microtubule plus end comet size was quantified from EB3 images from Z projected 3D-SIM stacks and thresholding before treatment with the “analyze particles” tool.

3.2.11. Statistical analysis

Statistical analyses were performed with OriginPro 2016 software. Datasets were first tested for normal distribution using Q-Q plots and a Levene’s test was used to assess the homogeneity of variance. Changes in fluorescence intensity were statistically tested over time (repeated measures) and between independent treatments (between groups) using a mixed-

model two-way repeated measures analysis of variance (ANOVA). The source of significant differences identified by ANOVAs was found using pair-wise post-tests that were Bonferroni corrected. Effects were considered statistically significant when the probability of falsely rejection the null hypothesis was less than 0.05 ($p<0.05$).

3.3. Results

3.3.1. Effect of different pulse regimes on microtubule dynamics

In order to test our hypothesis that nsPEF will disrupt the microtubule network we first looked at the effect of different pulse application regimes on EB3 dynamics. To do this U87 cells expressing EB3-GFP were treated with 1 pulse, 10 pulses applied at either 1 or 100 Hz or 100 pulses applied at 10 Hz (Figure 29). We observed that application of a single pulse or 10 pulses at 1 Hz failed to cause an obvious change to EB3 dynamics with comets remaining a similar size before and after pulse with no change in fluorescence levels. However, applying 10 pulses at a higher frequency (100 Hz) resulted in an increase in EB3 comet size occurring within the first 5 minutes following pulse application. Within the same time period 100 pulses applied at 10 Hz caused a reduction in the number of EB3 comets present associated with an increase in size of the remaining comets.

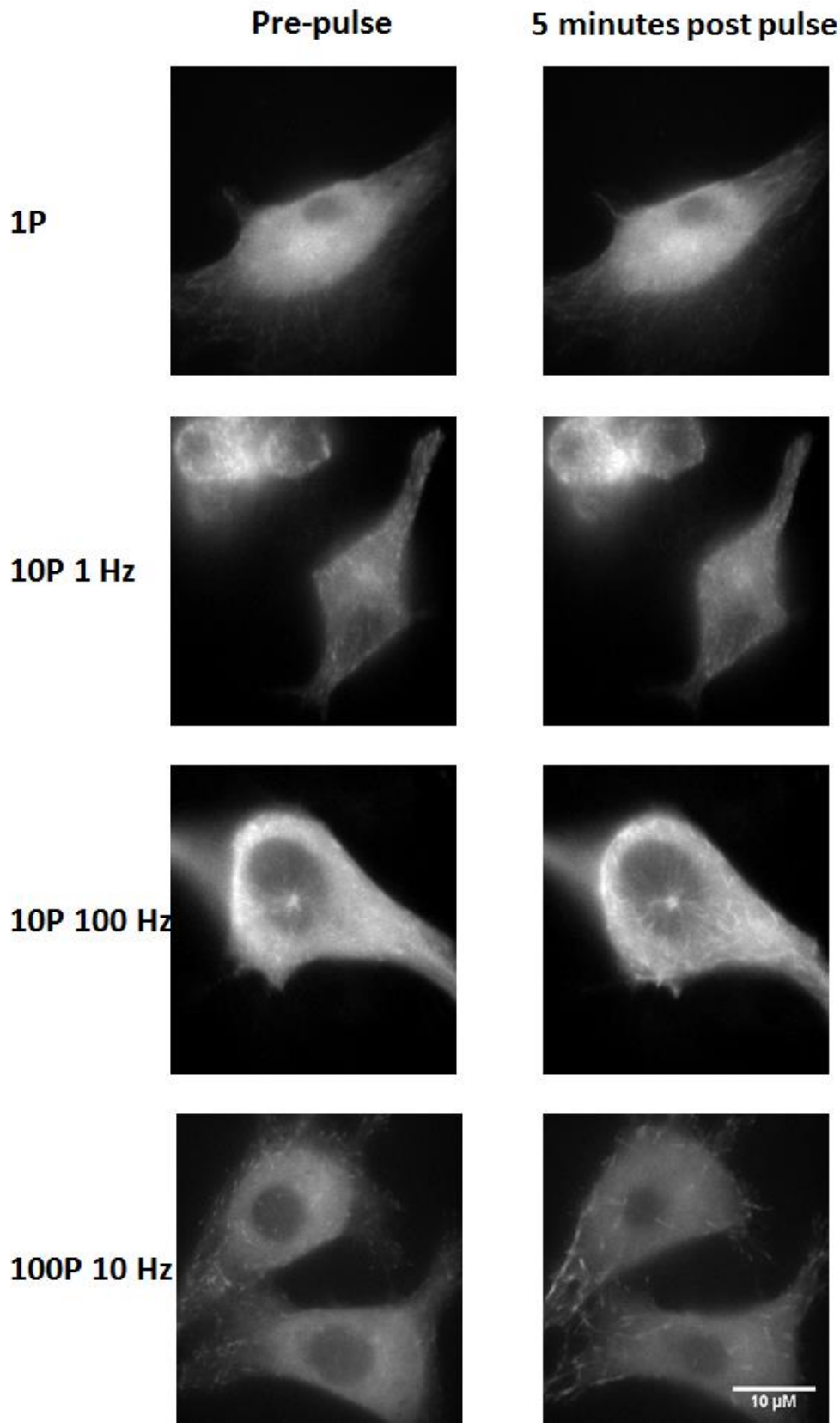

Figure 29. Representative images showing the effects of different pulse application regimes on EB3 dynamics.

3.3.2. Effect of nsPEF on the microtubule network and its dynamics

Given that 100 pulses applied at 10 Hz had a dramatic effect on EB3 dynamics we next used U87 cells expressing both EB3-GFP and tubulin-RFP to look at the effect of this pulse application regime on the interphase microtubule network. Cells were imaged every 30 seconds for a total of 24.5 minutes (50 image pair captures). Pulses were applied after 4.5 minutes (10 image pair captures) to give a baseline measurement. Changes in fluorescence were measured in a peripheral region, in the MTOC and in a central region of the imaged cell (Figure 30A). Control experiments, where electrodes were placed but no pulse was administered, showed stable measurements of both EB3-GFP and tubulin-RFP fluorescence levels, in all regions, throughout the imaging period (Figure 30B). Following pulse application both EB3-GFP and tubulin-RFP fluorescence in the central ROI started to decrease within the 30 seconds following the pulse, reaching a steady level within 10 minutes of the pulse. Decrease in EB3-GFP and tubulin-RFP fluorescence also occurred in the MTOC ROI with a delay of 2.5 minutes (EB3) and 3 minutes (tubulin) following pulse delivery. The decrease levelled off within 10 minutes of the pulse. In the peripheral ROI both EB3-GFP and tubulin-RFP fluorescence levels remained relatively stable for the whole imaging period with the exception of a transient increase in fluorescence immediately after the pulse, corresponding to a contraction of this region following the pulse. In contrast to this cytosolic clearance, both EB3 and tubulin show a post-pulse accumulation close to the plasma membrane (arrows Figure 30A). The increase in EB3 comet length is observable in the first image post-pulse and persists to the end of the imaging period.

a.

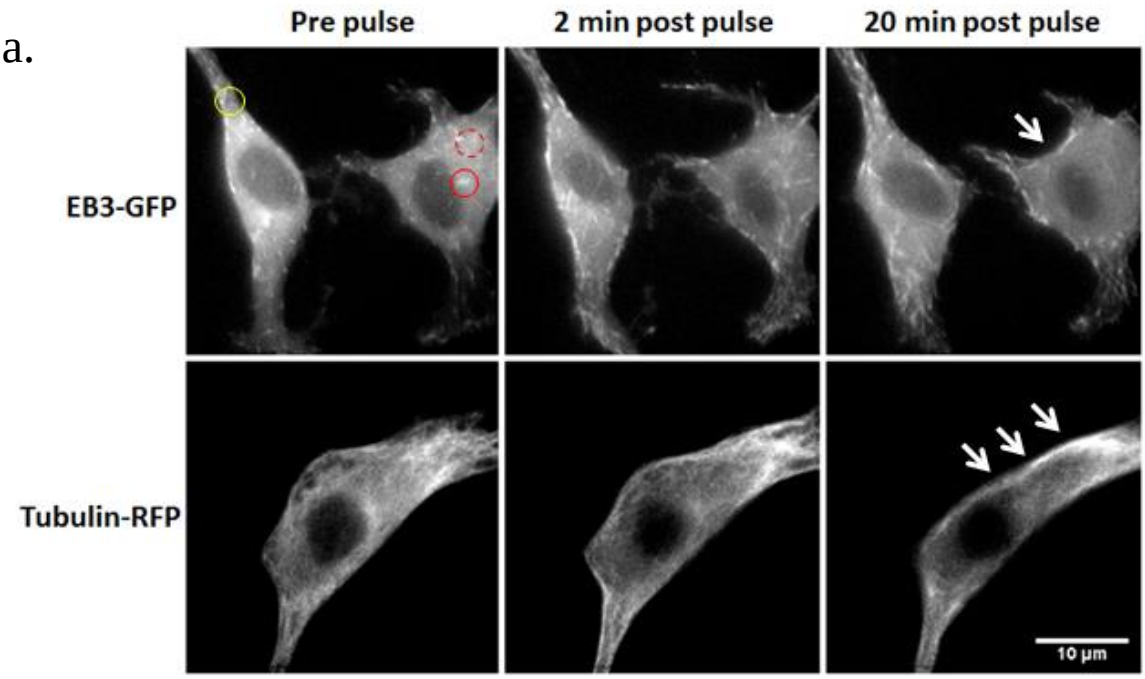
Pre pulse
2 min post pulse
20 min post pulse
EB3-GFP
Tubulin-RFP
10 µm

b.

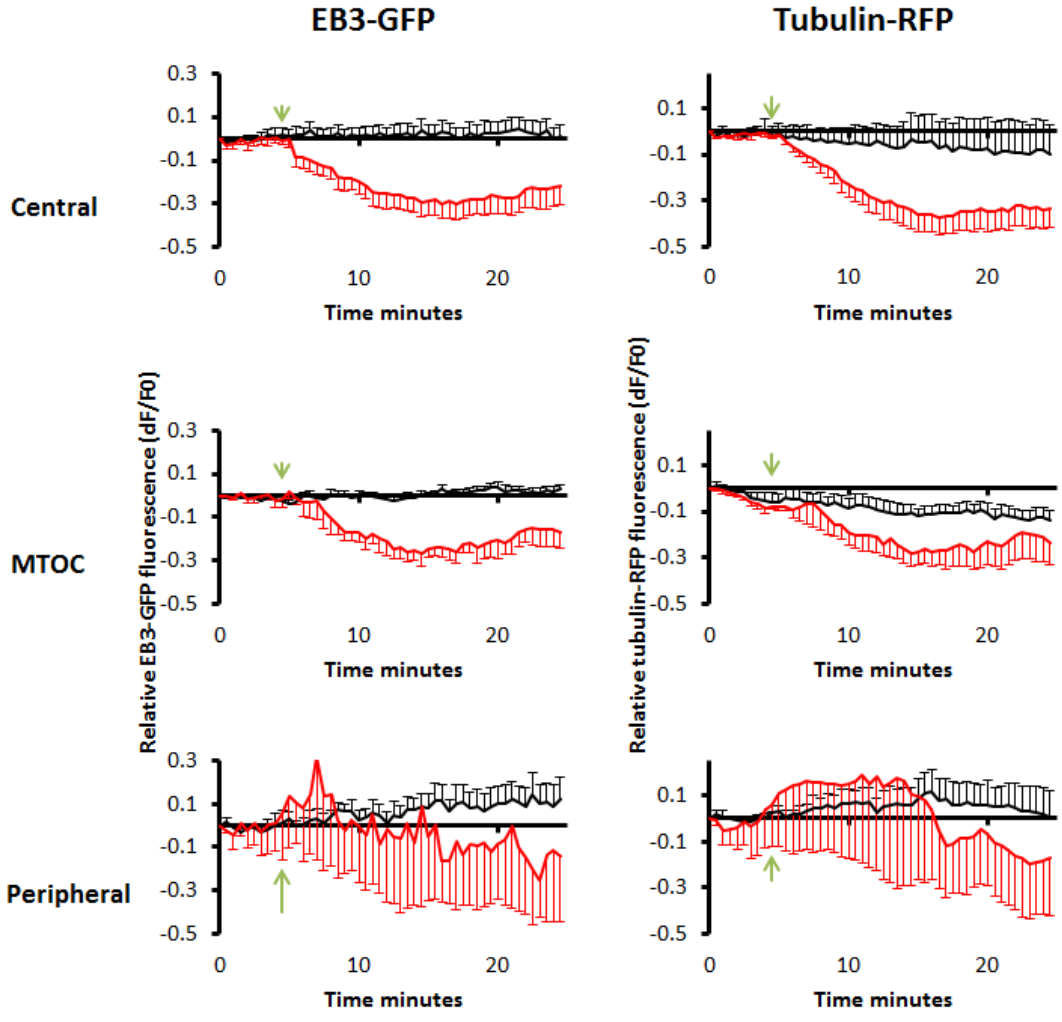
EB3-GFP
Tubulin-RFP
Central
MTOC
Peripheral
Relative EB3-GFP fluorescence (dF/F0)
Relative tubulin-RFP fluorescence (dF/F0)
Time minutes

Figure 30. 100, 10 ns pulses applied at a frequency of 10 Hz induces clearance of the microtubule network and disrupts microtubule growth.

A: representative live cell images of U87-EB3-GFP-tubulin-RFP cells before and 2 minutes after the application of 100, 10 ns pulses delivered at a frequency of 10 Hz. Circles show example ROIs: red solid = MTOC; red broken = central; yellow = peripheral.

B: Change in fluorescence over time plots for live cell imaging of U87-EB3-GFP-tubulin-RFP cells. For each of the three ROI for EB3-GFP (left) and tubulin-RFP (right) black lines denote averages for control experiments, where no pulse was applied and red lines denote averages for pulsed experiments; the start of application of 100, 10 ns pulses at 10 Hz is denoted by the green arrow. For control experiments: EB3 n = 7 and tubulin n = 5. For pulsed experiments: EB3 and tubulin central n = 4, EB3 and tubulin MTOC n = 3, EB3 peripheral n= 4, tubulin peripheral n = 5. Error bars show SE.

3.3.3. Determination of how quickly nsPEF affects microtubule dynamics

As both tubulin and EB3 fluorescence levels in the central ROI had decreased within the 30 second interval between pulse application and the subsequent image capture, we carried out faster imaging using U87 EB3-mNeonGreen cells to better determine the timescale of the onset of this decrease. Previous attempts at faster imaging with U87-EB3-GFP-tubulin-RFP cells resulted in photo bleaching. mNeonGreen is brighter than GFP[168] and therefore less illumination needs to be applied resulting in less photo bleaching and the fluorescence remaining stable throughout the imaging period (Figure 31). Unfortunately we had no photo stable alternative for imaging tubulin.

Cells were imaged every 2 seconds for a total of 178 seconds (90 image captures) and the pulse was applied after 24 seconds (13 image captures). A difference in the fluorescence signal in control and pulsed experiments is first observed 8 seconds after the beginning of pulse application, and by 44 seconds post pulse this difference is significant.

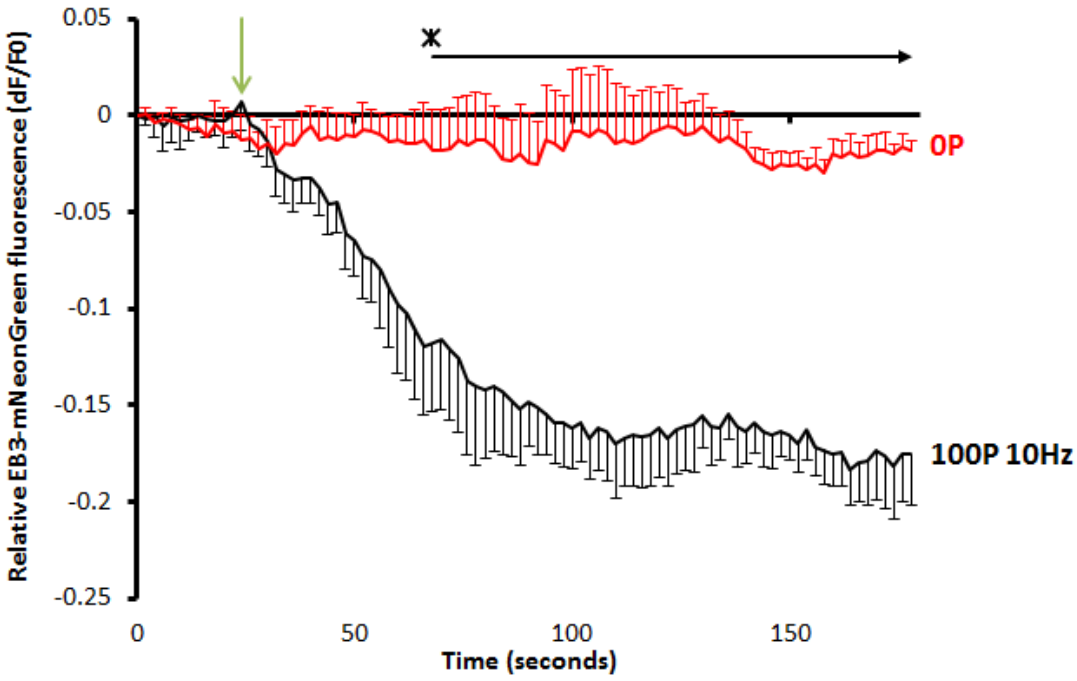

Figure 31. Faster imaging of EB3-mNeonGreen shows that microtubule growth in the central region is disrupted within 8 seconds of the application of 100, 10 ns pulses applied at a frequency of 10 Hz.

Red line denotes averages for control experiments (n = 4), where no pulses were applied and the black line denotes averages for pulsed experiments (n = 4). The start of application of 100, 10 ns pulses at 10 Hz is denoted by the green arrow. Asterisk indicates a significant difference between control and pulsed experiments, as reported by two-way repeated measures ANOVA with Bonferroni tests, $F(2.06, 12.38) = 17.88$, $p < 0.05$.

3.3.4. EB3 comet size increase following application of 100 pulses at 10 Hz

We next sought to better understand the post-pulse increase in EB3 comet length with the aims of both quantifying the increase and determining its time frame. Whilst wide-field imaging of cells expressing EB3-GFP clearly shows a post-pulse increase in comet size, the resolution and background fluorescence make it insufficient to allow for quantification of the increase. We overcame this by using 3D-SIM, a type of super-resolution microscopy, which uses structured illumination to allow the resolution to be doubled[163] (Figure 32). 3D-SIM uses considerably higher levels of illumination than wide-field microscopy which would have

resulted in photo bleaching of GFP. We therefore used cells expressing EB3-mNeonGreen, as it 1.5-3 times brighter than GFP, which allowed us to limit illumination as much as possible[168]. We found that 60 seconds after pulse application EB3 comets were 47.8 ± 4.4 % (n=11) larger than the pre-pulse comets compared with non-pulsed controls which had a 4.1 ± 3.0 % (n = 4) decrease in size over the same time period (mean ± SE). This size difference was significant; $t(13) = 6.79$, $p < 0.0001$.

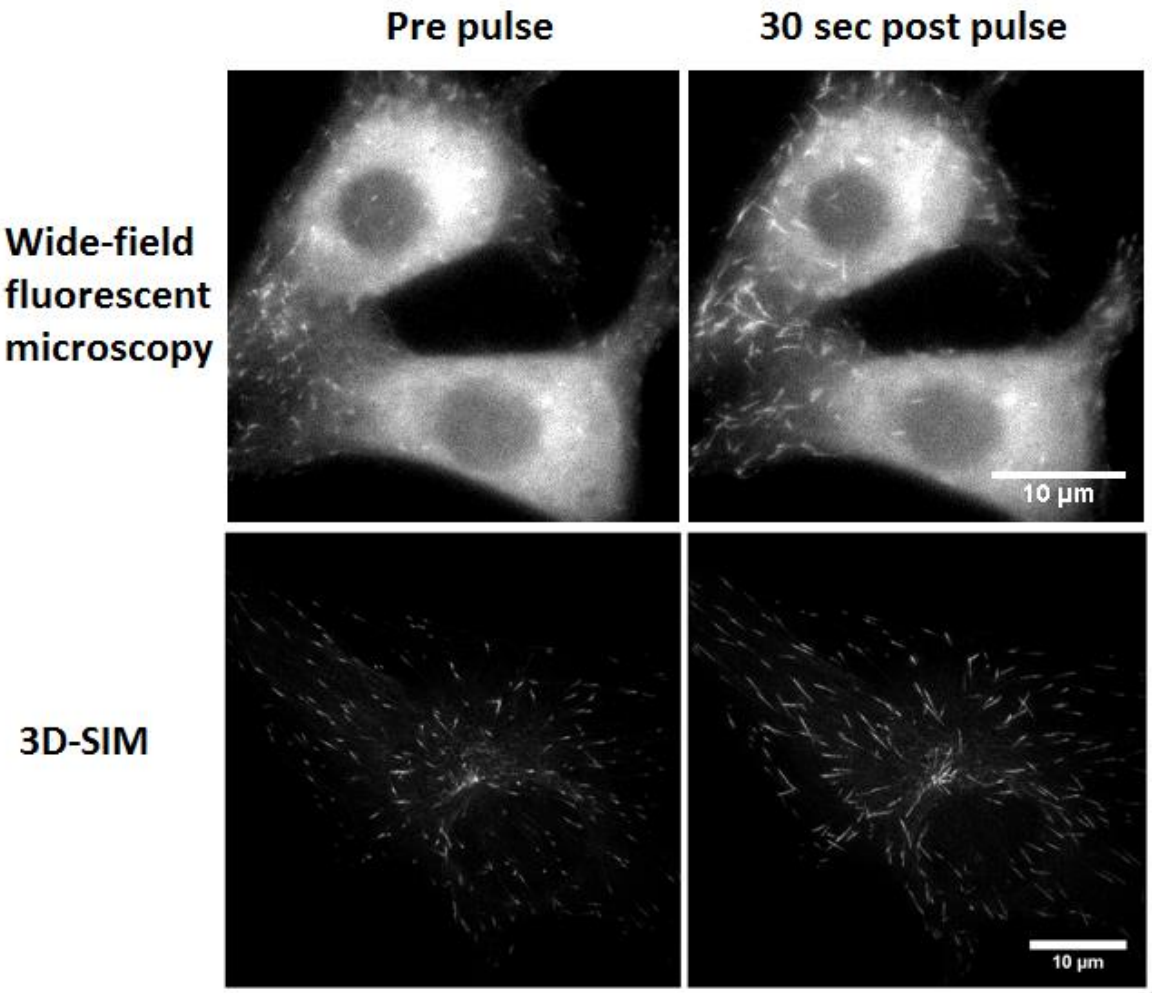

Figure 32. 100 pulses at 10 Hz causes an increase in EB3 comet size.

EB3 comets pre-pulse (left) and 30 seconds post-pulse application (right) captured with wide-field fluorescent microscopy (EB3-GFP) (top) or 3D-SIM microscopy (EB3-mNeonGreen) (bottom).

3.3.5. Is increased intracellular calcium responsible for disruption of the microtubule network?

Given that nsPEF causes a rapid increase in intracellular calcium concentration and that calcium ions are known to destabilise microtubules, we next investigated the possibility that the microtubule network disruption was calcium induced. U87 cells were loaded with Fura Red, AM and imaged every 3 seconds for a total of 174 seconds (59 image captures). 100, 10 ns pulses at 10 Hz were applied after 24 seconds (9 image captures). Changes in fluorescence for these experiments were plotted on the graph obtained in Figure 31 that showed changes in EB3-mNeonGreen fluorescence following the same pulse exposure. This allowed for a temporal comparison between increase in intracellular calcium and the onset of microtubule disruption.

A 0.2 fold decrease in Fura Red fluorescence, representing an increase in intracellular Ca^{2+} concentration, was observed in the first 3 seconds following the start of pulse application and a stable fluorescence level was reached by 9 seconds. The timing of this stabilisation corresponds with the end of the pulse application period (Figure 33). Given that the decrease in EB3-mNeonGreen fluorescence, from base-line, is first observed to occur 8 seconds after the start of pulse application, it would seem that the increase in calcium concentration precedes the start of the breakdown of the microtubule network.

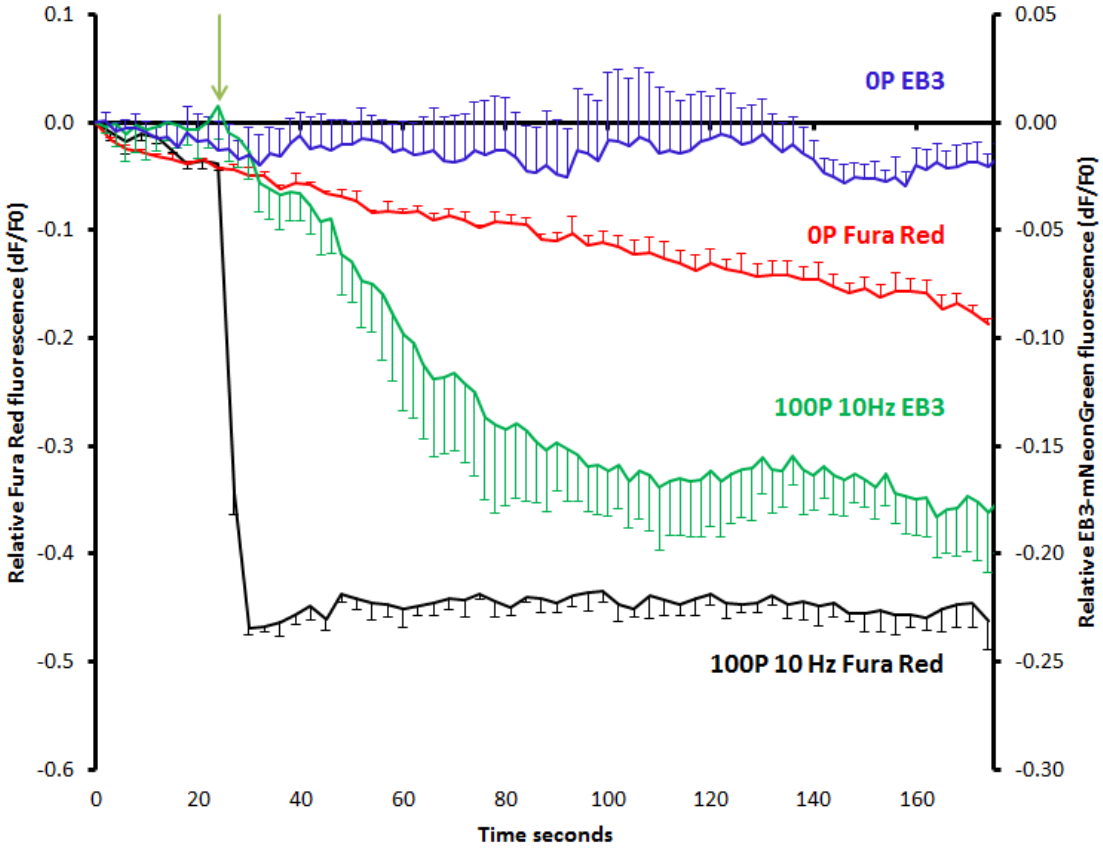

Figure 33. Effect of 100, 10 ns pulses delivered at 10 Hz on the change of fluorescence of EB3-mNeonGreen and Fura Red.

EB3-mNeonGreen (green line, n=4) and the calcium indicator Fura Red (black line, n=3) and their respective controls (EB3-mNeonGreen: blue line, n=4 and Fura Red: red line, n=3) Decrease in Fura Red fluorescence indicates an increase in Ca^{2+} concentration. The start of application of pulse is denoted by the green arrow. Error bars show S.E.

This result made calcium a likely candidate for the disruption of the microtubule network. To test this we next looked at the effect of 100, 10 ns pulses applied at 10 Hz on the microtubule network in calcium free environments. Having already shown that plasma membrane poration occurs with this pulse regime it was likely that extracellular calcium would be a large contributor to the post-pulse increase in intracellular calcium. We therefore pulsed EB3-GFP expressing U87 cells in a calcium-free HBSS containing 4 mM EGTA. As shown in Figure 34 the absence of extracellular calcium failed to have an effect on either the decrease in EB3-GFP fluorescence or the increase of EB3 comet length.

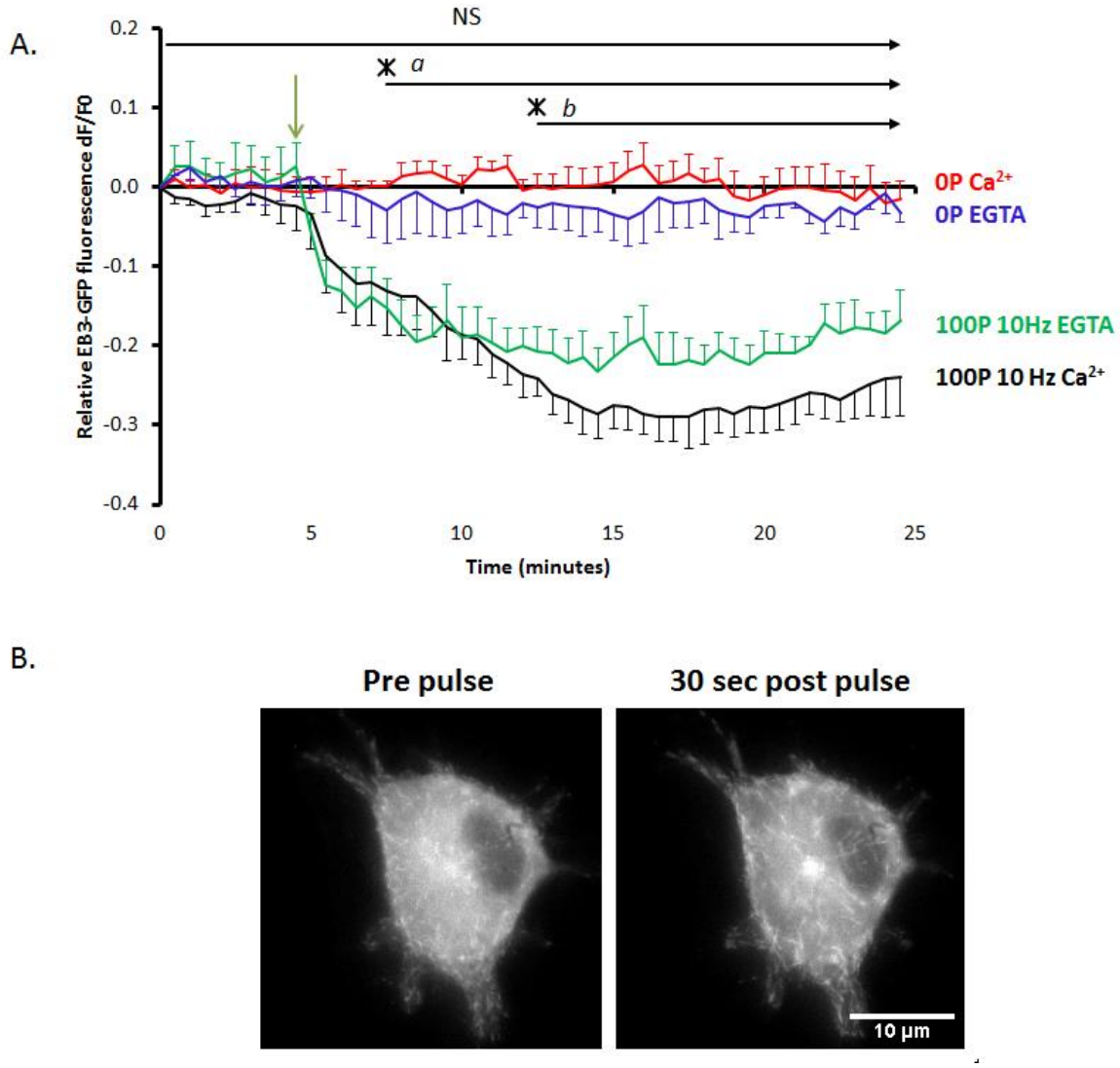

Figure 34. Effect of 100, 10 ns pulses delivered at 10 Hz on EB3-GFP in the absence of extracellular calcium

A: Effect of 100, 10 ns pulses delivered at 10 Hz on the change of fluorescence of EB3-GFP in the presence (black line, n=6) and absence (green line, n=4) of extracellular calcium. Their respective unpulsed controls are shown by the red (n=7) and blue lines (n=3). NS denotes no significant difference between the two pulsed conditions. Asterisk *a* indicates a significant difference between the calcium control and both pulsed experiments, asterisk *b* indicates a significant difference between the EGTA control and the EGTA pulsed experiment, as reported by two-way repeated measures ANOVA with Bonferroni tests, $F(11.82, 63.04) = 13.64$, $p < 0.05$. The start of application of pulse is denoted by the green arrow. Error bars show S.E. B: Representative images showing EB3 comets before and after pulse application in a calcium free buffer.

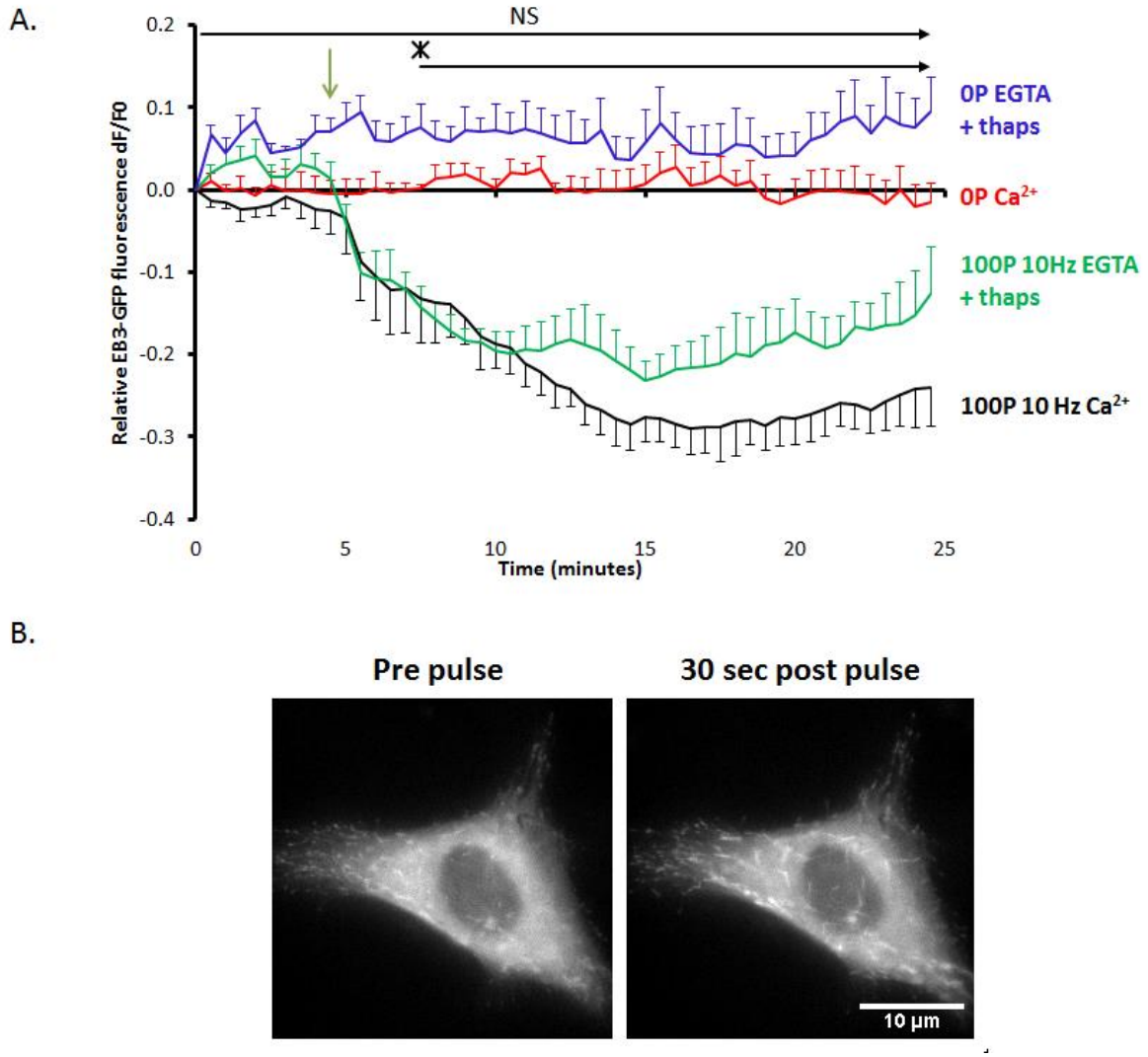

Figure 35. Effect of 100, 10 ns pulses delivered at 10 Hz on EB3-GFP in the absence of extracellular and intracellular calcium.

A: Effect of 100, 10 ns pulses delivered at 10 Hz on the change of fluorescence of EB3-GFP in the presence (black line, n=6) of extracellular calcium and absence of calcium with thapsigargin depleted intracellular calcium stores (green line, n=5). Their respective unpulsed controls are shown by the red (n=7) and blue lines (n=3). NS denotes no significant difference between the two pulsed conditions. The asterisk indicates a significant difference between the control conditions and pulsed conditions, as reported by two-way repeated measures ANOVA with Bonferroni tests, $F(12.19, 69.10) = 13.97$, $p < 0.05$. The start of application of pulse is denoted by the green arrow. Error bars show S.E. B: Representative images showing EB3 comets before and after pulse application in a calcium free buffer with thapsigargin depleted intracellular calcium stores.

Intracellular calcium stores, such as the ER, are also likely to contribute to the post-pulse increase in calcium. To deplete the ER stores U87 EB3-GFP cells were incubated for 30 minutes with 1 µM of thapsigargin before pulsing in the calcium-free HBSS. Again the same initial decrease in EB3-GFP fluorescence was observed (Figure 35), however fluorescence levels started to recover towards the end of the imaging period suggesting a possible downstream action of calcium. The increase in EB3 comet length was also observed under the calcium depleted conditions. The absence of a post-pulse increase in calcium under the calcium depleted conditions was confirmed by the FLUO-4 results in the previous chapter, reproduced here in Figure 36.

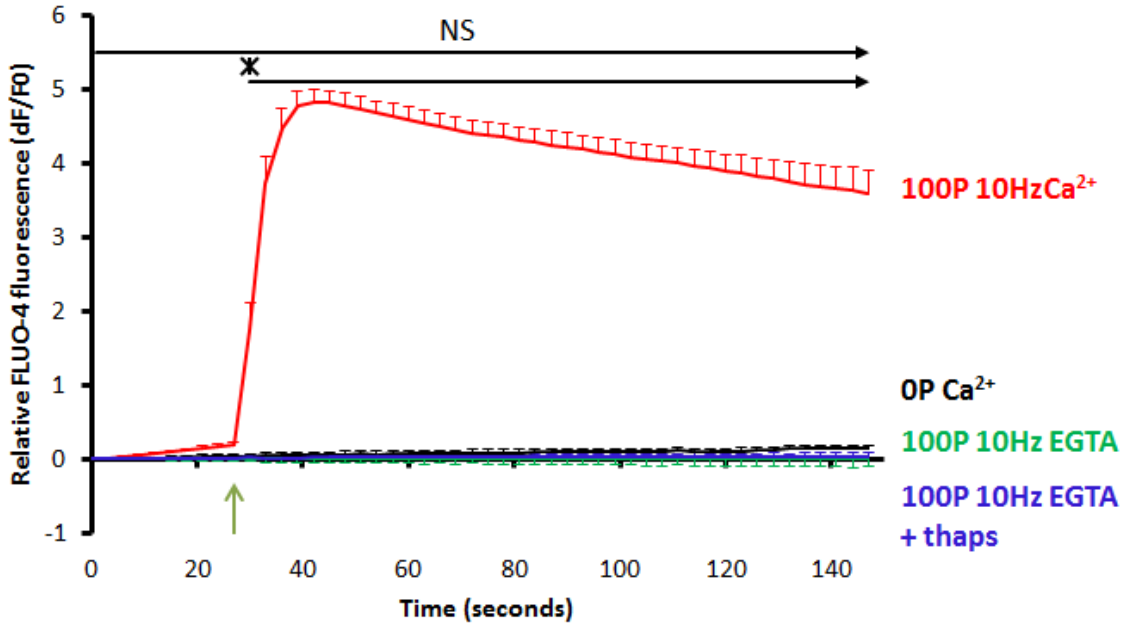

Figure 36. Effect of 100, 10 ns pulses delivered at 10 Hz on the change of FLUO-4 fluorescence in U87 cells under calcium free condition.

Change in FLUO-4 fluorescence in U87 cells subjected to 100 pulses delivered at 10 Hz. Black = non-pulsed controls (n=4), red = pulsed Ca^{2+} HBSS (n=8), green = pulsed Ca^{2+} free HBSS (n=3) and blue = pulsed Ca^{2+} free HBSS with thapsigargin treatment (n=3). NS denotes no significant difference between the unpulsed and both calcium-free pulsed conditions. The asterisk indicates a significant difference between Ca^{2+} HBSS pulsed condition and the unpulsed control and both calcium free conditions, as reported by two-way repeated measures ANOVA with Bonferroni tests, $F(5.39, 25.15) = 97.97$, $p < 0.05$. The start of application of pulse is denoted by the green arrow. Error bars show S.E.

3.3.6. Is cellular swelling responsible for disruption of the microtubule network?

By imaging YO-PRO-1 entry we have previously shown cell poration following the application of 100 pulses at 10 Hz. Osmotic swelling as a result of this poration is therefore likely to occur and rapid swelling could be an explanation for the observed breakdown of the microtubule network.

To test if swelling caused the microtubule breakdown we applied pulses to cells in calcium containing HBSS mixed 7:3 with a 300 mM sucrose solution, which has previously been shown to prevent nsPEF induced swelling[169]. A post-pulse decrease in EB3 fluorescence, initially closely resembling that observed with Ca^{2+} HBSS, was obtained (Figure 37a). However, unlike the cells pulsed only in the calcium containing HBSS, those in the sucrose solution show EB3 fluorescence levels starting to recover within 5 minutes of pulse application. The previously observed increase in EB3 comet size was also seen in sucrose pulsed cells (Figure 37b).

Sucrose does however affect the conductivity of the HBSS solution and can alter the intensity of the nsPEF effect on the cell[170]. To further understand post-nsPEF swelling in U87 cells we used phase contrast microscopy to observe cell morphology before and after nsPEF application (Figure 38). We observed no morphological indications of swelling with an absence of blebbing in all cases. We also measured cell area and found an absence of swelling. Cells had a pre-pulse cell area of 202.1 ± 13.4 μm² (n = 12). When compared to the pre-pulse cell area nsPEF treated cells showed a 3.5 ± 1.4 % decrease in area at 30 seconds post nsPEF, a 6.6 ± 3.5 % decrease at 180 seconds post nsPEF and a 8.1 ± 5.4 % decrease 10 minutes post pulse (n = 6). Non-nsPEF treated cells at the same time points showed a 2.0 ± 2.7 % decrease for 30 seconds post, a 3.7 ± 1.7 % decrease for 180 seconds post and a 3.6 ± 3.6 % increase at 10 minutes post (n = 6). Using a two tailed independent samples t-test, there was no significant difference in cell area change between cells in the control condition (X = 3.55, SE = 3.59) and cells in the nsPEF condition at the 10 minute time point (X = -8.07, SE = 5.43) $t(9) = -1.78$, $p = 0.11$.

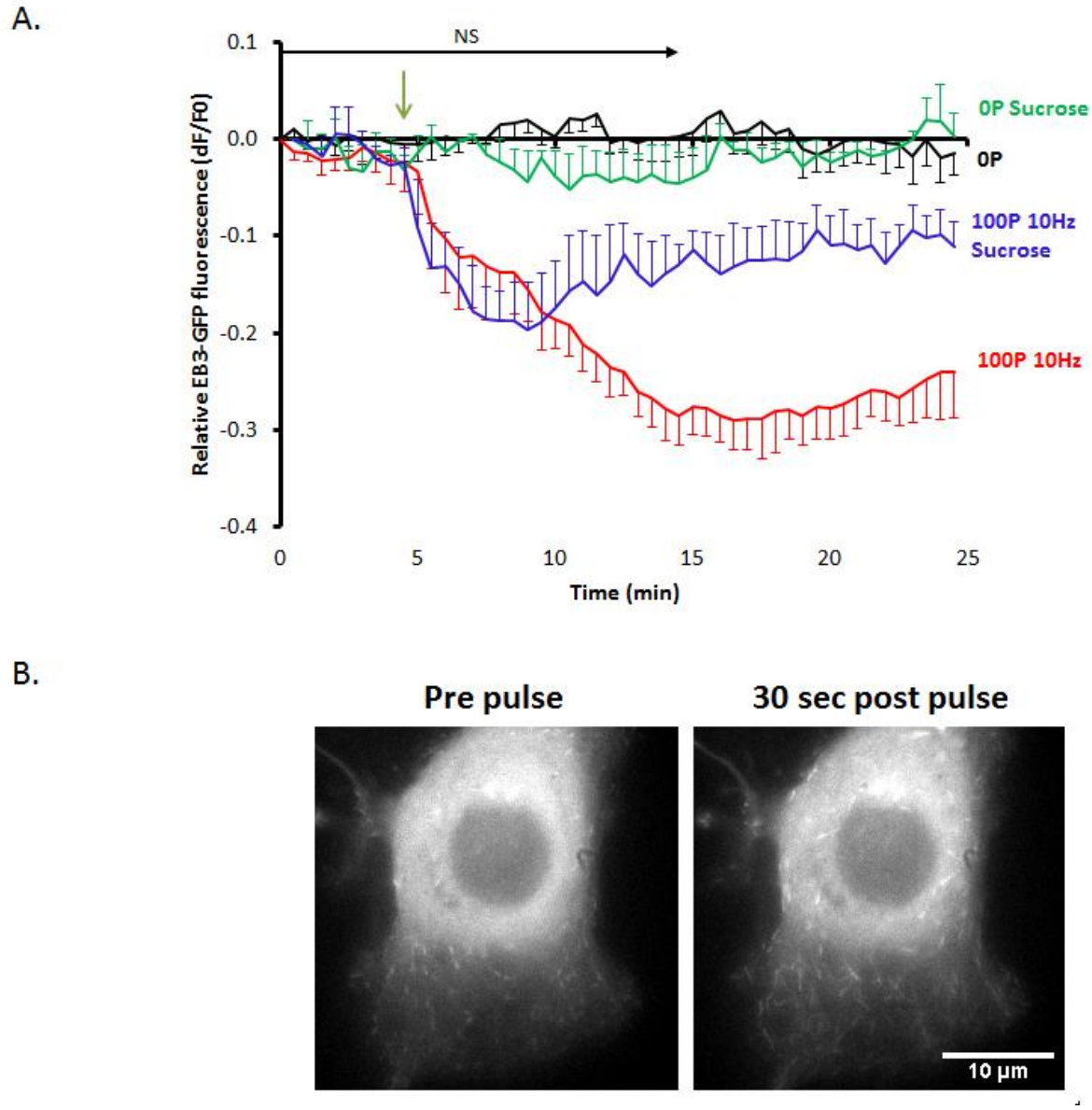

Figure 37. Cellular swelling does not cause nsPEF induced changes to microtubule growth.

A.100, 10 ns pulses delivered at a frequency of 10 Hz were applied to U87-EB3-GFP glioblastoma cells bathed in Ca^{2+} HBSS (red line, n=6) or a 7:3 mix of Ca^{2+} HBSS and 300 mM sucrose (blue line, n=3) and their corresponding unpulsed controls (black line, n=7 and green line, n=3, respectively). NS denotes no significant difference between the two pulsed conditions, as reported by two-way repeated measures ANOVA with Bonferroni tests, $F(11.55, 53.90) = 12.12$, $p > 0.05$. The green arrow denotes the start of pulse application and error bars show S.E. B. EB3 comets before pulse, left, and 30 seconds post pulse, right in the sucrose containing HBSS.

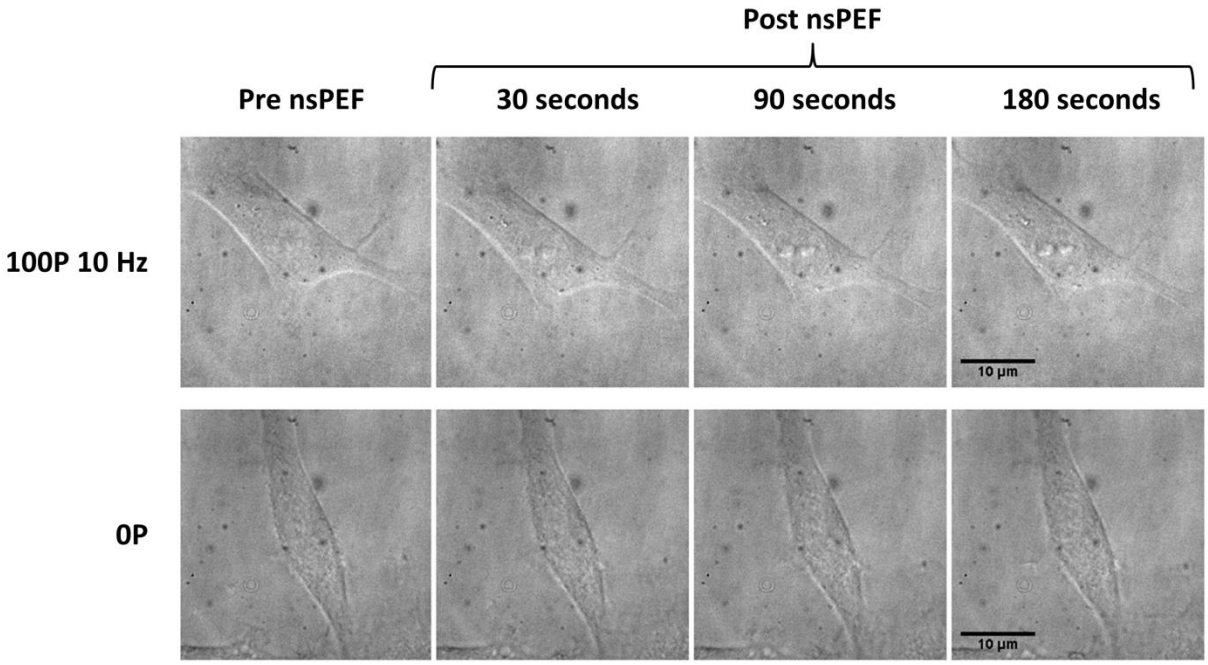

Figure 38. U87 cells do not swell following the application of 100, 10 ns pulses at 10 Hz. Representative phase contrast images of U87 cells before and following the application of 100, 10 ns pulses delivered at a frequency of 10 Hz (top) or non-nsPEF treated controls taken at the same time points (bottom).

3.3.7. Evidence of a direct effect of nsPEF on microtubules

As neither of the obvious explanations for microtubule disruption, calcium ions and swelling, appear to be responsible we next looked at the possibility that nsPEF was exerting a direct effect on microtubules.

Microtubules exist in a complex environment within the cell where they interact with, and can be stabilised or destabilised by, many different proteins and ions. To limit the impact of these factors we looked at taxol-stabilised microtubules, polymerised *in vitro* from rhodamine-labelled, purified tubulin. We exposed them to nsPEF using a custom delivery system (Figure 39). Care had to be taken when imaging these microtubules as exposure to too much light resulted in their spontaneous depolymerisation. Pulsing these microtubules however failed to have an effect on them (Figure 40).

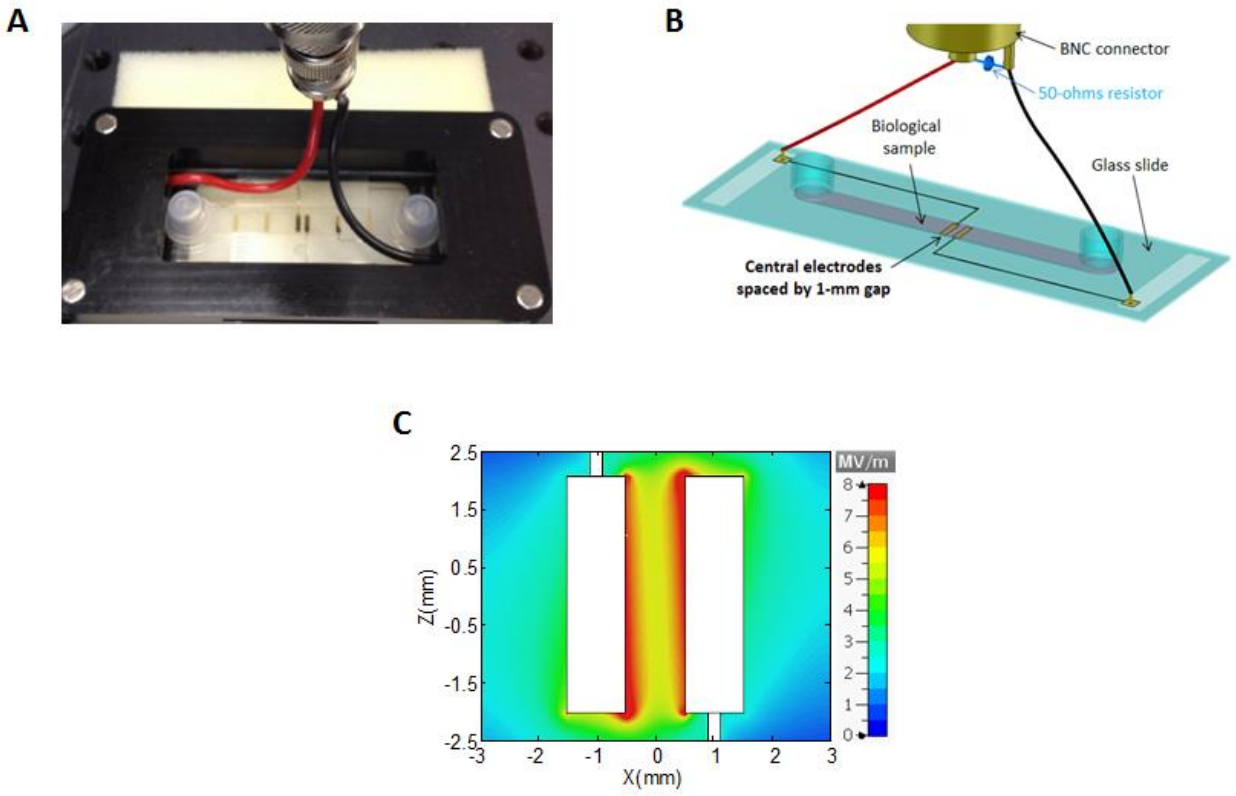

Figure 39. The delivery system used to apply nsPEF to purified microtubules.

A: photo and B: a diagram of the delivery system that comprised of a glass slide with built in electrodes and a central reservoir that held the microtubule solution. This was placed in a holder and the electrodes were connected to a coaxial cable via a connector. An area in the 1 mm gap between the two central electrodes was visualised with the microscope. C: the electric field distribution between the electrodes at the maximum electric field magnitude. Images used with permission from Malak Soueid, XLIM.

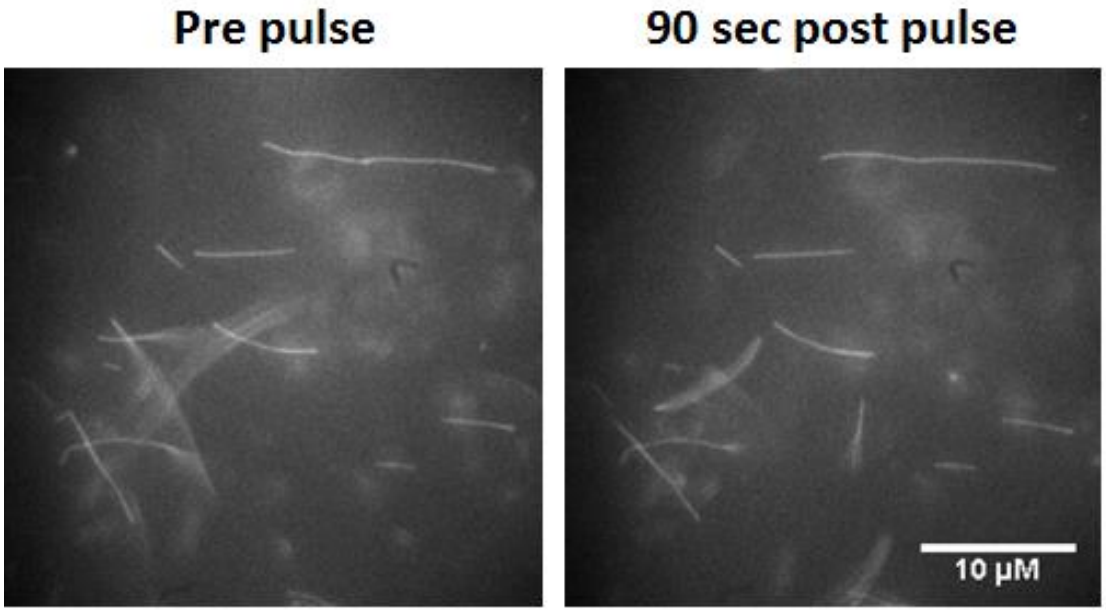

Figure 40. nsPEF show no effect on taxol stabilised, purified microtubules.
100, 10 ns pulses were applied at 10 Hz to purified rhodamine labelled microtubules in a µ-slide.

Given the lack of response in the purified microtubules we looked in more detail at microtubules in their cellular environment. U87 cells expressing tubulin-RFP were imaged by wide-field microscopy and exposed to our 100 pulse, 10 Hz pulse regime. Whilst the lack of resolution made it impossible to visualise individual microtubules we were able to see microtubule bundles. These bundles were most identifiable in flatter areas of the cell, such as the prolongations, where the density of microtubules is lower. Following pulse application we saw wave-like buckling occurring in some of these microtubule bundles (Figure 41a). To see if this buckling also occurred in individual microtubules we used the higher resolution offered by 3D-SIM. U87 cells expressing tubulin m-Emerald, which proved more photostable in 3D-SIM imaging than tubulin-RFP, were subjected to our pulse regime. We found, in the few minutes following pulse application, evidence that individual microtubules can bend and buckle and that this results in the depolymerisation of the microtubule (Figure 41b).

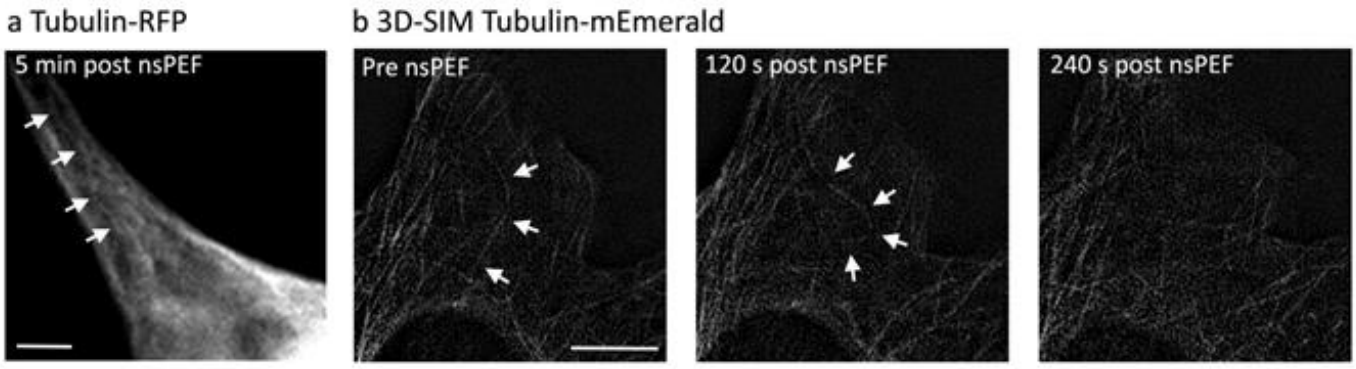

Figure 41. nsPEF application can cause microtubule buckling and depolymerisation.

a: A U87 tubulin-RFP cell showing post-pulse microtubule buckling as indicated by the white arrow. Scale bar = 5 µm b: A U87 tubulin-mEmerald cell, imaged using 3D-SIM, showing how individual microtubules can buckle following the pulse (120 s post pulse image) resulting in loss of the microtubule by depolymerisation (240 s post pulse image). Scale bar = 5 µm.

3.3.8. Link between disruption of the microtubule network and loss of mitochondrial membrane potential

Having demonstrated that nsPEF causes disruption of the microtubule network we next wanted to look at its possible downstream effects. Chemically induced microtubule depolymerisation has previously been shown to cause loss of $\Delta\Psi_m$[135]. As nsPEF treatment is also known to cause loss of $\Delta\Psi_m$ we looked next for a temporal link between post-pulse breakdown of the microtubule network and $\Delta\Psi_m$ dissipation. Using U87 cells loaded with TMRM we have already shown that our 100 pulse, 10 Hz pulse regime caused loss of $\Delta\Psi_m$ (Figure 21).When compared to the fluorescence-time plot of EB3-GFP (Figure 42) we found that the loss of $\Delta\Psi_m$ closely followed the disruption of microtubule dynamics.

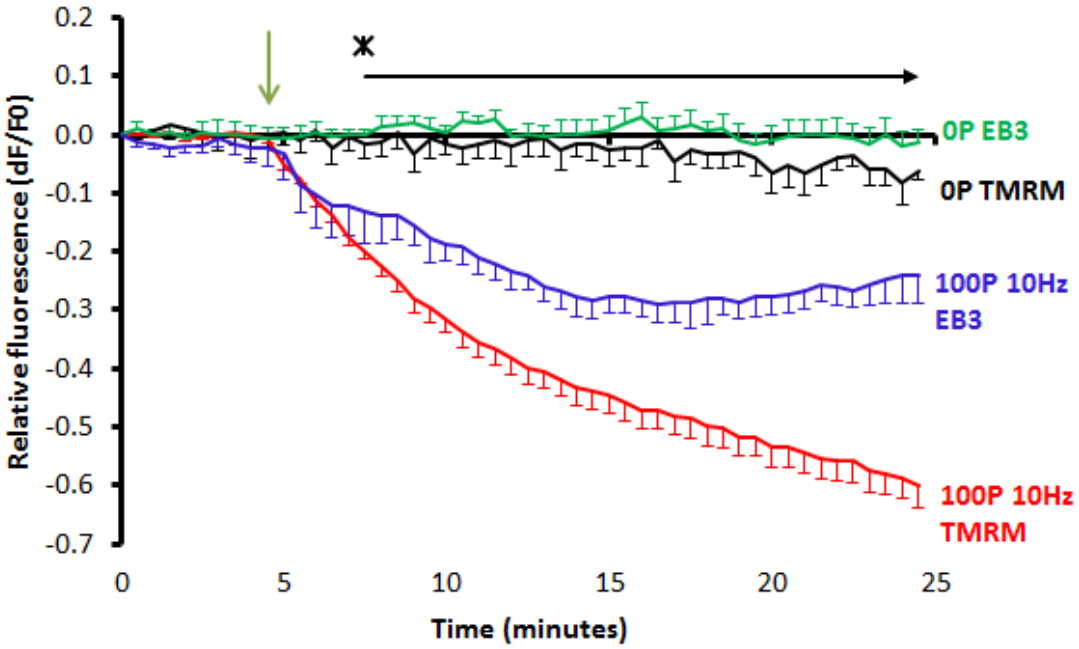

Figure 42. Loss of $\Delta\Psi_m$ is temporally linked to microtubule disruption.

100, 10 ns pulses delivered at a frequency of 10 Hz were applied to either U87-EB3-GFP cells (blue line, n = 6) or U87 cells loaded with TMRM (red line, n = 7) with corresponding non-pulsed controls (green line, n = 7 and black line, n = 3, respectively). Asterisk indicates a significant difference between pulsed and control TMRM experiments, when analysed by two way repeated measures ANOVA with Bonferroni tests $F(1.36, 10.85) = 79.52$, $p < 0.05$. The green arrow indicates the start of pulse application and error bars show S.E.

3.3.9. Does the breakdown of the microtubule network cause the mPTP to open?

Loss of $\Delta\Psi_m$ due to chemical depolymerisation of microtubules has been shown to be due to opening of the mPTP[135]. We therefore investigated the role that mPTP opening may play in the post-pulse loss of mitochondrial membrane potential. One effect of mPTP opening is the formation of donut-shaped mitochondria[171]. We used 3D-SIM to visualise mEmerald labelled mitochondria in U87 cells before and post application of 100 pulses applied at 10 Hz. We found the presence of a small number of mitochondrial donuts before the pulse application (Figure 43). These donuts remained at 120 seconds post pulse but no new ones were observed. Whilst this suggests that mPTP opening is not involved, it is possible that their opening and the donut formation takes longer than the two minute period we observed. Longer monitoring with the 3D-SIM was complicated by photobleaching of the mEmerald. Opening of the mPTP

is triggered by increased calcium concentrations[172] and catalysed by the binding of cyclophilin-D[173]. However, we were unable to prevent the loss of $\Delta\Psi_m$ by pulsing cells in Ca^{2+} free HBSS or cells that were pre-treated with 10 µM cyclosporin A, which binds to, and inhibits the action of cyclopholin-D (Figure 44).

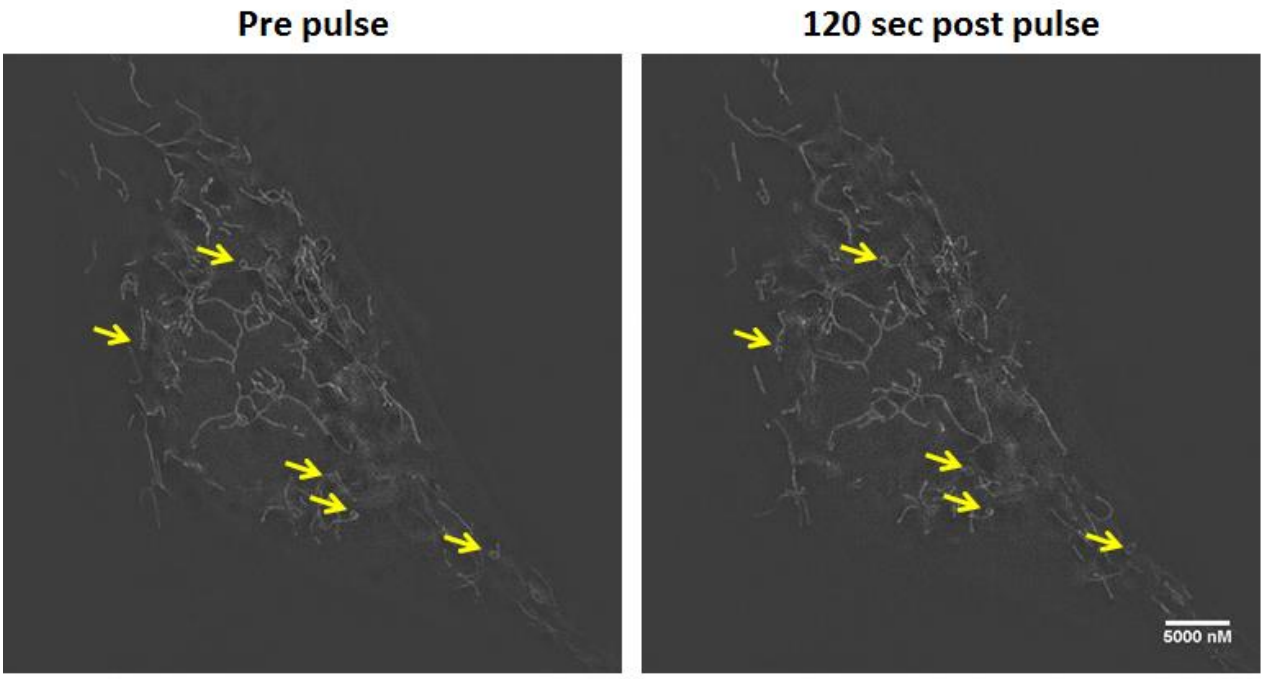

Figure 43. Small numbers of mitochondrial donuts are present in the cell before and after pulse.

mEmerald labelled mitochondria in U87 cells before and 120 seconds post application of 100 pulses applied at 10 Hz, visualised by 3D-SIM. Examples of mitochondrial donuts are labelled with the yellow arrows.

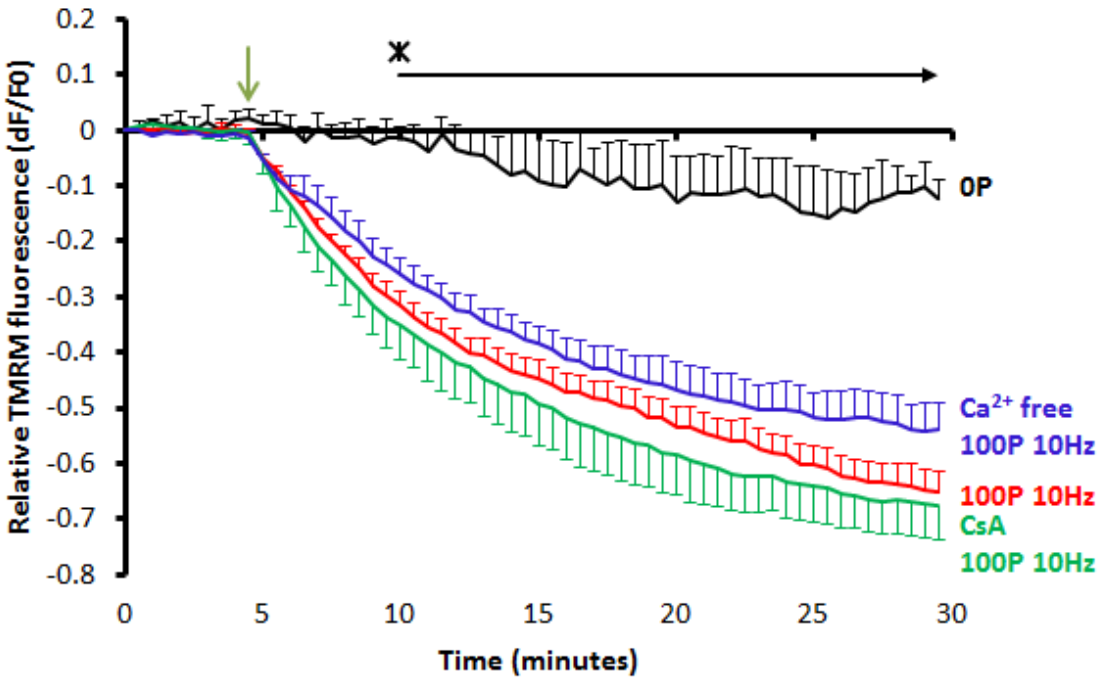

Figure 44. Loss of $\Delta\Psi_m$ is not caused by mPTP opening.

100, 10 ns pulses delivered at a frequency of 10 Hz applied to U87 cells loaded with TMRM in either Ca^{2+} HBSS (red line, n = 7), in Ca^{2+} free HBSS (blue line, n = 4) or Ca^{2+} HBSS with a pre-treatment in 10 µM cyclosporin A (CsA) (green line, n = 4) and the non-pulsed control (black line, n = 3). Asterisk indicates a significant difference between pulsed conditions and control and no significant difference between the different pulsed conditions, two way repeated measures ANOVA with Bonferroni test $f(4.23, 18.35) = 11.49$, $p < 0.05$. The green arrow indicates the start of pulse application and error bars show S.E.

3.3.10. Effect of microtubule chemical disruptors and stabilisers on EB3 dynamics

To further assess the downstream effects of nsPEF microtubule disruption we looked at how nsPEF affected cells with either chemically depolymerised or stabilised microtubules. To determine an effective dose and incubation time EB3-GFP expressing U87 cells were imaged before and following application of 10 µM colchicine or 10 µM taxol, to respectively disrupt or stabilise microtubules (Figure 45). We found that for both conditions by 2.5 minutes following drug addition, EB3 comet size had reduced. By 7.5 minutes there were no visible EB3 comets in either of the conditions. By 25 minutes the colchicine cells show a modified morphology with signs of detachment and cell rounding. Conversely the taxol treated cells maintain their morphology at 25 minutes.

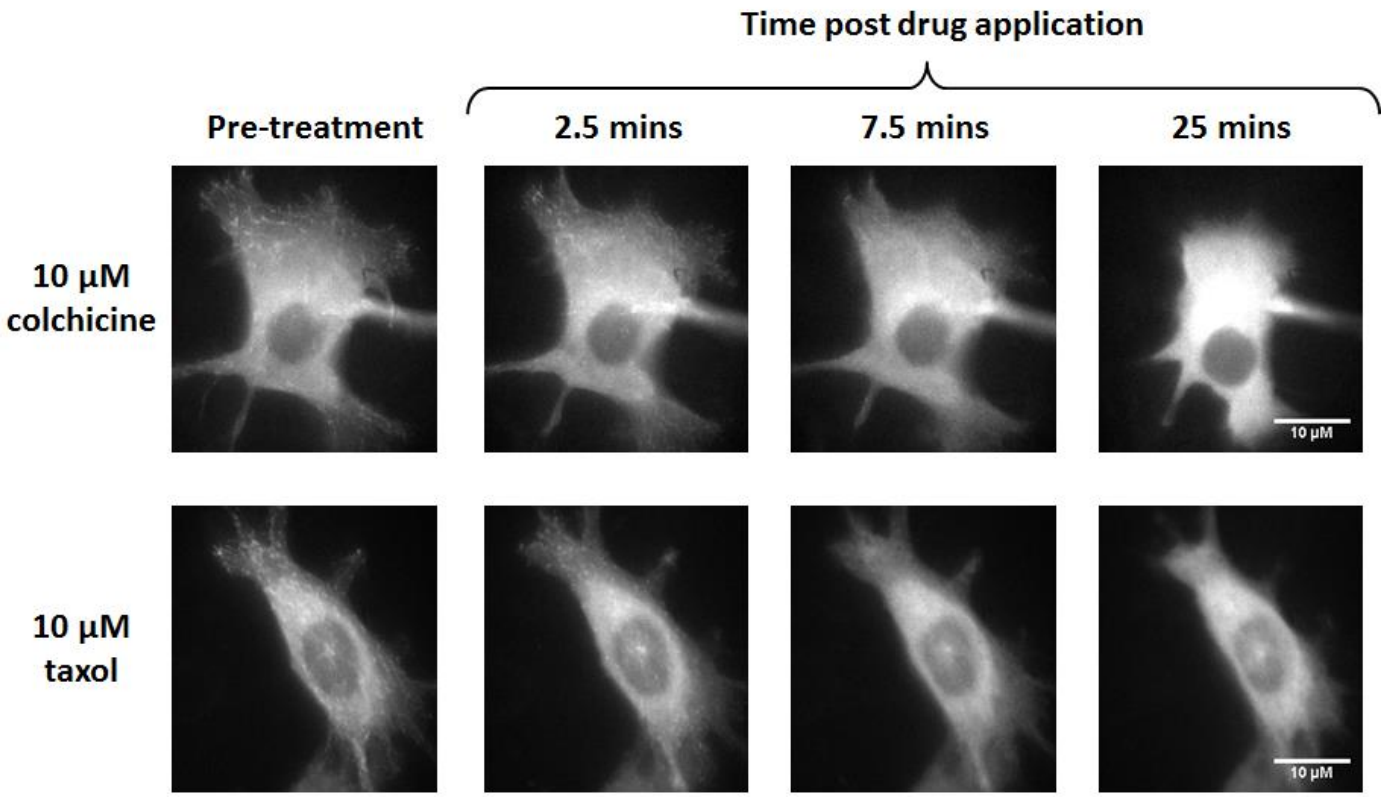

Figure 45. Effects of taxol and colchicine on microtubule growth dynamics in U87 cells expressing EB3-GFP.

Representative images of the effect of 10 µM colchicine or 10 µM taxol on microtubule growth dynamics as visualised with EB3-GFP.

3.3.11. Does breakdown of the microtubule network cause plasma membrane poration?

As microtubules form many interactions with the cell membrane we next looked at the possibility that their nsPEF induced disruption could result in the membrane poration that we have previously observed post-pulse (Figure 11). To do this we looked at post-pulse YO-PRO-1 uptake into U87 cells that had been treated with either taxol or colchicine. We found that applying 100 pulses at 10 Hz to cells with chemically stabilised microtubules did not alter the uptake of YO-PRO-1 when compared to non-taxol treated pulsed cells (Figure 46). Similarly, when cells with chemically depolymerised microtubules were pulsed there was no difference in YO-PRO-1 uptake when compared to non-colchicine treated pulsed cells (Figure 47).

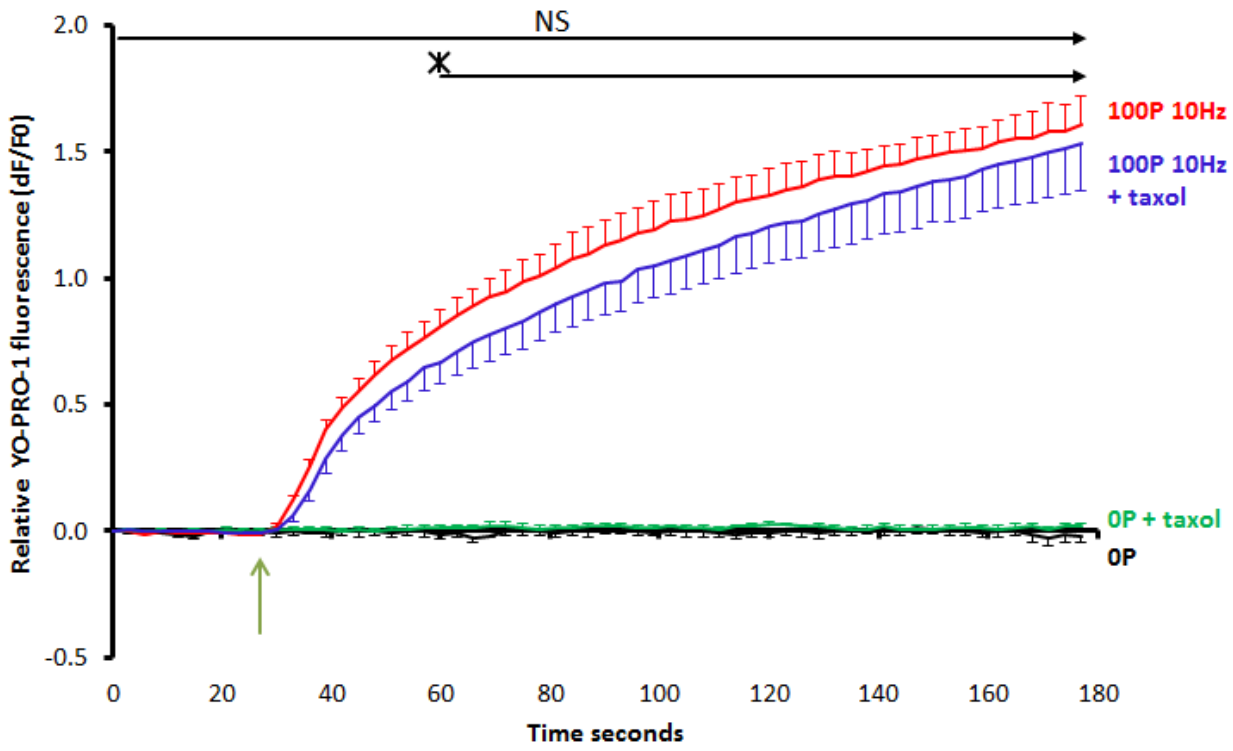

Figure 46. Microtubule stabilisation does not alter YO-PRO-1 uptake.

YO-PRO-1 uptake following application of 100, 10 ns pulses delivered at a frequency of 10 Hz to U87 cells that were either treated with 10 µM taxol (blue line, n=7) or not (red line, n=3) with corresponding non-pulsed controls (green line, n = 6 and black line, n = 6, respectively). NS denotes no significant difference between the two pulsed conditions. Asterisk indicates a significant difference between pulsed and control experiments, as analysed by two way repeated measures ANOVA with Bonferroni tests, $F(3.13, 18.77) = 24.17$, $p < 0.05$. The green arrow indicates the start of pulse application and error bars show S.E.

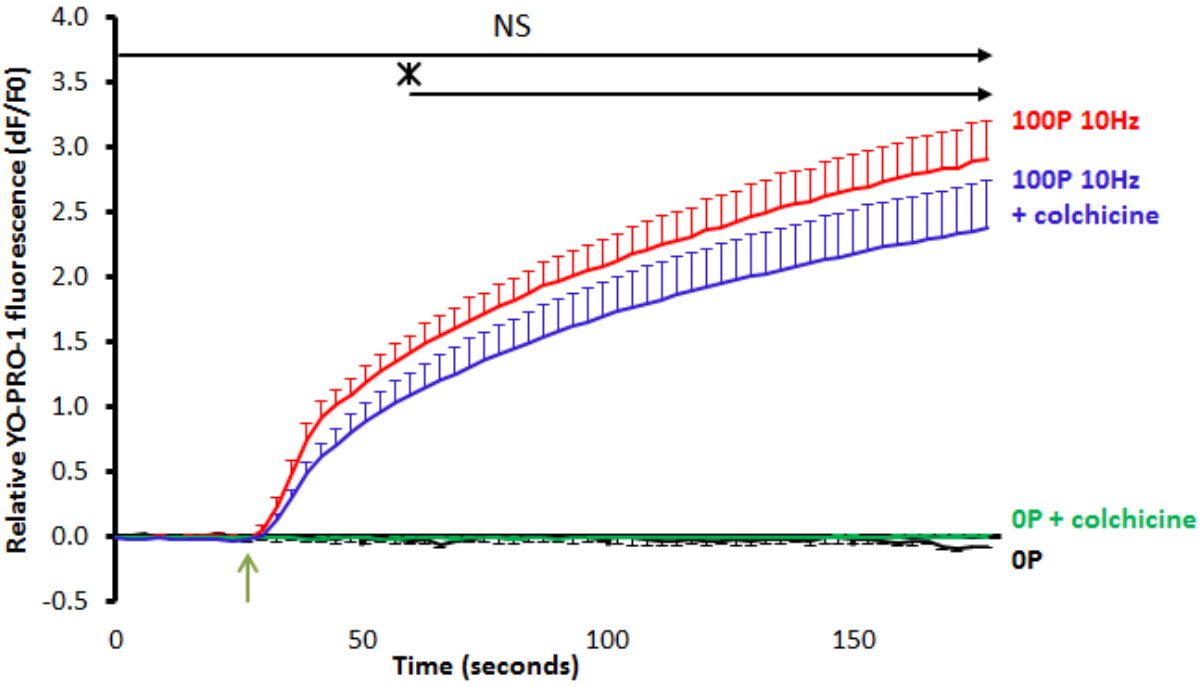

Figure 47. Chemical microtubule disruption does not alter YO-PRO-1 uptake.

YO-PRO-1 uptake following application of 100, 10 ns pulses delivered at a frequency of 10 Hz to U87 cells that were either treated with 10 µM colchicine (blue line, n=6) or not (red line, n=4) with corresponding non-pulsed controls (green line, n = 3 and black line, n = 3, respectively). NS denotes no significant difference between the two pulsed conditions. Asterisk indicates a significant difference between pulsed and control experiments, two way repeated measures ANOVA with Bonferroni tests, $F(3.15, 12.61) = 20.37$, $p < 0.05$. The green arrow indicates the start of pulse application and error bars show S.E.

3.3.12. Does nsPEF induced breakdown of the microtubule network cause an increase in intracellular calcium concentration?

We next looked at whether chemical microtubule stabilisation or depolymerisation would affect the post-pulse calcium response. We applied 100 pulses at 10 Hz to U87 cells loaded with Fura Red and treated with either taxol (Figure 48) or colchicine (Figure 49). Under both chemical treated conditions the post-pulse intracellular calcium increase matched that of non-chemically treated pulsed cells.

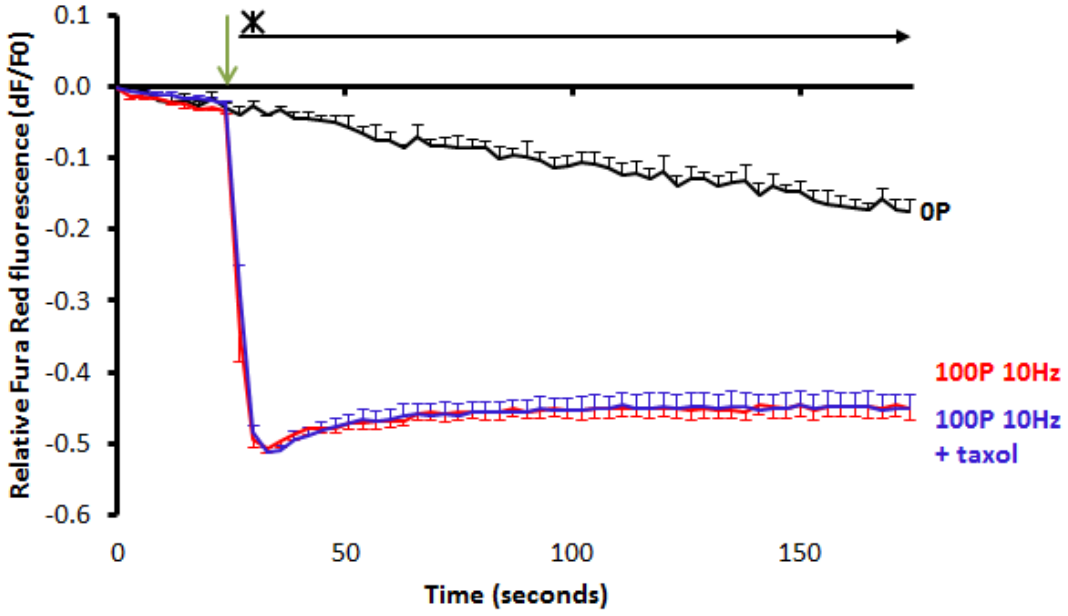

Figure 48. Microtubule stabilisation does not alter the post-pulse increase in intracellular calcium.

Intracellular changes in calcium measured in U87 cells loaded with Fura Red following application of 100, 10 ns pulses delivered at a frequency of 10 Hz. Cells were either treated with 10 µM taxol (blue line, n=6) or not (red line, n=6) with a non-pulsed control (black line, n = 3,). The asterisk indicates a significant difference between pulsed and control experiments and no significant difference between the two pulsed conditions, two way repeated measures ANOVA with Bonferroni tests $F(2.82, 6.94) = 66.26$, $p < 0.05$. The green arrow indicates the start of pulse application and error bars show S.E. A drop in Fura Red fluorescence indicates an increase in intracellular calcium.

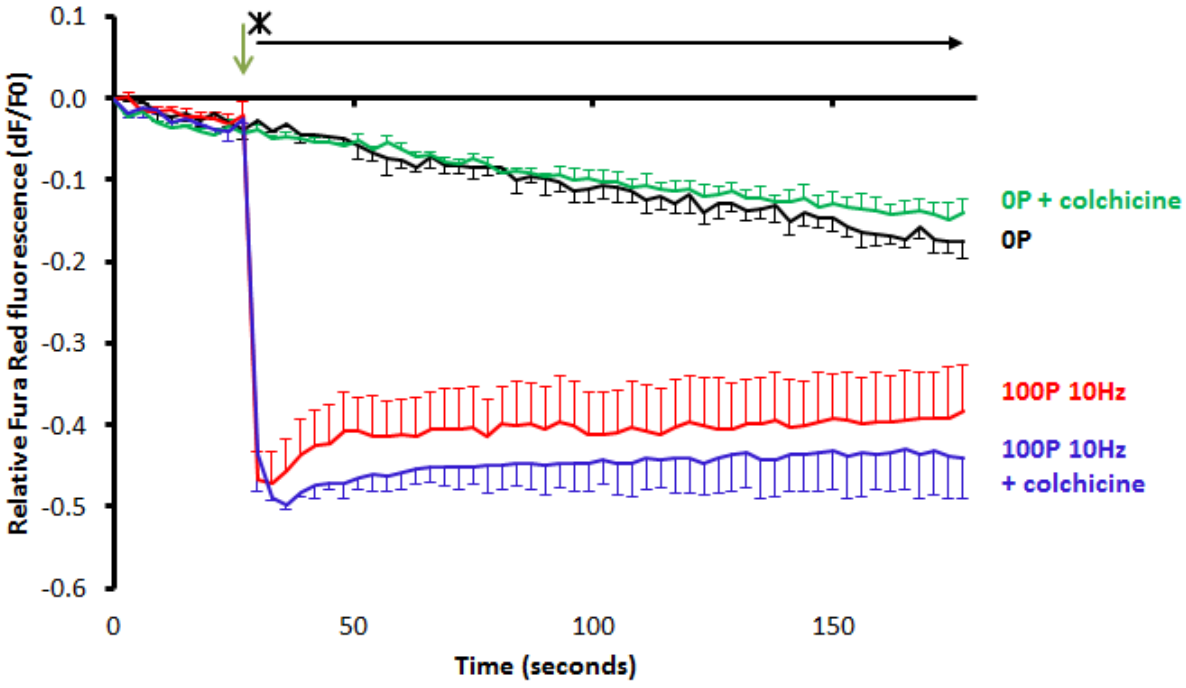

Figure 49. Chemical microtubule disruption does not alter the post-pulse increase in intracellular calcium.

Intracellular changes in calcium measured in U87 cells loaded with Fura Red following application of 100, 10 ns pulses delivered at a frequency of 10 Hz. Cells were either treated with 10 µM colchicine (blue line, n=3) or not (red line, n=3) with corresponding non-pulsed controls (green line, n = 4 and black line, n = 3, respectively). The asterisk indicates a significant difference between pulsed and control experiments and no significant difference between the two pulsed conditions. Two way repeated measures ANOVA with Bonferroni test f (3.68, 11.05) = 30.54, $p < 0.05$. The green arrow indicates the start of pulse application and error bars show S.E. A drop in Fura Red fluorescence indicates an increase in intracellular calcium.

3.3.13. Increasing pulse number results in a calcium-dependant nuclear uptake of EB3

Having only looked at a maximum of 100 pulses we next looked at the effect of 500 or 1000 pulses applied at 10 Hz to cells expressing EB3-mNeonGreen. When 500 pulses were applied an increase in EB3 comet length was visible 15 seconds after the start of pulse application. By 65 seconds EB3 comets had shrunk to less than their pre-pulse length and remained like this throughout the rest of the imaging period (Figure 50a). By 300 seconds post-pulse the MTOC was no longer visible. Microtubule nucleation by the MTOC appeared also to be reduced or absent as EB3 comets showed more random movement within the cell than the organised, pre-

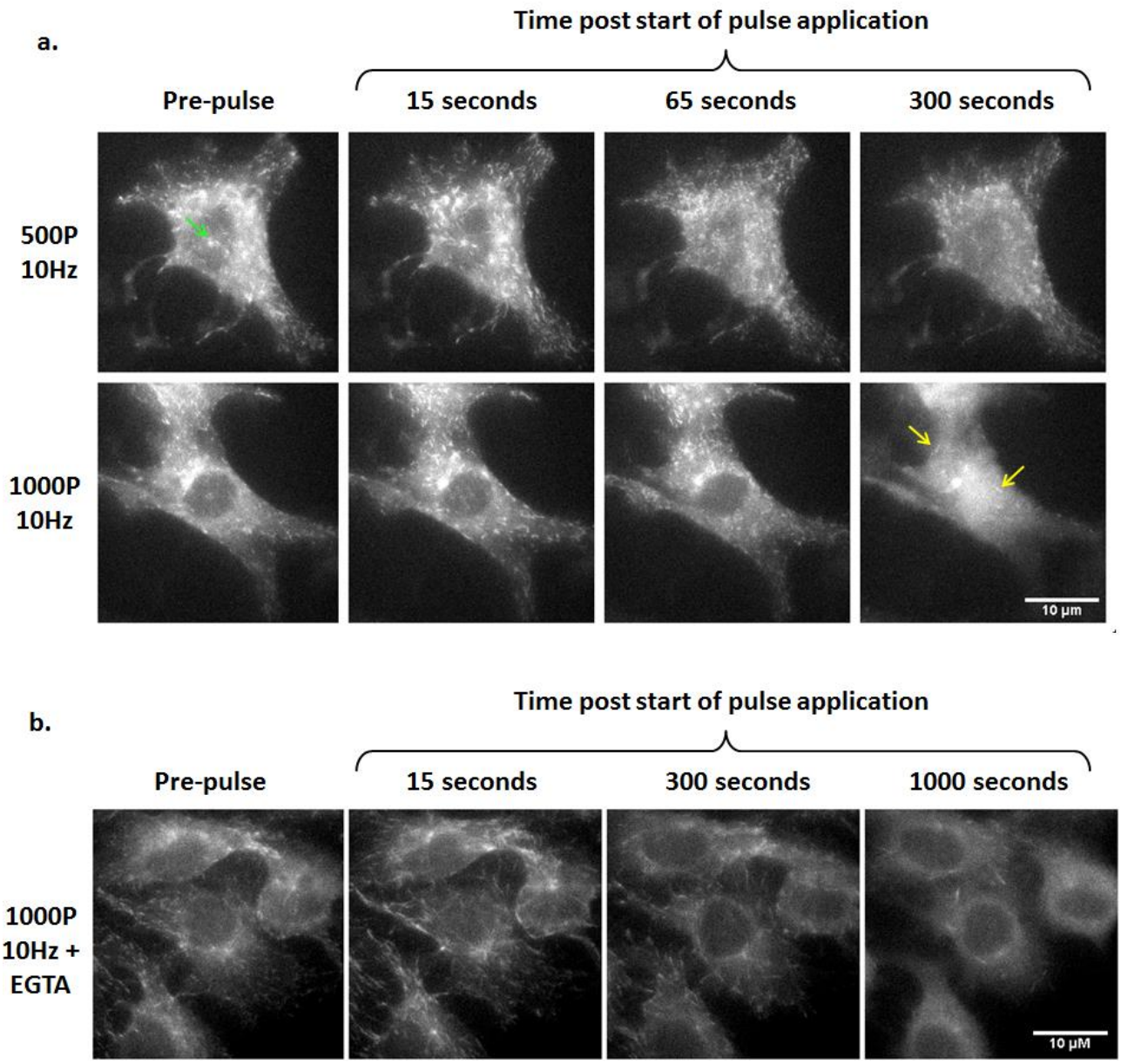

Figure 50. Effects of higher pulse numbers on microtubule dynamics in U87 cells expressing EB3-mNeonGreen.

Representative images of the effect of 500 or 1000 pulses applied at 10 Hz on microtubule growth dynamics as visualised with EB3-mNeonGreen, in the presence (a) or absence (b) of extracellular calcium. The red arrow denotes the MTOC and the yellow arrows denote immobile EB3 comets.

pulse MTOC to plasma membrane movement. Applying 1000 pulses resulted in the same initial increase in EB3 comet length and subsequent shortening, however, by the end of the

pulse application period (100 seconds) the EB3 comets had stopped moving and gradually disappeared with the exception of several immobile comets. By 600 seconds post pulse these immobile comets were still visible. The disappearance of the EB3 comets coincided with a nuclear uptake of EB3, visible in the image taken at 300 seconds post-pulse.

The same 1000 pulses were then applied to cells that were bathed in a calcium free buffer, containing 4 mM EGTA. EB3 comet lengthening was again observed immediately after the start of pulse application. In contrast to when calcium is present, the increased comet length persisted, as can be seen in Figure 50b at 300 seconds. Over the imaging period the number of comets in the cell decreased. By 1000 seconds of the start of pulse application only a few comets persisted and these comets showed both elongation and dynamic movement. No uptake into the nucleus of EB3 was observed.

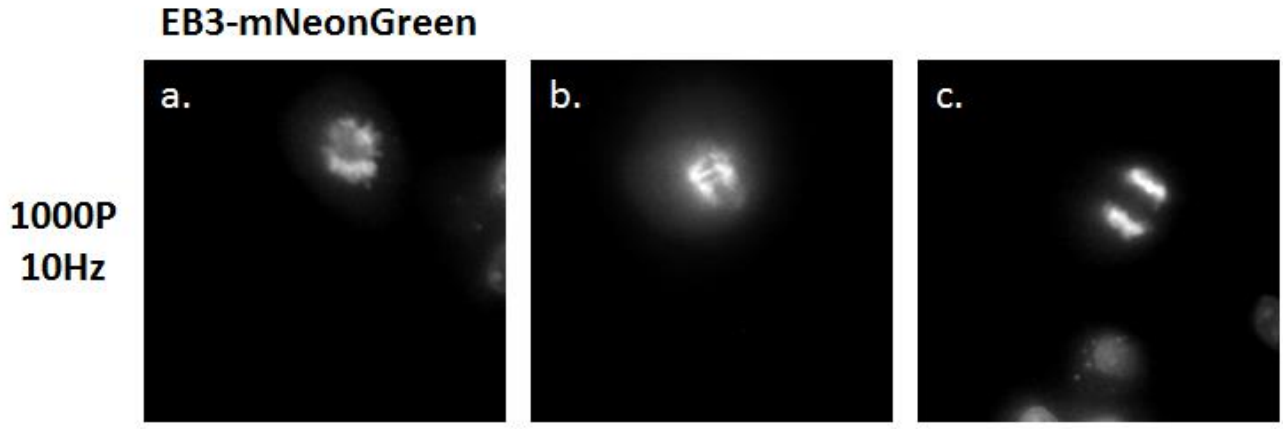

Figure 51. 1000P applied at 10 Hz pushes cells into mitosis.
Representative images of U87- EB3-mNeonGreen cells, 1 hour after pulse application and located proximally to the electrodes. Different stages of mitosis were observed: a) prophase, b) metaphase, c) anaphase.

An hour following the 1000 pulse application the slide was examined in further detail. In addition to the cells located between the electrodes, cells located in proximity to them were found to also found to have nuclear uptake of EB3. Cells located further from the electrodes however appeared to be unaffected by the pulse and showed normal EB3 comet movement. Nuclear uptake of tubulin, and therefore EB3, occurs before cells undergo mitosis. Whilst no signs of cell division were observed in cells located directly between the electrodes, some proximal cells did show signs of division (Figure 51). No cells undergoing division could be found in the regions unaffected by the pulse.

3.4. Discussion

In order to have an effect on the microtubule network a certain number of pulses need to be applied. We found that 10 pulses applied at 10 Hz had no visible effect on the microtubule dynamics whereas an application at 100 Hz caused an increase in EB3 comet length. Applying 100 pulses at 10 Hz caused both a rapid and persistent increase in EB3 comet length and a decrease in the overall number of comets. This decrease in comet number, demonstrated by the overall reduction in EB3-GFP fluorescence, implies a decrease in microtubule nucleation and polymerisation and an increase in catastrophe. This would result in an overall decrease in the number of microtubules, as supported by the reduction in tubulin-RFP fluorescence following pulse application. An increase in EB3 comet size has been shown to be due to an increase in microtubule growth rate[150], suggesting that whilst we observe an overall decrease in the number of polymerising microtubules, those that persist in polymerising do so at a faster rate post-pulse. Increase in growth speed can be attributed to either a higher concentration of available free tubulin[150] or to cellular swelling[174].

The increase in EB3 comet size was rapid, occurring within seconds. Whilst this is possibly due to an increase in free tubulin from a rapid microtubule breakdown, it could potentially also be explained by a release of sequestered tubulin from the MAP stathmin, if nsPEF were able to disrupt the electrostatic interactions between the proteins[175,176].

nsPEF has previously been shown to cause depolymerisation of the microtubule network in mammalian cells[122]. The authors concluded that the effect, however, was indirect and due to the post-pulse increase in intracellular concentrations of calcium, with calcium being known to induce microtubule instability. In this chapter we have shown for the first time in human cancer cells that nsPEF causes a breakdown of the microtubule network, this is important as microtubule isotype composition and post-translational modifications are often altered in cancerous cells[177] which can effect microtubule rigidity[178] and stability[179]. We show also that contrary to the previously published study our pulse effect persisted under calcium depleted conditions. One possible explanation for the difference in results is the pulse regimes that were used, with the mammalian cell study using 20, 600ns pulses of 16.2 kV/cm. It is possible that microtubules are more susceptible to the conditions that we used: a higher number of shorter pulses, with a larger electric field. Another supporting argument against calcium induced depolymerisation under our conditions is that the rapid disruption of microtubule growth occurs globally within the cell. We have previously shown that YO-PRO-1 entry into

the cell is polar followed by diffusion across the cell (Figure 11). Assuming that extracellular calcium also enters via the same part of the membrane, if it were responsible for the disruption we see, it could be expected that the microtubules in this area would be affected first[180]. A calcium dependent effect on EB3 was however observed when 1000 pulses were applied. Under this pulse regime the immediate EB3 comet lengthening occurred in both the presence and absence of extracellular calcium. However, whilst the longer comets persisted in the calcium free conditions, when calcium was present they underwent rapid shortening before the end of the pulse application duration. If this rapid reduction in comet length is characteristic of the effect of calcium on EB3 dynamics, then its absence when 100 pulses are applied further supports that our results, at this pulse number, are independent of calcium. We did however observe a significant increase in intracellular Ca^{2+} following pulse application and it is likely that under normal conditions, such elevations in Ca^{2+} would cause additional disruption to the microtubule network and other downstream signalling effects.

Microtubule depolymerisation following nsPEF has also been shown to occur in plants where it was proposed that the pulse acts directly on a membrane localised signalling hub formed from a kinesin and phospholipase D that cross-link microtubules and actin filaments[121]. Action on a homologous mammalian hub could perhaps also provide an alternative explanation for disruption of the actin cytoskeleton that has previously been linked to nsPEF[169] and the microtubule depolymerisation that we see. We also cannot rule out the possibility of nsPEF having an alternative, direct action on the membrane, resulting in microtubule disruption. Microtubules form many interactions with the plasma membrane including certain transient receptor potential channels[131,132], septins[133] and metabotropic glutamate receptors[134], nsPEF induced membrane trauma could cause a disruption of these interactions and a resulting loss in microtubule stability.

It is possible that nsPEFs activate other lipid signalling pathways in the plasma membrane of U87 cells that influence microtubules. Mammalian cells treated with nsPEF exhibited muscarinic receptor-like signalling with PIP_2 depletion and calcium independent accumulation of diacylglycerol (DAG)[72,127], these effects are proposed to be a result of a direct effect of nsPEF on the plasma membrane and membrane bound proteins. Agonist activation of the muscarinic receptor causes microtubule depolymerisation with translocation of tubulin to the plasma membrane, within minutes of activation, where it binds to, and inhibits the activity of, phospholipase D[124,125]. In the same time-scale we observed a similar membrane accumulation, of both tubulin and EB3 following pulse application.

Given that rapid swelling, in addition to increasing EB3 comet size, has been shown to cause microtubule depolymerisation[181] we investigated whether swelling was the cause of our observed effects. Cellular swelling is a known consequence of nsPEF[27,182,183], especially for pulses of longer durations, and this swelling has been shown to cause a breakdown of the actin network[169], which is cross-linked with microtubules. By using an isotonic sucrose HBSS, which has previously been shown to inhibit post-nsPEF swelling[169], we showed that the same initial disruption of microtubule growth was observed in the presence of sucrose. This observation is in agreement with previously published results[122]. However, EB3 fluorescence levels started to recover within the imaging period which we did not observe in the absence of sucrose. It is possible that an influx of water reduced the concentration of free tubulin, thus lowering the polymerisation rate. We further showed that our nsPEF treatment did not in fact result in any signs of osmotic swelling in U87 cells, with a tendency towards a small decrease in cell size observed instead. This could potentially be explained by the previously described nsPEF induced activation of the PIP_2/ IP_3 pathway[72,127], which in glioblastoma plays a role in cell volume regulation. Glioblastoma cells metastasise through the extracellular space in the brain, as such they have to adapt to the tight spatial limitations of this area. They achieve this by being able to dynamically adjust their cellular volume and are able to shrink by up to 35%[184]. Cell volume change can be a result of IP_3 activation by the chemotactic peptide Bradykinin, leading to the subsequent activation of outward pumping chlorine and potassium channels, with cytosolic water following via aquaporins[185–187]. Further experiments would be necessary to confirm a role of the PIP_2 pathway in the cell volume regulation and microtubule disruption that we observe.

Having discounted both obvious explanations for the microtubule disruption, calcium and swelling, we looked at the possibility that our nsPEF pulse regime might act directly on microtubules. Pulse application to microtubules that had been polymerised from purified tubulin and stabilised with taxol failed to have an effect. Whilst we did not see an effect the possibility that nsPEF acts directly on the microtubules cannot be disregarded. Lack of effect could be explained by the taxol stabilisation, which is considerably different to the stabilisation by MAPs that occurs in cells. Tubulin polymerisation is temperature dependent with polymerisation favoured at 37°C. The company providing the microtubule polymerisation kit suggest that there is a 5% loss of polymer per degree reduction in temperature without the addition of taxol. All our experiments were carried out at room temperature (around 21°C) and it is possible that if warmer temperatures were used taxol

stabilisation could be avoided. A purer and better quality of tubulin has also been suggested as a way of improving this experiment as well as testing different exposure systems.

Using wide-field microscopy we saw evidence, in the cellular environment, of bundles of microtubules buckling following the pulse. Using 3D-SIM the same was found to be true of individual microtubules. Whilst microtubule bending occurs frequently during growth, due to deflections of the growing tip, once polymerised microtubules form rigid structures that are 100 x more resistant to bending than actin[188,189]. However, buckling of microtubules, such as we observed, can occur as a natural phenomenon[190], when bends or weaknesses present in the microtubule are subjected to compressive forces such as caused by polymerisation against the cell perimeter or the activity of molecular motors[189,191,192]. Given that the EB3 comet lengthening indicates an increased rate of microtubule growth it could be imagined that the buckling we observe is in part due to more microtubules reaching, and polymerising against, the cell membrane. Microtubule bending has been shown to result in breaking, followed by depolymerisation[190], and our 3D-SIM results provide support that this is the case here. These effects might also be mediated by the electrical and/or mechanical properties of microtubules. Microtubules are dielectric structures with dipole moments that have been assessed by a number of methods, including electroorientation and simulation[193,194,195]. The resulting microtubule breakage associated with nsPEFs could therefore be caused directly by the force of the applied electric field, disrupting the electrostatic interactions of the microtubules proteins. It has already been proposed by Havelka et al.[101] that the electric fields associated with nsPEFs might be sufficient to directly disrupt microtubules and this hypothesis could be tested in future *in vitro* studies.

Bending is believed to either promote the dissociation of stabilising MAPs, cause the dissociation of tubulin dimers and/or allow for the binding of microtubule severing enzymes[190,196,197]. By increasing the amount of buckling microtubules within the cell, pulse application could therefore increase the amount of microtubule depolymerisation.

Having established that nsPEFs have an effect on the microtubule network we next sought to understand the possible knock-on effects on the rest of the cell. We first considered the effect on mitochondria and found a temporal link between the disruption of the microtubule network and loss of mitochondrial membrane potential. The loss was dose-dependent and gradual which does not fit with previously reported pulsed-induced electroporation of the inner mitochondrial membrane[22] where a more rapid loss of $\Delta\Psi_m$ would be expected. A similar

decrease in $\Delta\Psi_m$ was reported following chemical disruption of microtubules with nocodazole[135]. Mitochondria and microtubules are intrinsically linked within the cell with mitochondria being transported along microtubules by MAP motor proteins to areas of the cell that require ATP[198,199]. Nocodazole treatment disrupts this association of mitochondria to microtubules with a potential effect of opening the mPTP[135]. The opening of mPTP has also been proposed as a downstream effect of nsPEF treatment[24]. However in our case mPTP involvement seems unlikely as there was an absence of post-pulse donut shaped mitochondria, which are characteristic of the opening of the pore[171]. We were also unable to prevent $\Delta\Psi_m$ loss in the absence of calcium or in the presence of CsA, two conditions that prevent mPTP opening. Other mitochondrial pores or channels may, however, be implicated. One candidate which should be tested is the VDAC which are blocked by high levels of free tubulin leading to decreased $\Delta\Psi_m$[143,200].

A further possible explanation for the loss of $\Delta\Psi_m$ is release of pro-apoptotic proteins such as Bim which, under normal conditions, is bound to microtubules. Bim is known to dissociate from destabilised microtubules and translocate to the mitochondria[201–203]. Following translocation Bim activates Bax which has an essential role in apoptotic mitochondrial membrane permeabilisation, an event that causes loss of $\Delta\Psi_m$ [177,204].

As microtubules interact with and help regulate many channels in the cell membrane, including some that gate YO-PRO-1[205,206], we next looked at whether microtubule disruption was linked to post-pulse membrane poration. However, we found no difference in YO-PRO-1 uptake or changes in intracellular calcium levels following pulse application in cells with chemically stabilised or depolymerised microtubules, when compared to cells with no chemical treatment. This result suggests microtubules do not have a role in membrane permeabilisation, but within a cell in interphase there is a population of stable detyrosinated microtubules[207–209], as these stable microtubules are not polymerising they will be more resistant to both colchicine and taxol treatment and perhaps this persistent subset is enough to cause the permeabilisation.

Increasing the number of pulses applied to the cells resulted in a more dramatic effect on EB3 dynamics. Following the application of 500 pulses the initial EB3 comet lengthening, that we saw with 100 pulses, was rapidly replaced by comet shortening accompanied by a loss of the MTOC and disorganisation of EB3 direction. Glioblastoma cell lines, including U87, have high levels of gamma tubulin[210] which can cause non-MTOC nucleation of microtubules[211].

This type of nucleation, enhanced by high levels of soluble tubulin from microtubule breakdown, could explain these more random comet trajectories. Abrupt, mass microtubule depolymerisation just prior to nuclear envelope breakdown occurs in cells undergoing mitosis[212]. When 1000 pulses were applied a similar process occurred with EB3 uptake into the nucleus suggesting a breakdown of the nuclear envelope. This breakdown appears to be calcium dependent as it failed to occur in the absence of calcium. nsPEF have previously been shown to cause the breakdown of the nuclear membrane[213] and, under certain conditions, increase cell proliferation[214]. This, in combination with my results showing cells entering cell division following pulse application, highlights the importance of understanding the relationship between nsPEF dose and cellular response before use in a therapeutic setting. However, with a good understanding of this relationship nsPEF treatment could provide a drug-free, and locally acting, alternative to the microtubule disrupting medication commonly used in cancer therapies.

Chapter 4:
A comparison between chemical and genetically encoded calcium indicators and their application to understanding the nsPEF calcium response.

4. A comparison between chemical and genetically encoded calcium indicators and their application to understanding the nsPEF calcium response.

4.1. Introduction

4.1.1. Role of calcium within the cell

Calcium ions (Ca^{2+}) play a key role in a wide range of cellular processes, with elevation of intracellular Ca^{2+} levels being seen by cells as a signalling event. Resting intracellular calcium levels are in the order of 100 nM with cell activation occurring at concentrations above 1000 nM[215]. Ca^{2+} is involved in gene transcription, metabolism, muscle contraction as well as cell development, differentiation, proliferation and death[216,217]. The ability to influence such a wide range of processes is due to tight control of calcium by many different molecular contributors that control its spatio-temporal patterning[215].

4.1.2. Regulation of calcium in the cell

Calcium signals within the cell originate from either an influx of extracellular calcium or from the release of calcium from intracellular stores (Figure 52). The primary intracellular stores are the endoplasmic and sarcoplasmic reticulums (ER and SR). Within the ER the total concentration of calcium is greater than 2 mM, however the majority is bound to buffering proteins leaving a free concentration of 50 – 500 μM[218]. Influx of extracellular calcium is via the activation of voltage-operated channels (VGCC) activated by depolarisation of the plasma membrane, receptor operated channels activated by the binding of agonists such as ATP and acetylcholine (P2X), mechanically activated channels (TRP) activated by stress and shape changes to the cell and store operated channels that are activated by low levels of calcium in the internal stores (ORAI1 and STIM1 see section 3.1.7)[219].

Release of calcium from the ER or the SR is controlled by IP_3R and ryanodine receptors (RYR). IP3R are activated by IP_3, a secondary messenger that forms following the activation of a membrane receptor, such as a G-protein coupled receptor (GPCR). Activation of a GPCR causes the release of its bound G-proteins, which in turn activate phospholipase C (PLC). IP_3 is formed as a result of PLC hydrolysis of the plasma membrane[216]. IP_3 can then diffuse through the cell and on reaching the ER/SR bind to the IP_3R causing local calcium release. This can then lead to calcium induced calcium release which is discussed in an earlier chapter (see section 2.1.3.2). Some of the calcium released from the ER is taken up by mitochondria

through the mitochondrial calcium uniporter (MCU). Mitochondria acts as a buffer for calcium, however the uptake of too much cytosolic calcium leads to an overload and the opening of the mPTP with a subsequent release of pro-apoptotic proteins[220].

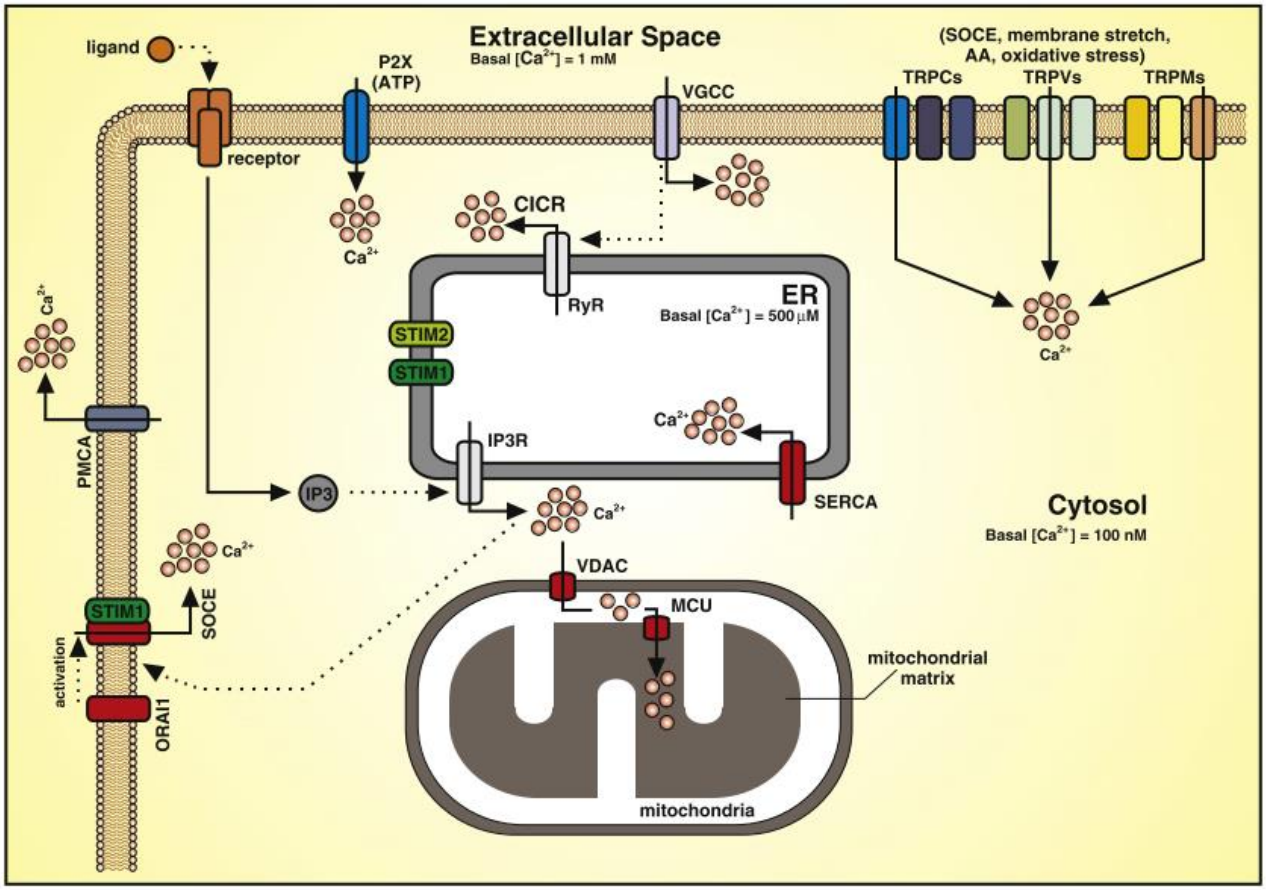

Figure 52. Calcium homeostasis within the cell.

The levels of calcium within the cell are tightly regulated by different membrane receptors and channels. Abbreviations: ER: endoplasmic reticulum; CICR: Ca^{2+}-induced Ca^{2+} release; SOCE: store-operated Ca^{2+} entry; ATP: adenosine triphosphate; AA: arachidonic acid; VGCC: voltage-gated calcium channel; TRP: transient receptor potential channel (C: canonical; V: vanilloid; M: melastatin); ORAI1: Ca^{2+} release-activated calcium channel protein 1; STIM1: stromal interaction molecule 1; IP_3: inositol-1,4,5-trisphosphate; IP_3R: IP_3 receptor; RyR: ryanodine receptor; SERCA: sarco/endoplasmic reticulum Ca^{2+}-ATPase; MCU: mitochondrial calcium uniporter; VDAC: voltage-dependent anion channel; PMCA: plasma-membrane Ca2+-ATPase. From[220]: Marchi and Pinto 2016.

Once calcium has been released by either a plasma membrane or ER/SR channel the signal can remain local or develop into a global signal or wave, this is in part due to the action of

cytosolic calcium buffers such as, calretinin and parvalbumins[215,221]. Following signalling the levels of calcium in the cell are rapidly decreased by extrusion from the cell via plasma membrane pumps (PMCA) and exchangers or by pumping back into internal stores by the SERCA pump[215].

4.1.3. Effects of the disruption of calcium homeostasis

The tight regulation of calcium within the cell is therefore governed by many different proteins working together. The disruption of one or more of these regulating proteins can result in calcium levels that are either higher or lower than normal. This deregulation of calcium homeostasis has been linked to numerous disorders including heart disease, neurological disease such as Alzheimer's and schizophrenia[222]. There is also a link to cancer progression with many cancerous cells exhibiting alterations in the channels and pumps responsible for calcium homeostasis. These alterations include modifications of the expression level or localisation and mutations that affect activity[223].

4.1.4. Methods used to measure intracellular calcium levels

The measurement of intracellular calcium first became possible with the discovery, in the early 1960's, of a jellyfish protein called aequorin that emits visible light when in contact with calcium[224]. Early experiments using this photoprotein involved its microinjection into the cells of interest[225]. In the 1980's work by Tsien and colleagues introduced new synthetic calcium indicators[226,227] that could be loaded easily into cells by using a membrane-permeant acetoxymethyl (AM) ester[228]. More recently the field has advanced by the introduction and improvement of genetically encoded calcium indicators (GECIs).

4.1.4.1. Small molecule fluorescent indicating dyes

Synthetic calcium indicators are mostly based on the calcium chelators EGTA and BAPTA modified with a range of fluorescent molecules allowing detection in different colours. The structures of the three synthetic calcium indicators used in this chapter, all based on BAPTA, are shown in Figure 53. Their well-established protocols, range of calcium affinities and commercial availability means that these chemical indicators are easy to use[229]. In general they are cytosolic dyes, including FLUO-4 and Fura Red which are used in this study. However, a limited range of membrane localised indicators are available. We have used FFP-18 a near membrane indicator based on Fura-2 which has hydrophobic tail that inserts into the membrane, with the indicator being tethered to the intracellular part of the plasma membrane.

The addition of a piperazine collar helps to prevent the indicator being pulled into the membrane[230]. Both Fura Red and FFP-18 are ratiometric indicators that allow a quantitative measurement of calcium concentrations. Given that these indicators are based on calcium chelators their results have to be interpreted with care as they can buffer the calcium within the cell and distort the response, for example they can lead to the attenuation of calcium waves[231].

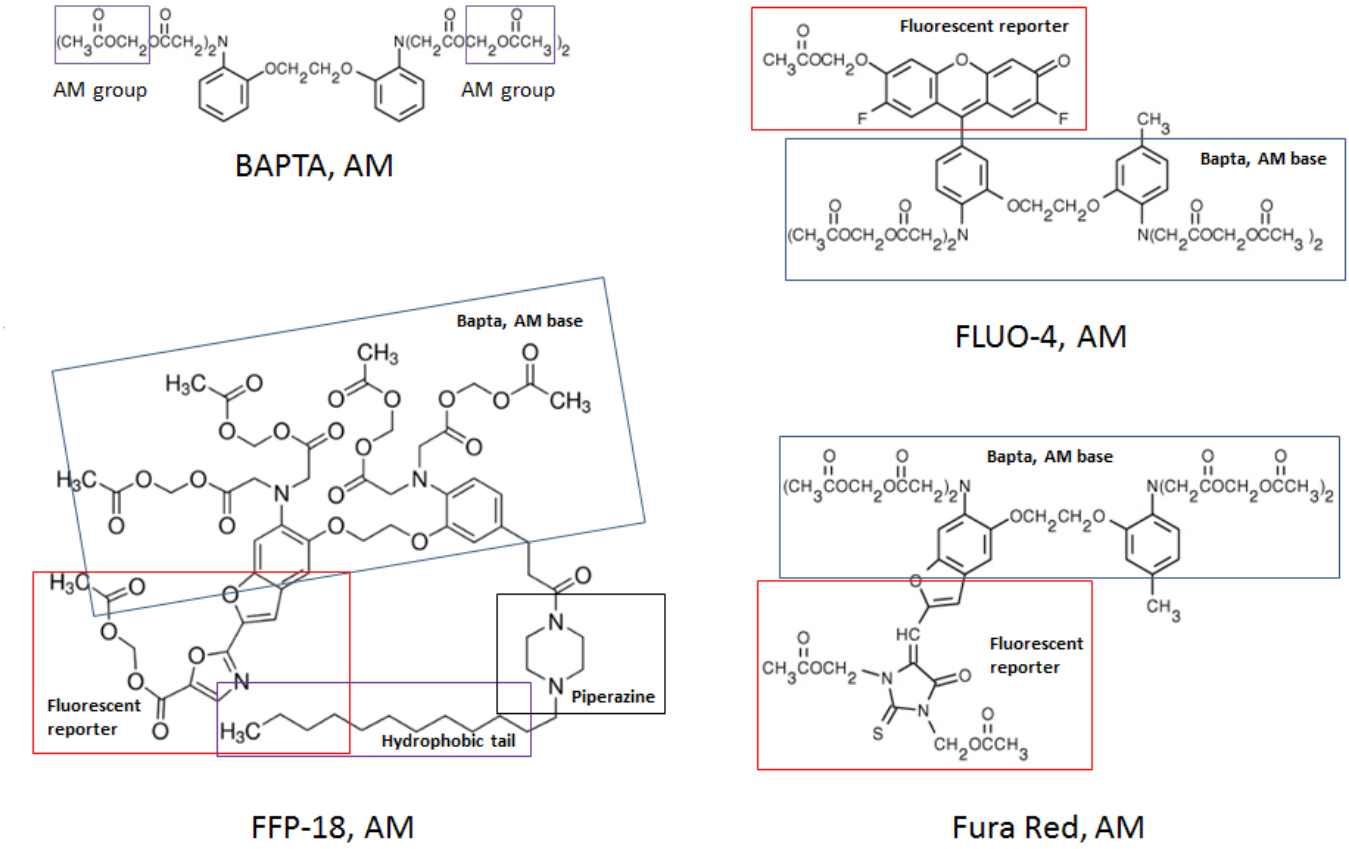

Figure 53. Chemical structure of the synthetic calcium indicating dyes used in this chapter.

FLUO-4, Fura Red and FFP-18 are both based on the calcium chelator BAPTA and composed of a fluorescent reporter molecule (highlighted by red rectangle) and an AM ester (the AM group is shown by purple rectangle in the BAPTA-AM image); the BAPTA + AM base is shown by the blue rectangles. In addition FFP-18 has a hydrophobic tail that inserts into the membrane and a piperazine collar which helps prevent the indicator being pulled into the membrane (Images adapted from thermofisher.com and sigmaaldrich.com).

4.1.4.2. Genetically encoded calcium indicators

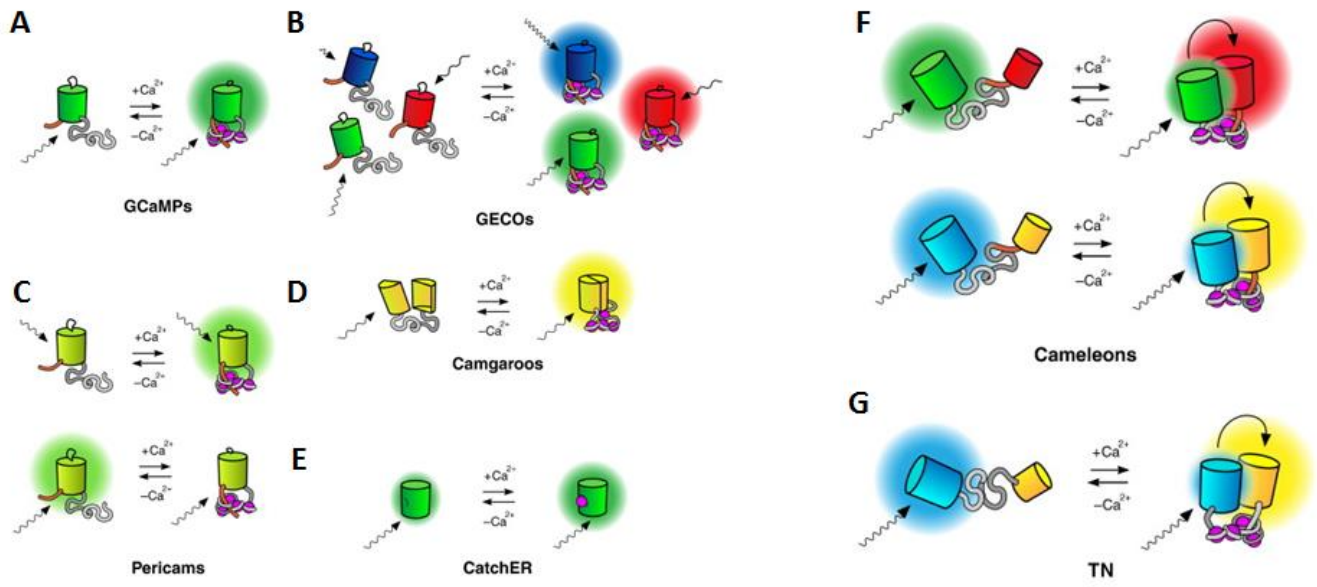

Figure 54. Examples of the different GECIs that have been developed.
GECIs that are based on a single fluorescent protein are shown in images A-E. These proteins are excited by light of different frequencies (wavy line) and binding calcium (purple circles) induces a conformational change and subsequent modification of emitted fluorescence. GECIs based on two fluorescent proteins are shown in images H-G. Binding of calcium causes a conformational change that brings both proteins together allowing FRET to occur (reproduced from Pérez and Nagai[232]).

GECIs are fluorescent proteins, expressed by the cell through molecular biology techniques, which have been modified, by fusion to a calcium binding motif, to act as calcium sensor. The calcium binding motifs include calmodulin, a Ca^{2+}/calmodulin binding peptide called M13 and troponin C. They can be genetically targeted to specific locations within the cell such as the plasma membrane or organelles and therefore can be used to measure localised calcium signals. GECIs can be split into two groups based on whether they use a single fluorescent protein or two fluorescent proteins (see Figure 54). The single fluorescent group rely on the binding of calcium inducing a conformational change in the fluorescent protein causing a detectable alteration in its fluorescence properties. Those made of two fluorescent proteins use Förster resonance energy transfer (FRET). In FRET one of the fluorescent proteins (the donor) is excited by its specific wavelength of light and when it is in close enough proximity to the second fluorescent protein (the acceptor) it is able to transfer its excitation energy to the

acceptor via long-range dipole-dipole interactions. Excitation of the acceptor results in it emitting detectable fluorescence. In the calcium unbound state FRET based GECIs have their donor and acceptor proteins separated, a conformational change induced by the binding of calcium results in the donor and acceptor being brought into close proximity. These different types of GECIs are reviewed in[232].

In this study we have used GCaMP as our GECI of interest. GCaMP uses a circularly permuted variant of enhanced-GFP (cpEGFP) as the fluorescent protein and this is fused with a calmodulin protein at its C-terminus and an M13 peptide at its N terminus. M13 interacts with calcium bound calmodulin resulting in a change of conformation cpEGFP and an increase in its fluorescence intensity[233]. Various mutations and optimizations of GCaMP have led to the development of brighter and more sensitive sensors[234–236]. We have used two versions of this GECI, GCaMP6-S which is expressed in the cytosol and a form of GCaMP5-G which is expressed as a fusion protein with archeorhodopsin leading to a PM bound expression (Figure 55). This fusion protein was originally conceived as a dual function Ca^{2+} and voltage reporter (CaViar)[237], however in this study we have only used its calcium reporter properties.

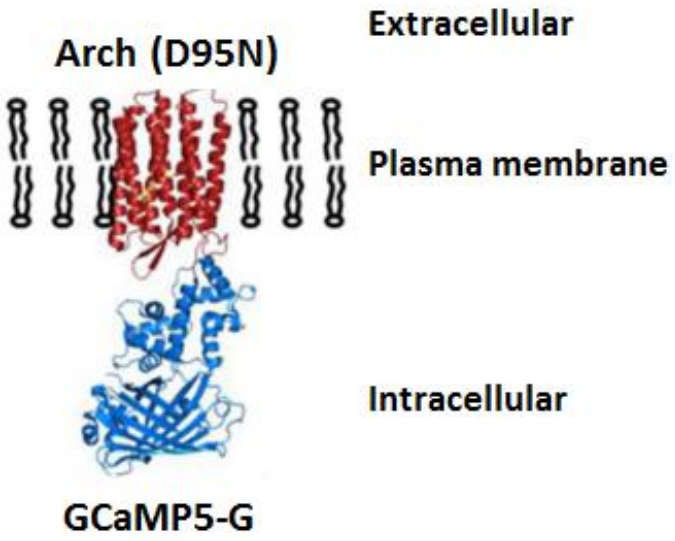

Figure 55. Structure of the CaViar fusion protein inserted into the plasma membrane.

The transmembrane voltage indicator Arch (D95N) is shown in red and the calcium reporter GCaMP5-G in blue. From Hou *et al.*[237].

4.1.5. Ways that calcium has been measured following nsPEF

An increase in $[Ca^{2+}]_i$ following application of nsPEF has been widely reported. However, it is still unclear whether the source of this calcium is from intracellular stores, such as the ER, or from extracellular calcium that enters through plasma membrane nanopores. Measurements of intracellular calcium levels following nsPEF have been measured using live cell imaging with different chemical indicators including FLUO-4[24,238,239], Fura-2[31,54,83] and Calcium Green[58,72,96,122,240–242]. Whilst most of these studies report calcium changes over a time period of seconds a high-speed imaging technique has been reported[96] that allows images to be captures approximately every millisecond. This method showed entry of calcium on the cathodic side of the cell within 3.5 ms of the application of a 600 ns, 16.2 kV/cm pulse, with the calcium signal spreading progressively across the cell in the following 60 ms. Many chemical calcium indicators, including Fura-2 and Calcium Green, show temperature sensitivity with fluorescence output being decreased at higher temperatures[243]. nsPEF has been shown to cause temperature changes within the cell[244] and this presents a potential drawback of the use of chemical indicators in nanopulse studies.

4.1.6. Objectives

Chemical indicators are easy to use and to date have been the only means used to detect post-nsPEF intracellular calcium changes. Whilst initially requiring more effort to prepare the transfected cell line, genetically encoded calcium indicators provide an alternative to chemical indicators. Once the cell line has been established they have the potential to be more economic and quicker as they are ready to use straight from the incubator, with possible detrimental effects caused by the long room temperature incubations needed by the chemical indicators are also avoided.

The objectives of this chapter are therefore to assess the use of genetically encoded calcium indicators in nsPEF studies, to see how they compare to commonly used chemical indicators and identify any other advantages they may have.

4.2. Material and methods

4.2.1. Cell culture

The human glioblastoma cell line U87-MG and U87 stably transfected with GCaMP5-G were cultured in T75 flasks at 37°C, 5% CO_2 in MEM medium (Gibco, 10370-047) supplemented with 10% FBS (Gibco, 10500), 2 mM L-glutamine (Dutscher, X0550-100), 1.1 mM glucose

(Gibco, 19002-013), 100 U/ml penicillin and 100 µg/ml streptomycin (Gibco, 15070-063). On reaching 80% confluence, cells were detached from the surface of the flask by washing twice with PBS (Gibco, 14190) and then incubating for 3-5 minutes at 37°C with trypsin (Gibco, 25200-056). Trypsin activity was stopped with the addition of an equal quantity of defined trypsin inhibitor (Gibco, R-007-100) and then centrifuged for 10 minutes at 600g. The resulting cell pellet was resuspended in MEM for use in experiments and for reseeding flasks.

4.2.2. Cell transfection

4.2.2.1. Lentiviral transfection

U87 cells were transfected with the CaViar plasmid (Addgene, 42168) using lentiviral transfection. The lentivirus was produced using a Lenti-X 293T cell line (Clontech, 632180) which is a HEK 293-T cell that has been optimized for Lenti-X virus production. These cells were cultured in DMEM (Sigma, D6429) containing 4500 mg/l glucose, L-glutamine, sodium pyruvate and sodium bicarbonate supplemented with 10 % tetracycline-free FBS (Clontech, 631105) and 1.1 mM glucose (Gibco, 19002-013), 100 U/ml penicillin and 100 µg/ml streptomycin (Gibco, 15070-063). The Lenti-X 293T cells were transfected with a Lenti-X expression vector containing the DNA coding for CaViar using the Xfect Transfection Reagent (Clontech, 631318) following a similar method as described in the following section, but with the addition of Lenti-X HTX Packaging Mix (Clontech, 631248) to the DNA and reaction buffer. Following 48 hours of culture the lentivirus was recovered by an overnight incubation at 4°C of the Lenti-X 293T cells' culture medium with Lenti-X concentrator (Clontech, 631231). U87 cells were infected with the lentivirus by direct addition with a target multiplicity of infection (MOI) of 10.

4.2.2.2. Chemical transfection

U87 cells were transiently transfected with CaViar (Addgene, 42168) or GCaMP6-S (Addgene, 40753) using Xfect Transfection Reagent (Clontech, 631318). Cells were seeded onto a 6-well dish so as to be at 50%-70% confluence the day of transfection. Following the manufacturer's protocol, for each well to be transfected, 5 µg of plasmid DNA was mixed with 100 µl Xfect Reaction Buffer, followed by 1.5 µl of Xfect Polymer. After an incubation of 10 minutes at room temperature the DNA / reagent mix was added dropwise to the well, mixed gently and incubated overnight under cell culture conditions. The culture media was

replaced the following day and cells were plated onto imaging slides for use 48 hours after transfection.

4.2.3. Preparation of cells for wide-field live cell imaging

Cells were plated at a density of 1.8 x 10^5 cells/ml into 35 mm dishes, each containing a 22 mm poly-L-lysine (Sigma, P9155) coated glass coverslip (Dutscher, 140541DD), and incubated overnight. For imaging coverslips were removed from their dishes, sandwiched into plastic imaging chambers and covered in 1 ml of room temperature HBSS (NaCl 121 mM, KCl 5.4 mM, $MgCl_2$ 0.8 mM, $NaHCO_3$ 6 mM, D-glucose 5.5 mM, HEPES 25 mM, $CaCl_2$ 1.8 mM, pH 7.3). For measurement of intracellular calcium levels with chemical calcium indicators U87 cells were incubated for 30 minutes at room temperature, in the dark, in HBSS containing 1.25 µM Fura Red, AM (Life Technologies, F3020) or 0.5 µM FLUO-4, AM (Life Technologies, F14201) or 1 µM of FFP-18 (Interchim, SC-218476) all with 0.02% pluronic acid (Life Technologies, P3000MP), then washed three times in the corresponding HBSS and incubated a further 30 minutes at room temperature.

4.2.4. Wide-field live cell microscopy

Cells were observed by epifluorescence using a Leica DMI6000 microscope with a 100x objective. Fluorescent excitation was provided by a Spectra 7 light engine (Lumencor). Emitted light was filtered and captured on an electron-multiplying charge-coupled device camera (EMCCD; Photometrics Evolve 512, Roper) with 512 x 512 pixels. The system was controlled by, and images were captured with, Metafluor (version 7.8, Molecular Devices). Protocols for each experiment were first optimised to minimize illumination in order to reduce photobleaching. GCaMP5-G and GCaMP6-S (excitation: 475/25 nm; emission: 525/50 nm) with exposure times and source intensities of 20 ms and 5%. Only cells showing good GCaMP expression were chosen for imaging. Fura Red (excitation: 475/25 nm; emission: 615/25 nm) had an exposure time of 25 ms and 5% source intensity. FLUO-4 (excitation: 475/25 nm; emission: 525/50 nm) had an exposure time of 10 ms and 5% source intensity. FFP-18 (excitation: 390/18 nm; emission: 525/50 nm) had an exposure time of 10 ms and 10% source intensity. In all experiments a 2 x binning was used.

4.2.5. Exposure of cells to nsPEF

100, 10 ns pulses, with an electric field strength of 44 kV/cm, were applied to cells at a frequency of 10 Hz using an nsPEF generator (FPG 10-1NM-T, FID Technology, Germany) with 50 Ω output impedance. A high-voltage measurement device (tap-off 245 NMFFP-100, Barth Electronics Technology, USA) connected to an oscilloscope (DPO 4104, Tektronix, USA) was used to visualize the time-domain measurements of the pulse[84–86]. Pulses were applied by positioning an electrode delivery system with a micromanipulator (Sutter MP285) comprising of two steel electrodes, separated by a gap of 1.2 mm and with 50 Ω impedance in parallel[37].

4.2.6. Image analysis

For wide-field live cell imaging experiments images were analysed using Image Analyst MKII (Image Analyst Software). Background was subtracted from the stack of images by manually drawing a region of interest (ROI) in a zone that did not contain cells and subtracting the grey level in this area from the rest of the image. ROIs were then drawn to include the entire cell of interest and fluorescence intensity data for the ROIs were generated by Image Analyst MKII.

To calculate calcium and YO-PRO-1 wave velocity a straight line ROI was drawn across the cell in the direction of the wave (Figure 56A). Using this ROI a kymograph was created, with Image J's resliced function, using only the stacks that covered the wave duration (Figure 56B). On the kymograph a line was drawn along the front of the wave and the pixel coordinates for the start (X_a,Y_a) and end (X_b,Y_b) of the line noted. The total distance, in µm, travelled was calculated by: (Y_b-Y_a) / 7.467 (with 7.467 being the number of pixels/µm in our images). The total duration of the wave (in seconds) was calculated by: X_b-X_a. Speed in µm/S was then calculated by: Distance / Duration.

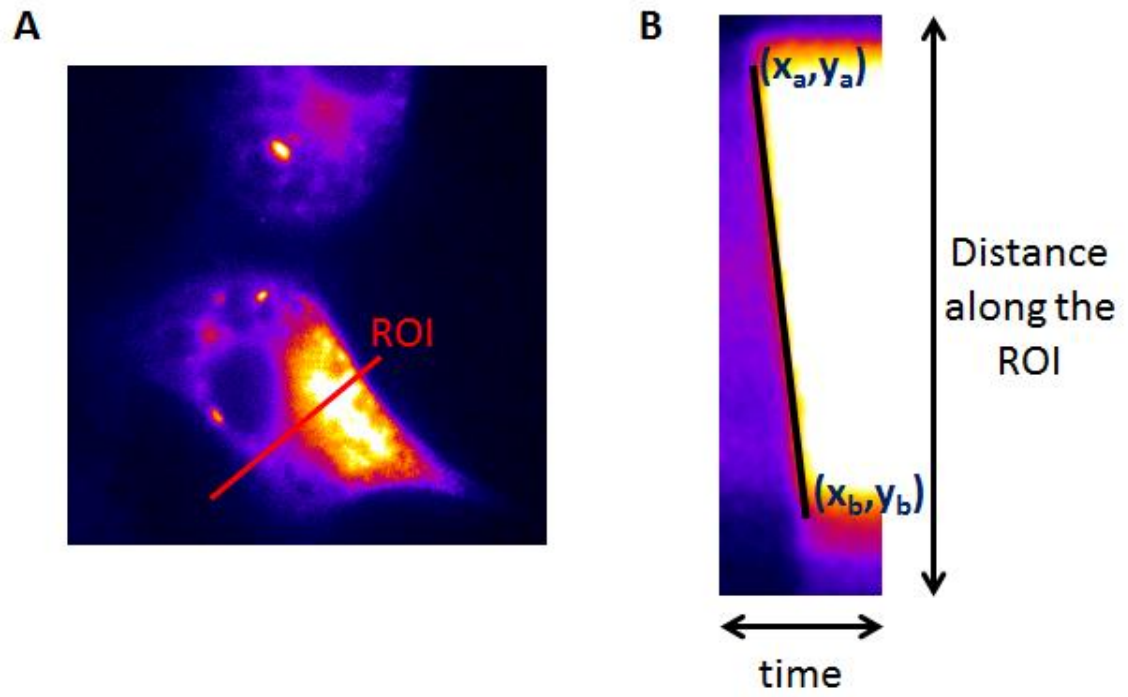

Figure 56. Calculation of calcium wave velocity.

A. Representative image showing the location of the ROI (red line) used to create the kymograph in B. The black line in B traces how the wave front travels over time. (X_a,Y_a) are the start coordinates of the wave and (X_b,Y_b) are the end coordinates.

4.2.7. Statistical analysis

Statistical analyses were performed with OriginPro 2016 software. Datasets were first tested for normal distribution using Q-Q plots and a Levene's test was used to assess the homogeneity of variance. Changes in fluorescence intensity were statistically tested over time (repeated measures) and between independent treatments (between groups) using a mixed-model two-way repeated measures analysis of variance (ANOVA). The source of significant differences identified by ANOVAs was found using pair-wise post-tests that were Bonferroni corrected. Effects were considered statistically significant when the probability of falsely rejection the null hypothesis was less than 0.05 ($p<0.05$).

4.3. Results

4.3.1. The effect of nsPEF on common chemical and genetically encoded calcium indicators

We looked first at the spatiotemporal effect of 100, 10 ns pulses applied at 10 Hz on two different types of GCaMP (membrane bound GCaMP5-G and cytosolic GCaMP6-S) and two common chemical indicators: FLUO-4 and Fura Red. GCaMP expressing cells were used directly from the incubator whereas FLUO-4 and Fura Red were both loaded for 30 minutes at room temperature in the dark, followed by washing and another 30 minute incubation, under the same conditions, to allow for de-esterification of the AM group.

For all indicators a change in fluorescence could be observed within the first second of pulse application (Figure 57) and with the exception of GCaMP5-G, which took longer, maximum fluorescence was reached by the end of the 10 second pulse application duration (Figure 58). Whilst all three of the cytosolic indicators (FLUO-4, Fura Red and GCaMP6-S) indicated a global, uniform change in intracellular calcium the membrane bound GCaMP5-G showed a polar increase in fluorescence, reminiscent of our previous observations with YO-PRO-1, before spreading as a wave across the cell.

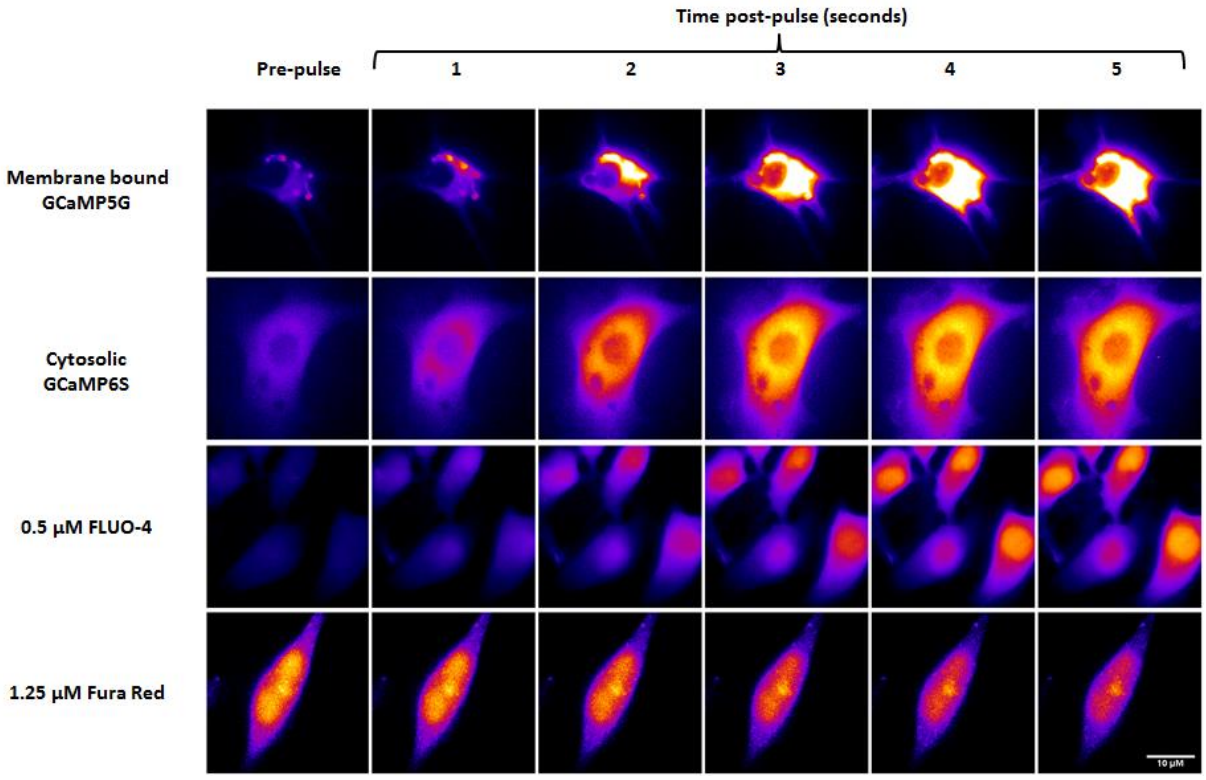

Figure 57. Spatiotemporal effect on intracellular calcium of 100, 10 ns pulses applied at 10 Hz to U87 cells visualised with different calcium indicators.

Representative live cell images of U87 cells either stably expressing the genetically encoded calcium indicator GCaMP (membrane bound expression top line and cytosolic expression second line) or loaded with the chemical calcium indicators FLUO-4 (third line) or Fura Red (bottom line). Images have been pseudo-coloured for clarity. Fura Red fluorescence decreases with increasing calcium, the other indicators show an increase in fluorescence.

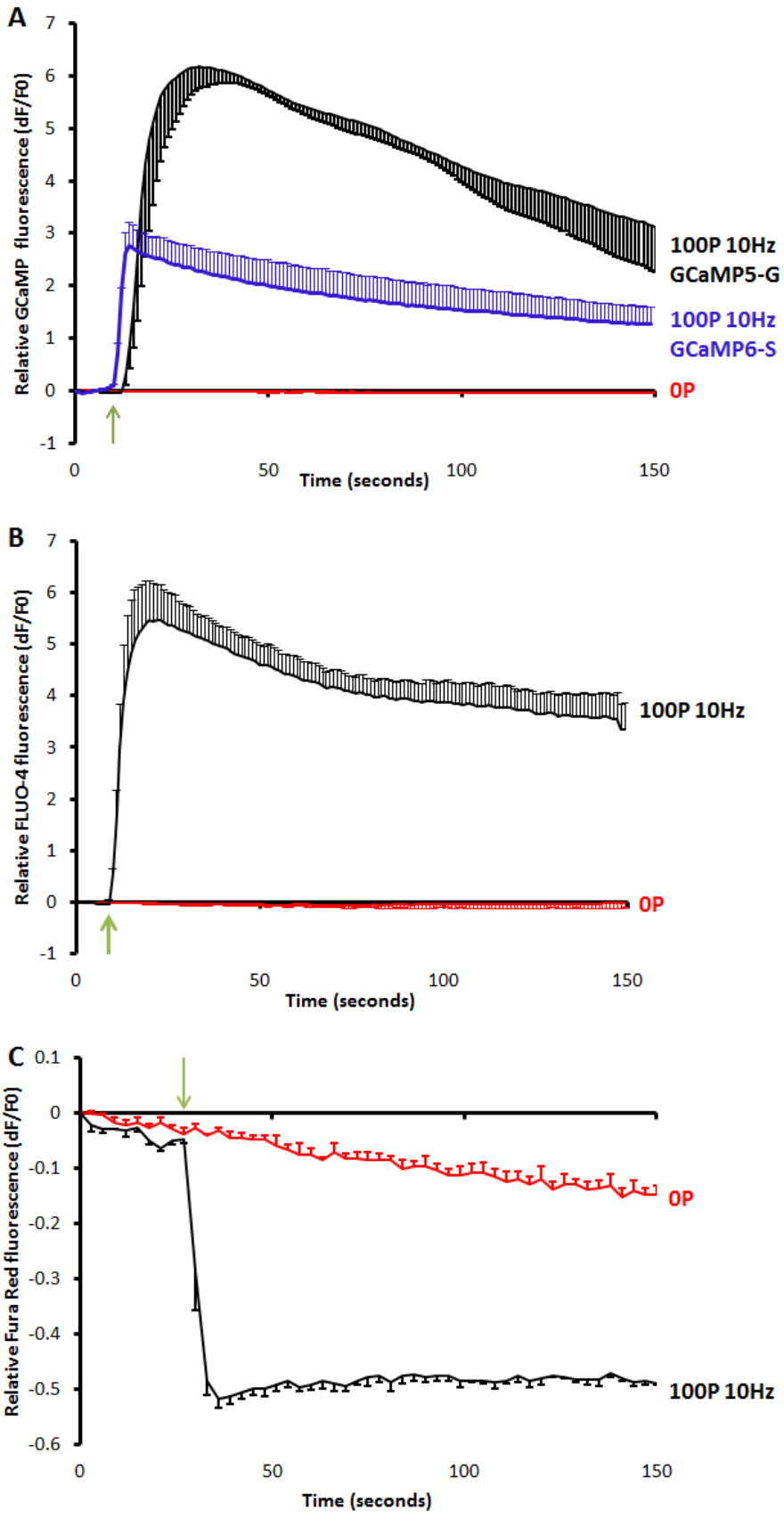
A
Relative GCaMP fluorescence (dF/F0)
7
6
5
4
3
2
1
0
-1
0
50
100
150
Time (seconds)
100P 10Hz
GCaMP5-G
100P 10Hz
GCaMP6-S
0P
B
Relative FLUO-4 fluorescence (dF/F0)
7
6
5
4
3
2
1
0
-1
0
50
100
150
Time (seconds)
100P 10Hz
0P
C
Relative Fura Red fluorescence (dF/F0)
0.1
0
-0.1
-0.2
-0.3
-0.4
-0.5
-0.6
0
50
100
150
Time (seconds)
0P
100P 10Hz

Figure 58. Change in fluorescence over time plots for live cell imaging of U87 cells either loaded with a chemical calcium indicator or expressing a GCaMP indicator.

For each condition 100, 10 ns pulses at 10 Hz were applied as indicated by the green arrow (GCaMP5-G: n = 3, GCaMP6-S: n = 2, FLUO-4: n = 3 and Fura Red: n = 3). Controls were no pulse was applied are also included (GCaMP5-G: n = 2, FLUO-4: n = 3 and Fura Red: n = 3). Error bars show SE and the arrows indicate start of pulse application.

4.3.2. Understanding the GCaMP5-G calcium wave

4.3.2.1. How does the GCaMP5-G Ca2+ signal vary with different pulse numbers and different frequencies of application?

We next sought to further investigate the calcium wave that was unique to GCaMP5-G. We applied increasing numbers of pulses at increasing frequencies to see if there was a threshold for the wave occurrence and to better understand the dose-response relationship between nsPEF and intracellular calcium changes. We found that increasing the number of pulses increases the total amount of fluorescence change with the three 100 pulse conditions reaching comparable levels of maximum change in fluorescence and similar being true of the three 10 pulse conditions. The time taken to reach maximum fluorescence is dependent on the frequency of application at 100 pulses, the 100 Hz application reached maximum fluorescence 2 seconds after the start of pulse application, whereas, at 1 Hz the maximum was reached 87 seconds after the start (total pulse period 100 seconds). The application of 1 pulse failed to cause any appreciable increase in fluorescence (Figure 59A). The enlargement of the axis in Figure 59B demonstrates further that increasing the frequency of pulse application increases the rate of fluorescence change. Regardless of the total number of pulses applied the onset of fluorescence increase depends on pulse frequency; at 100 Hz the onset is immediate whereas at 1 Hz the onset does not occur until 7 seconds after the first pulse is applied.

Figure 60 shows that in all cases the start of the calcium signal is polar (top right part of each cell). For 10 pulses applied at 1 or 10 Hz this initial calcium spike occurs but is not propagated across the cell, however, for 10 pulses applied at 100 Hz a calcium wave follows the spike. For the 100 pulse application all three frequencies resulted in a calcium wave the speed of which depended on pulse frequency. Quantification of the wave velocity showed the following speeds in μm/s ± SE: 100P 100 Hz: 7.23 ± 0.89; 100P 10 Hz: 2.42 ± 0.43; 100P 1 Hz: 0.40 ± 0.04 (Figure 61). YO-PRO-1 also showed a similar polar entry before crossing the cell as a wave. Quantification of the YO-PRO-1 wave showed a similar speed for 100 pulses

applied at both 10 (0.68 ± 0.04 µm/s, n = 4) and 100 Hz (0.71 ± 0.10 µm/s, n = 4). These speeds are comparable with the calcium wave observed at 1 Hz.

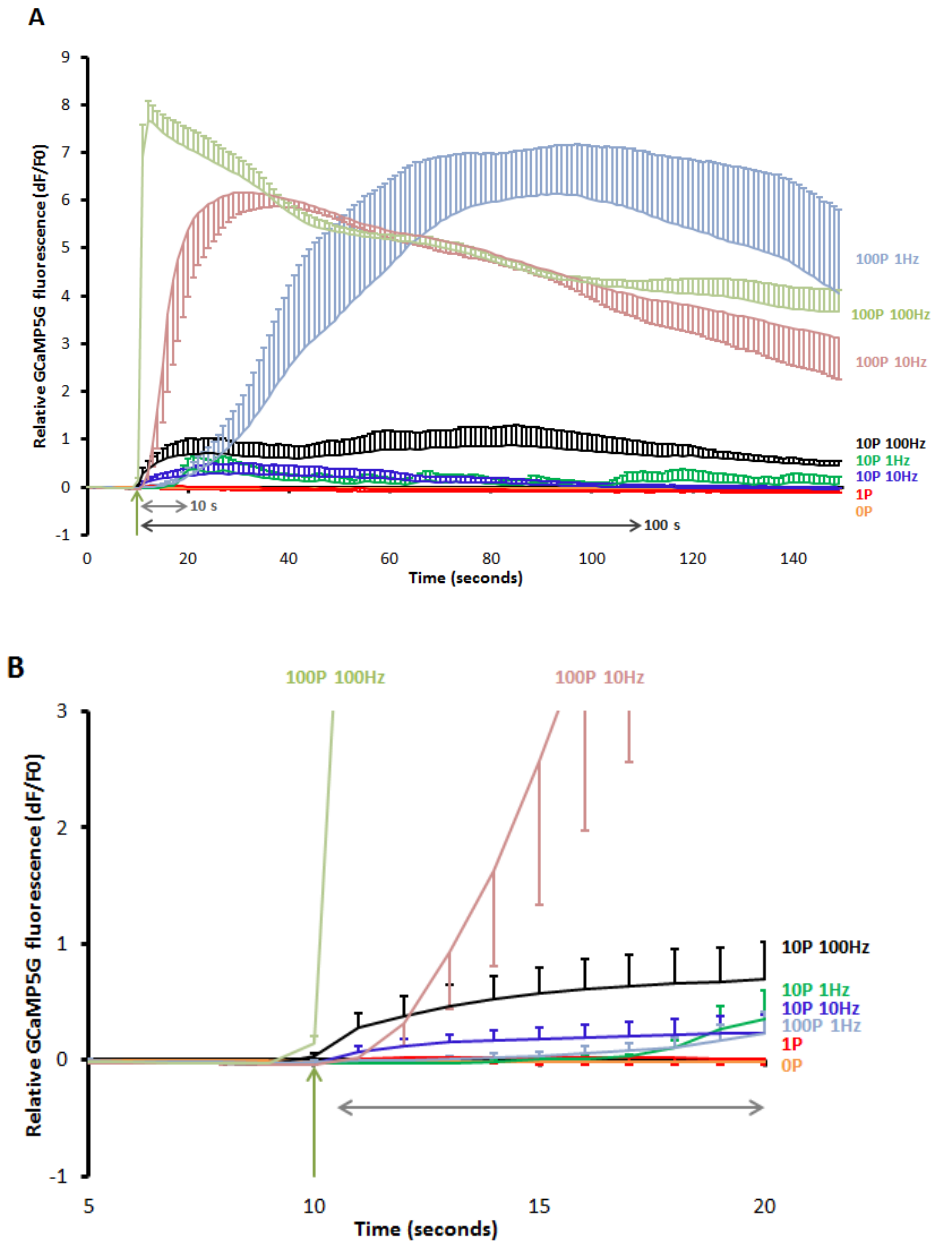

Figure 59. Change in fluorescence over time plots for live cell imaging of U87 cells expressing GCaMP5-G.

Figure A shows fluorescence over the whole imaging period with figure B being an enlargement of the period just before and after pulse application. Increasing pulse numbers and frequencies were applied: 100 pulses 100 Hz n = 3, 100 pulses 10 Hz n = 3, 100 pulses 1 Hz n = 4, 10 pulses 100 Hz n = 2, 10 pulses 10 Hz n = 3, 10 pulses 1 Hz n = 3, 1 pulse n = 3 and 0 pulses n = 2. Error bars show SE.

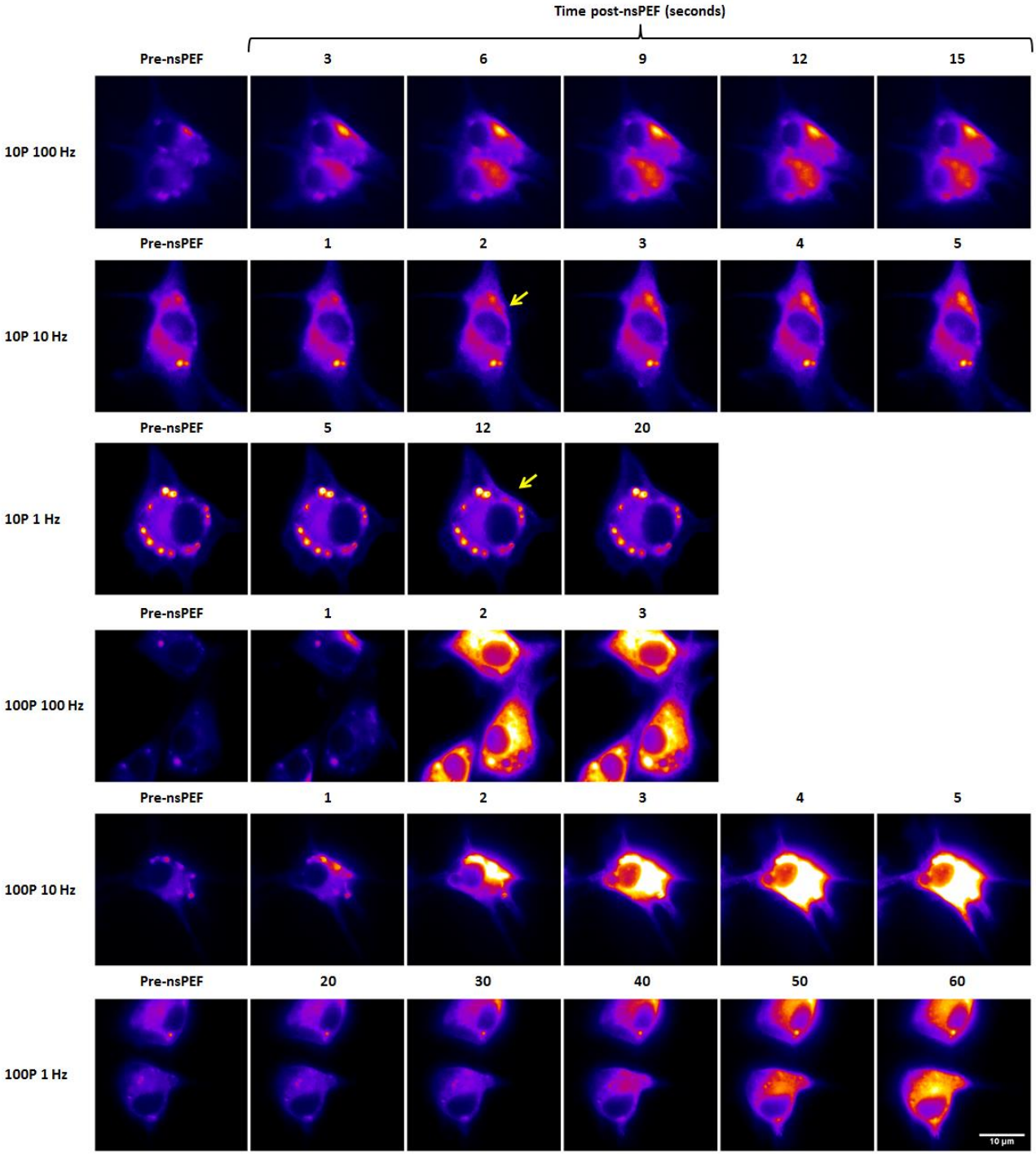

Figure 60. Spatiotemporal effect on intracellular calcium of different pulse numbers and frequencies visualised with GCaMP5-G.

Representative lives cell images of U87 cells expressing GCaMP5-G exposed to increasing number and frequencies of 10 ns pulses. Images have been pseudo-coloured for clarity. Yellow arrows indicate the zone of increased fluorescence in cells where the effect is not obvious. Times shown vary between pulse conditions.

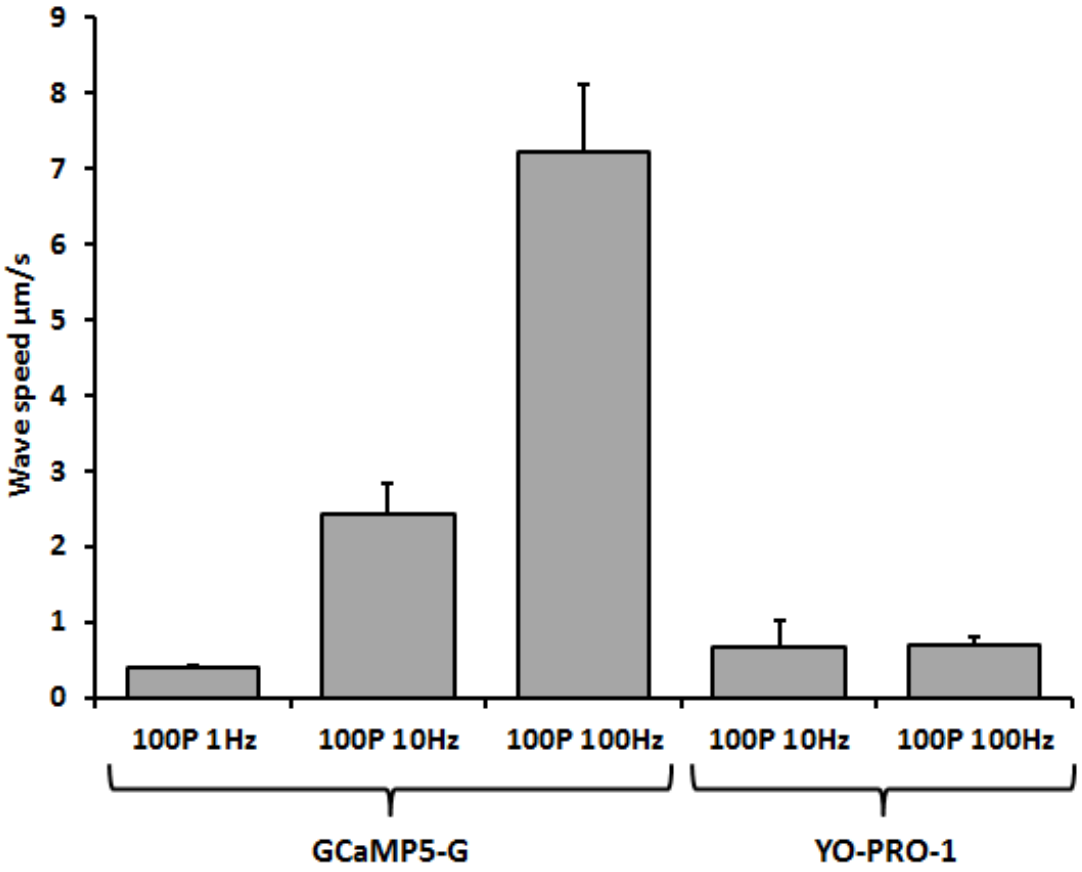

Figure 61. Speed of the intracellular calcium wave following application of 100 pulses at increasing frequencies.

The velocity of the calcium wave front was calculated in U87 cells expressing GCaMP5-G that were exposed to 100, 10 ns pulses at either 1 Hz (n = 4), 10 Hz (n = 3) or 100 Hz (n = 4). The same was done to measure the wave speed of YO-PRO-1 entering cells treated with 100, 10 ns pulses at either 10 Hz (n = 4) or 100 Hz (n = 4). Error bars show SE.

4.3.2.2. The relationship between frequency and onset of increase in intracellular calcium – comparison with FLUO-4

To see if the delay in the increase in fluorescence at lower pulse frequencies was unique to GCaMP5-G we compared the effect of 100 pulses applied at 10 Hz and at 1 Hz in cells loaded with FLUO-4. We found that, unlike in GCaMP5-G cells, at both frequencies the onset of the increase in fluorescence was directly after the start of pulse application. However, in

agreement, the rate of increase is slower, and the maximum fluorescence obtained was lower, for the 1 Hz application (Figure 62).

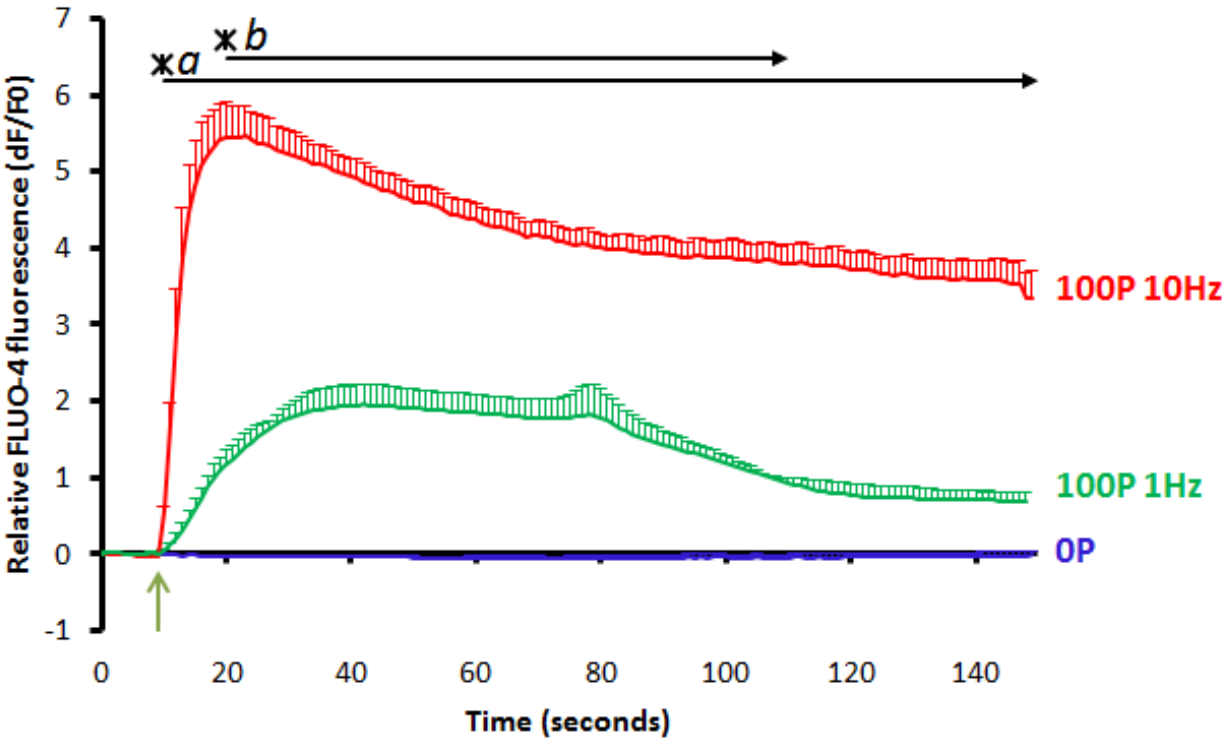

Figure 62. The effect of 100, 10 ns pulse applied at 10 or 1 Hz on intracellular calcium in U87 cells measured by FLUO-4.

Change in fluorescence over time plots for live cell imaging of U87 cells loaded with FLUO-4. The blue line denotes averages for control experiments (n = 3), where no pulses were applied. The red line denotes averages for 100 pulses applied at 10 Hz (n = 3) and the green line averages for 100 pulses applied at 1 Hz (n = 3). The start of pulse application is denoted by the green arrow. Asterisk *a* indicates a significant difference between the 100 pulse at 10 Hz response and the 100 pulse at 1 Hz and control, asterisk *b* indicates a significant difference between the 100 pulses at 1Hz and the control, as reported by two-way repeated measures ANOVA with Bonferroni tests, $F(5.29, 15.88) = 29.04$, $p < 0.05$. Error bars show S.E.

4.3.2.3. Does nsPEF cause intercellular waves?

To further understand the calcium waves we looked to see if the wave was confined as an intracellular signal or if it was able to spread from cell to cell. To do this we applied 100 pulses at 10 Hz to clusters of GCaMP5-G expressing cells (Figure 63) and found that in all

cells within the field of view the calcium increase started in each cell at the same time, always in the top right segment of the cell, and spread across all cells with comparable timing and velocity. Repeating the experiment with a lower objective, to incorporate more cells, would be a useful for the future as it would show if the wave propagates to cells that are less directly affected by the pulse.

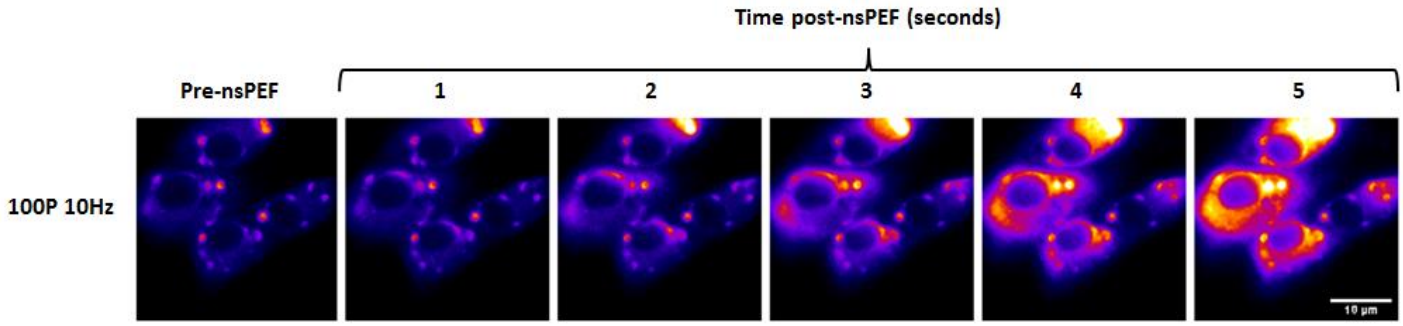

Figure 63. Wave spread in clusters of U87 cells following nsPEF.
Representative live cell images of a cluster of U87 GCaMP5-G cells exposed to 100, 10 ns pulses at 10 Hz. Images are pseudo-coloured for clarity.

4.3.2.4. Is the intracellular wave propagated by calcium induced calcium release?

Semenov *et al.*[31] showed that under their pulse conditions nsPEF causes calcium release from internal stores via CICR. CICR is propagated through activation of IP_3R leading to release of calcium, and calcium waves. To see if CICR was involved in our wave we followed Semenov in using 50 µM of 2-APB to inhibit IP_3R. We found however that 2-APB had no impact on the time-course of fluorescence increase when compared to untreated cells (Figure 64A) nor did it eliminate the wave (Figure 64B). Quantification of the wave speed found it also to be comparable to untreated cells (2.37 ± 0.39 µm/s, n = 3). As a further test we depleted the intracellular stores with thapsigargin and applied 100 pulses at 10 Hz in Ca^{2+} HBSS, this treatment also failed to prevent the wave (Figure 65).

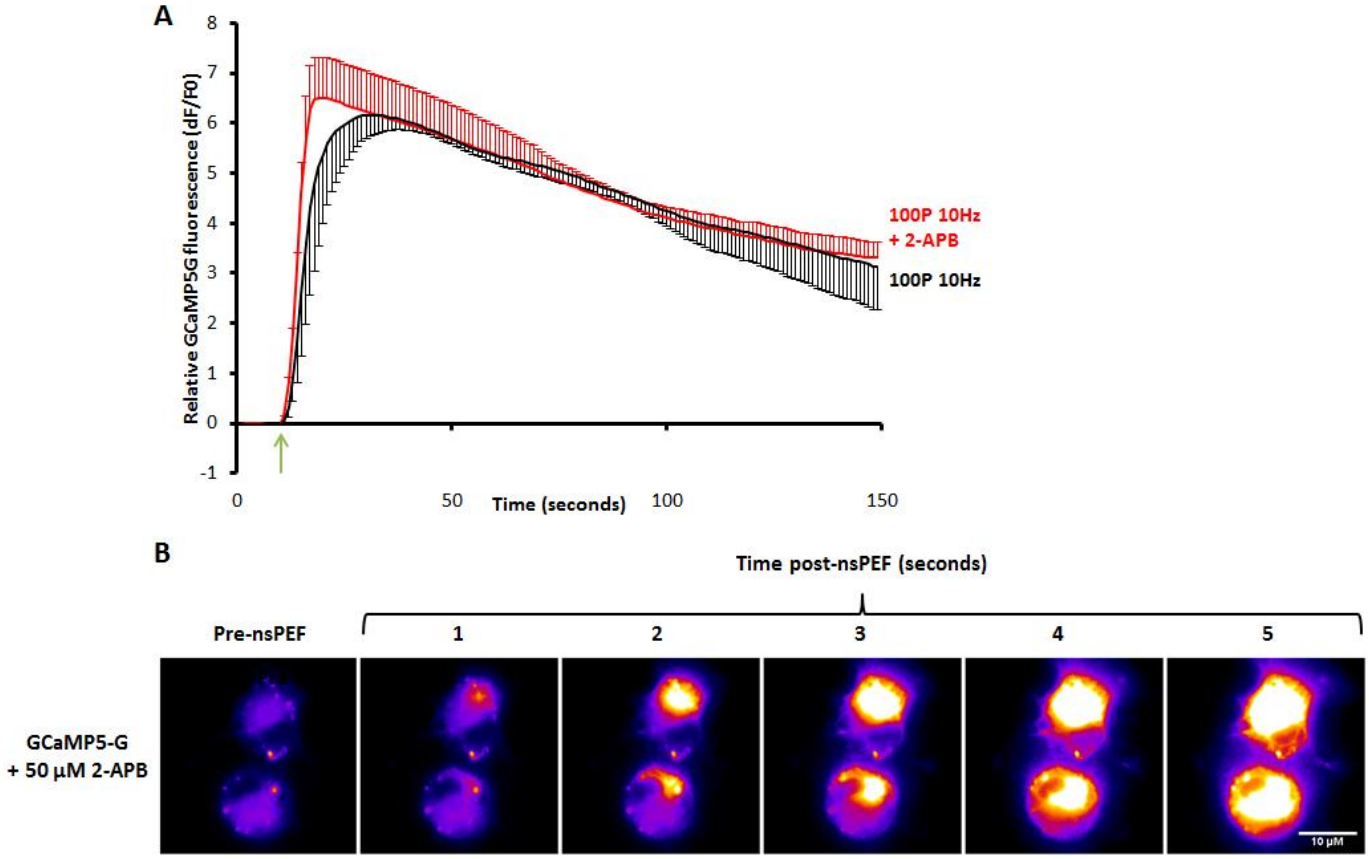

Figure 64. Effect of IP3R inhibitor, 2-APB, on the calcium wave.

Change in fluorescence over time plots for live cell imaging of U87 cells expressing GCaMP5-G. Cells were incubated with 50 µM 2-APB (red line, n=3) or without (black line, n=3) before application of 100, 10 ns pulses at 10 Hz. There is no significant difference in change of fluorescence between cells treated or not with 2-APB, as measured by two-way repeated measures ANOVA with Bonferroni tests, $F(1.97, 7.90) = 0.52$, $p > 0.05$. Error bars show S.E. B. Representative live cell images of U87 GCaMP5-G cells incubated with 50 µM 2-APB and exposed to 100, 10 ns pulses at 10 Hz. Images are pseudo-coloured for clarity.

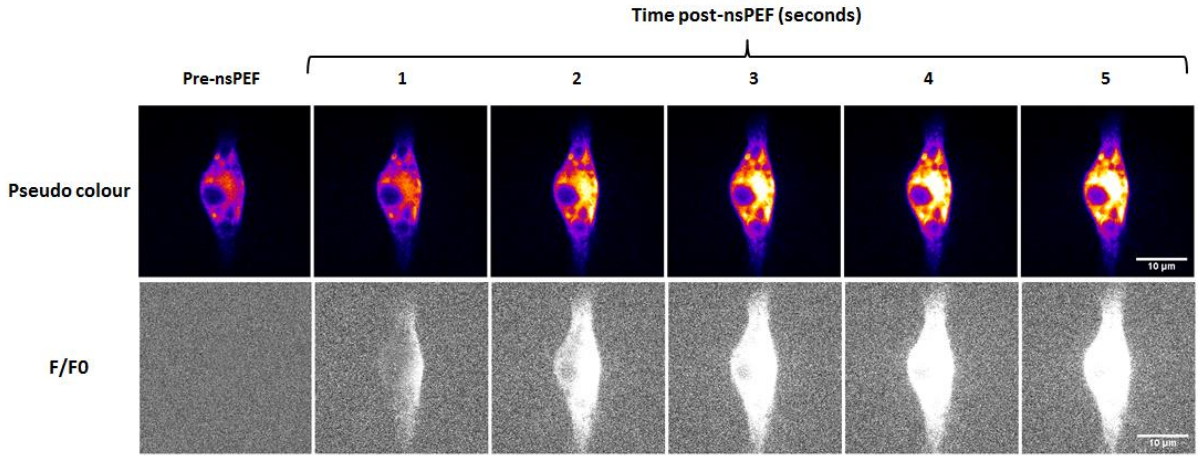

Figure 65. Effect of intracellular store depletion, with thapsigargin, on the calcium wave. Representative live cell images of U87 GCaMP5-G cells, whose intracellular calcium stores had been depleted by incubation with 1 µM of thapsigargin for 30 minutes, exposed to 100, 10 ns pulses at 10 Hz. In the top panel the images are pseudo-coloured and in the bottom panel the same cell is shown as relative change in fluorescence (F/F_0) to make the wave, seen in white, easier to visualise.

4.3.2.5. Is the wave due to the dye being tethered to the membrane?

Of the calcium indicators measured GCaMP5-G was the only one that was tethered to the membrane. As mobile, cytosolic buffers have previously been shown to buffer calcium waves, whereas immobile ones do not[245,246], we hypothesised that this difference could be responsible for the wave that we see with GCaMP5-G. To test this we loaded cells with a synthetic calcium indicator, FFP-18, that is also tethered into the PM. We found that we were able to measure an increase in intracellular calcium following the pulse application and that this increase occurred in a wave (Figure 66). When FFP-18 ($\overline{X}$ = 3.42 µm/s, S.E. = 0.3, n = 8) was compared to GCaMP5-G ($\overline{X}$ = 2.42 µm/s, S.E. = 0.43, n = 3) by a two-tailed t-test there was found to be no difference in wave speed [t(4) = 1.92, p = 0.13].

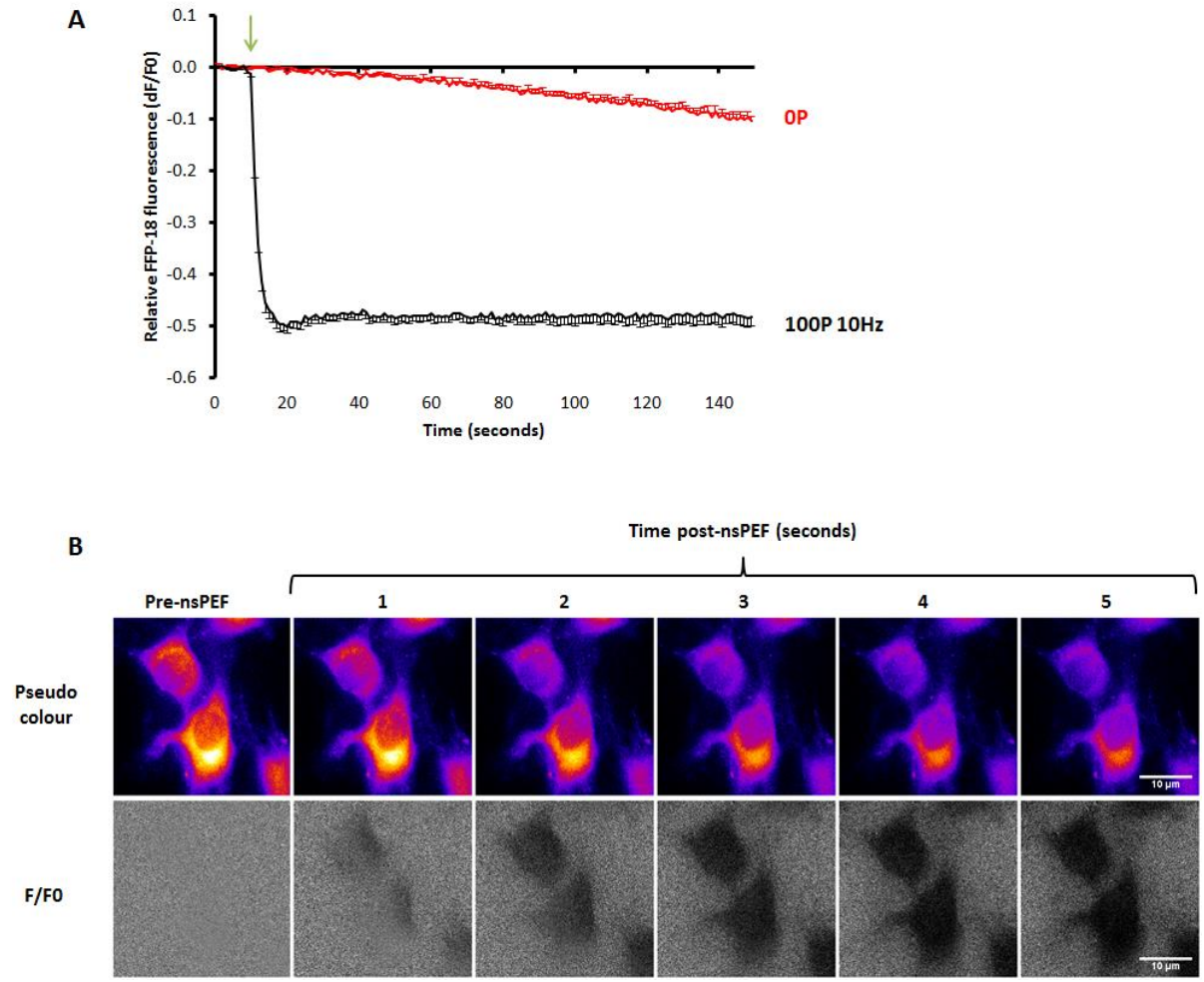

Figure 66. The effect of 100, 10 ns pulse applied at 10 Hz on intracellular calcium in U87 cells measured by FFP-18.

A. Change in fluorescence over time plots for live cell imaging of U87 cells loaded with FFP-18. Cells were exposed to 100, 10 ns pulses at 10 Hz (black line, n = 19 over 8 independent experiments), control cells were not exposed to nsPEF (red line, n = 16 over 6 independent experiments). A decrease in fluorescence represents an increase in intracellular calcium. Error bars show S.E and the green arrow the start of pulse application. B. Representative live cell images of U87 cells loaded with FFP-18 and exposed to 100, 10 ns pulses at 10 Hz. In the top panel the images are pseudo-coloured and in the bottom panel the same cells are shown as relative change in fluorescence (F/F_0) to make the wave, seen in black, easier to visualise.

4.3.3. Are the hotspots with the GCaMP5-G cells due to viral transfection?

Resting, virally transfected, GCaMP5-G expressing cells all showed persistent hotspots of fluorescence (Figure 67) that became more intense upon nsPEF application. We speculated that it could be an artefact of the transfection method and perhaps linked to the location in

which the virus had entered the cell. However, cells that underwent a chemical transfection demonstrated the same presence of fluorescence hotspots.

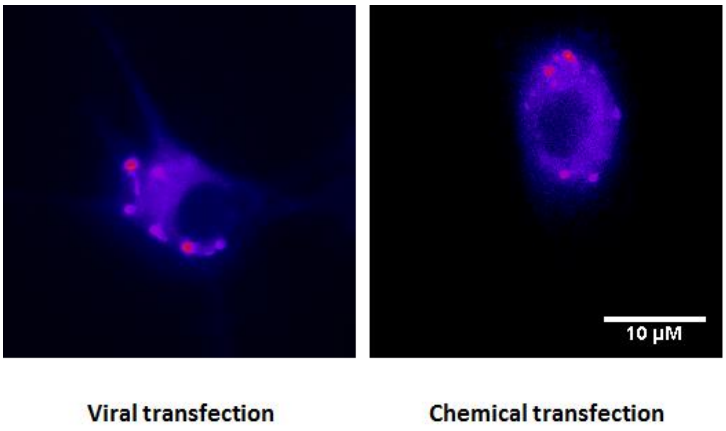

Figure 67. Hotspots appear in both virally transfected and chemically transfected GCaMP5-G cells.
Representative live cell images of U87 GCaMP5-G cells either transfected virally (left) or chemically (right). Images are pseudo-coloured for clarity with the hotspots of fluorescence visible in pink.

4.4. Discussion

The effect of nsPEF on intracellular calcium levels has been widely investigated and reported, however, no published nsPEF study has used GECIs. This chapter has compared nsPEF response using three commercially available synthetic calcium indicators, two of which are commonly used, and two forms of the GECI GCaMP. The overall objective was to access the suitability of GECIs in nsPEF studies and to see what advantages they had over synthetic indicators.

All the synthetic indicators had the advantages of being easy to use straight from the packet with a common loading protocol lasting in total 1 hour. In contrast the GCaMP cells were more complicated to prepare involving plasmid amplification and purification followed by lentiviral transfection of the cells. However, once transfected the GCaMP cells were ready to use straight from the incubator increasing the number of experiments that could be done in a day. Loading of the synthetic dyes also had to be carried out at room temperature in HBSS, in order to prevent dye compartmentalisation or loss of dye[87], resulting in possible detrimental effects on the cell.

For imaging selecting cells loaded with the synthetic dyes was rapid as all cells showed similar levels of fluorescence. Choosing a suitable GCaMP cell for imaging was more challenging as our cells had not undergone antibiotic selection to create a stable cell line. Therefore the cells on the imaging slides had different levels of GCaMP expression and each slide had to be searched to find a cell expressing a suitably high level of fluorescence.

All of the indicators used showed an increase in intracellular calcium levels following the application of nsPEF. However, cells that only expressed GCaMP weakly would fail to show a response. Of the five indicators only Fura Red and FFP-18 photobleached, even after optimisation of acquisition conditions (amount of dye loaded, exposure time, source intensity, number of acquisitions). This is possibly due to the slightly higher exposure time needed to capture the lower level of initial fluorescence and the subsequent decrease following pulse application. This impact of the photobleaching could be limited by exploiting the dual excitation properties of Fura Red and FFP-18 to give ratiometric measurements.

Following the application of 100, 10 ns pulses at 10 Hz FLUO-4, Fura Red and GCaMP6-S all showed a uniform, global increase in calcium with an onset immediately after pulse application. GCaMP5-G, however, showed a polar spike in calcium, occurring 1 second after the start of pulse application, which then spread across the entire cell in a wave. The same wave was seen with FFP-18. The time taken for each dye to reach maximum change in fluorescence following the start of pulse application varied: GCaMP6-S: 4 seconds, Fura Red: 6 seconds, FLUO-4: 14 seconds, FFP-18: 18 seconds and GCaMP5-G: 22 seconds. These time differences can potentially be attributed to the calcium affinity of each dye as those with a higher affinity will bind the calcium more readily than those with lower affinities. Of the four, GCaMP6-S has the highest affinity (Kd = 144 nM)[247] compared to the lower affinities of FLUO-4 (Kd = 345 nM)[229], FFP-18 (Kd = 400nM)[248] and GCaMP5-G (Kd = 447 nM)[247]. Fura Red should therefore, logically, have an affinity somewhere between that of GCaMP6-S and FLUO-4, however, it has the highest Kd (650 nM)[249] of all four indicators. That it reaches it maximum change in fluorescence quicker than FLUO-4 is perhaps due to it being used at a higher concentration (1.25 µM vs 0.5 µM) and therefore there is more dye available to bind calcium. Also of note is that we cannot know the amount of GCaMP6-S in the cells that we imaged. As cells with higher levels of basal fluorescence were chosen it is likely that their concentrations of GECI were high and this could also play a role in the speed of the increase in fluorescence.

GCaMP5-G and FFP-18 are unique amongst the indicators studied in that they are membrane bound whereas the others are free within the cytosol. This difference may explain their slower responses and why we only saw a calcium wave with these indicators. As all calcium indicators are essentially calcium buffers they will have a perturbing effect on the underlying calcium signal. It has been shown by modelling experiments that mobile buffers, which would include FLUO-4, Fura Red and GCaMP6-S, are able to eliminate calcium wave activity whereas immobile buffers, such as GCaMP5-G, will have little effect[245]. This has been also been demonstrated experimentally[246,250] and can be explained by the mobile buffer contributing to the diffusional equilibration by binding calcium in one area and releasing it in another[249]. Calcium waves following pulsed fields have been reported for ms pulses[251], but with the exception of one study that used high speed imaging[96] and one looking at electrically excitable cardio myocyte cells[252], it is generally agreed that they do not occur with nsPEF[32,251]. This is the first study to investigate the nsPEF induced calcium response with a membrane bound indicator and suggests that a wave can occur but may previously been masked by mobile indicators.

When we looked further at the GCaMP-5G response to nsPEF we found that increasing the number of pulses increased the maximum change in fluorescence, in agreement with previous work[32]. The value of the peak change in fluorescence, especially when 100 pulses were applied, remained comparable regardless of the frequency of application, however the time taken to reach this peak fluorescence was longer for lower frequency applications. FLUO-4 showed a similar frequency dependent change although its maximum peak fluorescence was lower for 100 nsPEF applied at 1 Hz than at 10 Hz. These frequency differences are likely a result of delayed entry, due to slower poration with lower frequency pulses and a similar result was seen with YO-PRO-1 uptake (Figure 11). When we looked at the speed of the calcium wave we found that those induced by lower pulse frequencies took longer to move across the cell than those from faster frequency pulses. This is not however the case for the YO-PRO-1 wave where those generated by the application of 100 pulses at either 10 Hz or 100 Hz were both the same speed as the 100 pulse 1 Hz calcium wave. Temperature has been shown to alter the velocity of calcium waves[253] with faster calcium diffusion occurring at higher temperatures. More cell heating occurs with faster nsPEF application frequencies[244] providing a potential explanation for the differences in calcium wave velocities that we observed. The diffusion of YO-PRO-1, being a bigger molecule, is perhaps less affected by temperature. The velocity of the calcium waves observed here were in close agreement with

previously reported fast calcium waves (non-fertilization waves) which are in the range of 3-30 µm/s[254].

We considered that the calcium wave was either due to entry from the extracellular solution or a result of CICR from the ER. Given the polar origin of the calcium wave mirroring the entry of YO-PRO-1, and the lack of calcium response we have seen under EGTA conditions (Figure 19) it seems likely that the calcium source is extracellular. This is supported by our inability to prevent the wave under conditions that favour CICR inhibition. Whether this entry is through nanopores or through one of the calcium channels in the PM remains to be confirmed. P2X7R is a candidate given that it also gates YO-PRO-1 and we have shown some evidence that its inhibition can prevent nsPEF entry of this dye (Figure 12). Seeing if the P2X7R inhibitor probenecid was able to prevent the intracellular calcium signal would be an interesting future experiment.

For 10 pulses applied at 1 or 10 Hz only the initial calcium spike occurred, which failed to propagate across the cell. The same, however, is not true for YO-PRO-1 which showed waves under these pulse conditions, but with a reduced maximum fluorescence when compared to more intense conditions. This suggests that the absence of the wave is due to less calcium entrance following the nsPEF treatment which the cell is able to buffer locally.

The hotspots present on cells expressing GCaMP5-G, which are not a result of the viral transfection process, still remain to be identified. Similar sized spots, due to TRPA1 channels, were seen in astrocytes expressing a form of GCaMP-3 that is attached to the PM by a membrane tethering domain called Lck[255]. These spots, however, were transient, lasting only for seconds whereas the ones we observed were stable lasting the entire 30 minute imaging period in non-nsPEF treated cells. Transient spots were also observed in cardiomyocytes expressing CaViar [256]. The lack of hotspots with the FFP-18 dye suggests that they are an artefact of the CaViar fusion protein expression as opposed to real, membrane localised, high-calcium domains.

Whilst chemical indicators are easy to use, with standard protocols, there are advantages of using GECIs for studying nsPEF calcium responses. Whereas chemical indicators are in general cytosolic, GECIs can be expressed in specific subcellular locations. Here we have shown the advantage of their membrane expression to demonstrate influx of extracellular calcium. Whilst this was also possible with the FFP-18 chemical indicator obtaining the dye was difficult with an 8 month delay between the first order attempt and actual delivery to the

lab. The ability to tag to other locations within the cell could also be used to further investigate the nsPEF response. For example, using a GECI expressed within the ER could show if there is indeed a loss of calcium from intracellular stores. GECI expressing cells are also ready to use from the incubator, increasing experimental throughput and any negative effects of room temperature incubations. As disadvantages the time taken to generate the stable cell line can be long and needs to be repeated if a different cell line is to be studied.

Chapter 5:
Conclusion and perspectives

5. Conclusion and perspectives

With GBM being such a devastating disease for both sufferers and their family and friends the search for new, more effective treatments is imperative. nsPEF is showing clinical promise, with minimal side effects, for the treatment of skin cancers and there is much research underway into their application to other tumour types. This PhD thesis provides the first detailed description of the *in vitro* effects of nsPEF on a human glioblastoma cell line (U87-MG) with the aim of providing preliminary data to support future *in vivo* studies and any eventual patient based trials.

We used an electrode based delivery system to apply nsPEF to U87 cells and observed their responses in real time using live cell imaging. We initially sought to characterise three nsPEF responses, plasma membrane poration, increased intracellular calcium levels and loss of mitochondrial membrane potential; all of which have been already well documented in other cell types and with other delivery systems. We then further investigated the less well documented effect on the microtubule network using probes and imaging techniques that are novel to nsPEF research. Finally we assessed the applicability of GCaMP, a type of genetically encoded calcium indicator, to nsPEF studies and compared it with various commercially available and commonly used chemical calcium indicators.

Our results measuring YO-PRO-1 uptake, following the application of a repeated number of pulses, support the widely held view that nanoporation occurs as a result of nsPEF, and that the effect is more pronounced near the electrodes. When only a single pulse was applied we showed novel evidence that implicated a permeability channel, formed by the P2X7 receptor, in the uptake of YO-PRO-1. The pore opening however appears to be an indirect effect of the pulse and is instead mediated by ATP release from the pannexin-1 channel. The results presented are however preliminary and further work is required to demonstrate, pharmacologically, YO-PRO-1 entry through the P2X7R channel and also the ability to block this with antagonists. As probenecid has a dual inhibitory action on P2X7R and pannexin-1 it would also be interesting to use a specific pannexin-1 inhibitor and see if YO-PRO-1 uptake is still blocked. These results suggest a role of ATP in the membrane permeabilisation therefore a better understanding of how ATP levels are affected by nsPEF could help to elucidate the mechanism. To this end, work using U87 cells expressing a fluorescent ATP biosensor is currently being done in our lab. Further work to characterise the effect of a single pulse on other YO-PRO-1 gating channels, such as the TRPs, could also be envisaged. The

post nsPEF permeability is transient and we know from classic electroporation that cells are able to recover from short term poration. However, if nsPEF is affecting membrane channels and receptors then there is the possibility of signal pathway activation which would create further knock-on effects. This type of signalling as a result of nsPEF has been previously reported[72,127].

We used several different fluorescent indicators to show that there is a rapid increase in intracellular calcium following the application of nsPEF and that the source of this calcium is extracellular. To date there is no published work on the use of GECIs in nsPEF research. We showed that they can be useful tools with several advantages over the commonly used chemical indicators. One of the main advantages is being able to have a defined subcellular expression of the indicator. We demonstrated this by visualising a post-nsPEF wave of calcium with a membrane bound GCaMP that was not seen with the cytosolic indicators, including cytosolically expressed GCaMP. The wave had a polar entry similar to that of YO-PRO-1. Confirmation of its presence with a membrane bound chemical indicator confirms that the wave is not just specific to the GECI but is dependent on the tethering of the indicator which prevents the diffusion. We believe that this indicator diffusion masks the wave when using the cytosolic indicators. The wave was present even when intracellular calcium stores had been depleted indicating that the calcium was extracellular. The difference in the calcium wave speed observed with higher frequency pulses, but not with the YO-PRO-1 wave, hint at an increased diffusion of the smaller calcium molecule with increased heat. nsPEF is generally believed to be non-thermal but previous work from our lab has shown that there is indeed cellular heating[244], our work provides some evidence that this heating may augment nsPEF effects on the cell. To confirm this it would be interesting to look at how the nsPEF induced calcium wave speed varies in cells that are heated at a range of different temperatures between the room temperature used for our experiments and 37°C.

Previous nsPEF studies have interpreted the even increase in calcium throughout the cell, as measured with cytosolic chemical indicators, as being due to global nanoporation across the cell or the release of intracellular calcium stores. Our results suggest the possibility that these observations may have been misinterpreted to some extent due to wave masking by indicator diffusion. These published observations were made with different pulse conditions and cell types to those that we have used and it would be interesting to replicate them with the membrane bound GCaMP or FFP-18 in order to see if a wave does occur.

Persistent, elevated levels of intracellular calcium, like those we see following nsPEF, are likely to have an important detrimental effect on the cell. Among these include modulation of gene transcription, phosphorylation or dephosphorylation of proteins altering signalling pathways, mitochondrial failure as a result of metabolic exhaustion from trying to clear calcium ions from the cell and cytoskeletal disruption.

Whilst the work presented in this thesis shows a loss of mitochondrial membrane potential following nsPEF application it does not identify the mechanistic cause. Possible explanations include: nanoporation of the mitochondrial membrane, although the gradual loss of the potential seems to disagree with this hypothesis; the opening of a channel through the mitochondrial membrane, although this is unlikely to be the mPTP; poration by proapoptotic proteins released from the microtubules during depolymerisation. Metabolic exhaustion could also be a candidate, however, it seems unlikely in this case to be linked to increased calcium levels. Experiments with the ATP sensor may help to confirm or discredit this theory.

Whilst our results seem to show that the loss in $\Delta\Psi_m$ is not due to an influx of extracellular sodium they do need to be interpreted with care and ideally supported by further experiments. Choline whilst bigger than sodium is however still small enough to fit through nanopores; the dimensions of choline, as measured from a JMol image of the molecule, are approximately 0.6 x 0.4 x 0.4 nm and nanopores are estimated to be between 0.9 and 1.3 nm[257]. Choline itself could therefore have an impact on the $\Delta\Psi_m$ and confuse the interpretation of results. It could well be that the slight delay in loss of membrane potential (Figure 23) seen with choline, when compared with when sodium was present, reflects choline being bigger and it being harder for it to pass through the membrane. Repeating the experiment using larger cations such as quinine (1.4 x 0.9 x 0.7 nm) or tetrabutylammonium hydroxide (1.2 x 1 x1 nm) that are too big to pass through the pores could help to clear up the role of cations in causing the loss of $\Delta\Psi_m$.

Loss of $\Delta\Psi_m$ is linked to the opening of pores or channels in the mitochondrial membrane with a subsequent release of pro apoptotic molecules combined with a loss of ATP production. These two factors would have an important impact on the cell's viability.

We have shown here, for the first time, that nsPEF causes microtubule depolymerisation and affect microtubule growth dynamics in a calcium and swelling independent fashion. Our EB3 results represent the first time that microtubule dynamics have been looked at following

nsPEF treatment, giving an insight into polymerisation speeds and the number of polymerising microtubules. A more in-depth analysis of the EB3 comets could provide further quantitative information on their dynamics, for example, the number of comets present over time post-nsPEF, any changes in the comets trajectory following the pulse, and differences in trajectory speed pre- and post-pulse. There is a free Matlab package available to do this[258], however my efforts to use this were unsuccessful due to the high signal to noise ratio of EB3 in our widefield imaged cells, leading to poor detection of the comets, and also bugs that occurred when using the package. Efforts to improve the EB3 labelling and the input of someone with more Matlab experience could however overcome these problems.

The 3D-SIM work carried out at the Janelia Research Campus is the first time nsPEF effects have been assessed using super resolution microscopy. Not only did it provide evidence of an alternative reason for the breakdown of the microtubule network, bending and breaking, it also demonstrated that the effects we saw in our lab were reproducible in another lab. Between the two locations, slightly different experimental conditions were used including: different fluorescent markers, slightly modified imaging solution, cells of different passage numbers and lots, and a different model of pulse generator (producing the same pulse shape and intensity). This reproducibility supports the robustness and reliability of our results.

A mass breakdown of the microtubule network is a major event for the cell. Whilst we have shown that it is unlikely to be implicated in the nanoporation and loss of mitochondrial membrane potential that we see, it is likely to have other important downstream effects. Of which could include the release of microtubule sequestered pro-apoptotic proteins. Work to determine if this occurs could be envisaged with a first step being to determine if the nsPEF treated U87 cells actually die and if this death is apoptotic.

Further investigation into the effect of nsPEF on mitosis may also prove interesting to see if cells treated with high pulse numbers really do get blocked in mitosis, as suggested by our work. Cell cycle effects are currently being studied by another student in the lab. The ability to prevent replication by nsPEF, mimicking antimitotic drugs, would be an important discovery for tumour treatment.

This study has therefore shown that the XLIM nsPEF generator and electrode application device were able to reproduce published effects of nsPEF, validating their use for future work. It has also shown that GECIs were suitable for measuring nsPEF effects, providing justification for their use in mouse models for any future *in vivo* work. We have also

demonstrated that glioblastoma cells are sensitive to nsPEF, encouraging the need for *in vivo* follow up studies. We have also identified a pulsing regime (100, 10 ns, 44 kV/cm pulses applied at 10 Hz) that has a reproducible and large effect on all the parameters measured, whether this regime will give the desired anti-tumour effect *in vivo* remains to be seen.

The effect of nsPEF on microtubules will potentially prove to be of importance for glioblastoma treatment. In the brain glioblastoma are connected via microtubule containing membrane microtubes. These microtubes are an important factor in glioblastomas resistance as they allow for intercellular communication and repair, with radiotherapy treated connected cells being protected from death whereas unconnected ones were not[259]. If nsPEF were shown to be able to disrupt this microtube network, by breaking down their microtubules, it could perhaps be used as a pre-treatment to improve the results of radiotherapy.

Whilst the validation process for the use of nsPEF as a treatment for glioblastoma will be long and uncertain, the work in this thesis provides preliminary support to justify giving it a go.

List of publications and communications

Accepted publications:

S.M. Bardet, **L. Carr**, M. Soueid, D. Arnaud-Cormos, P. Leveque and R.P. O'Connor, "Multiphoton imaging reveals that nanosecond pulsed electric fields collapse tumor and normal vascular perfusion in human glioblastoma xenografts". *Sci. Rep.* **6,** 34443 (2016).

M. Soueid, S. Kohler, **L. Carr**, S. M. Bardet, R. P. O'Connor, P. Leveque, and D. Arnaud-Cormos, "Electromagnetic Analysis of an Aperture Modified TEM Cell Including an ITO Layer for Real-Time Observation of Biological Cells Exposed to Microwaves". *Progress In Electromagnetics Research*, **149,** 193-204 (2014).

Submitted publication:

L. Carr, S.M. Bardet, R. Burke, D. Arnaud-Cormos, P. Leveque and R.P. O'Connor, "Calcium-independent disruption of microtubule dynamics by nanosecond pulsed electric fields in U87 human glioblastoma cells". Submitted to: Scientific Reports.

International communications:

L. Carr, S. M. Bardet, M. Soueid, D. Arnaud-Cormos, P. Leveque & R. P. O'Connor, "Super-resolution microscopy reveals microtubule buckling and breaking following nanosecond pulsed electric field exposure in U87 human glioblastoma cells", BioEM2016, Joint Meeting of the BioElectroMagnetics Society and the European BioElectromagnetics Association, Ghent, Belgium, June 2016.

L. Carr, S. M. Bardet, M. Soueid, D. Arnaud-Cormos, P. Leveque & R. P. O'Connor, "Calcium-independent disruption of microtubule growth following nanosecond pulsed electric field exposure in U87 human glioblastoma cells", BioEM2015, Joint Meeting of the BioElectroMagnetics Society and the European BioElectromagnetics Association, Pacific Grove, CA, United States, June 2015.

L. Carr, S. M. Bardet, M. Soueid, D. Arnaud-Cormos, P. Leveque & R. P. O'Connor, "Calcium-independent disruption of microtubule growth following nanosecond pulsed electric field exposure in U87 human glioblastoma cells", Electroporation based Technologies and Treatments Workshop, Ljubljana, Slovenia November 2015

S. M. Bardet, **L. Carr**, M. Soueid, D. Arnaud-Cormos, P. Leveque & R. P. O'Connor, "*In vivo* multiphoton microscopy shows that a single 10 nanosecond pulsed electric field is sufficient to disrupt vasculature in xenografted human glioblastoma ", BioEM2015, Joint Meeting of the BioElectroMagnetics Society and the European BioElectromagnetics Association, June 2015, Pacific Grove, CA, United States.

M. Soueid, N. Ghazie, **L. Carr**, R. P. O'Connor, P. Leveque, and D. Arnaud-Cormos, "nsPEF characterization of a delivery device based on 1-mm Gap thin electrodes for the exposure of biological cells", *The 3rd* IEEE Middle East Conference on Antennas and Propagation MECAP'16, Beirout, Lebanon, September 2016.

National communications:

L. Carr, S. M. Bardet, M. Soueid, D. Arnaud-Cormos, P. Leveque & R. P. O'Connor, "Calcium-independent disruption of microtubule growth following nanosecond pulsed electric field exposure in U87 human glioblastoma cells", 1er Workshop Cancéropôle GSO : Technologies pour la Santé, Toulouse, France, September 2015.

References

1. Cooper, G. in *Cell A Mol. Approach* (Sinauer Associates, 2000). at <http://www.ncbi.nlm.nih.gov/books/NBK9898/>
2. Malhotra, R. Membrane Glycolipids: Functional Heterogeneity: A Review. *Biochem. Anal. Biochem.* **1,** 1–5 (2012).
3. Alberts, B. *et al.* in *Mol. Biol. Cell* (Garland Science, 2002). at <http://www.ncbi.nlm.nih.gov/books/NBK26884/>
4. Lodish, H. *et al.* in *Mol. Cell Biol.* (W. H. Freeman, 2000).
5. Schoenbach, K. H. *et al.* Ultrashort Electrical Pulses Open a New Gateway Into Biological Cells. *Proc. IEEE* **92,** 1112–1137 (2004).
6. Lee, R. C. Cell injury by electric forces. *Ann. N. Y. Acad. Sci.* **1066,** 85–91 (2005).
7. Pucihar, G. *et al.* Measuring the Induced Membrane Voltage with Di-8-ANEPPS. *J. Vis. Exp.* e1659 (2009). doi:10.3791/1659
8. Belehradek, M. *et al.* Electrochemotherapy , a New Antitumor Treatment First Clinical Phase 1-11 Trial. *Cancer* **72,** 3694–3700 (1993).
9. Mir, L. M. *et al.* Bleomycin : Revival of an Old Drug. *Gen. Pharmacol.* **27,** 745–748 (1996).
10. Sersa, G. *et al.* Electrochemotherapy with Cisplatin : Potentiation of Local Cisplatin Antitumour E V ectiveness by Application of Electric Pulses in Cancer Patients. *Eur. J. Cancer* **34,** 1213–1218 (1998).
11. Mir, L. M. *et al.* Standard operating procedures of the electrochemotherapy : Instructions for the use of bleomycin or cisplatin administered either systemically or locally and electric pulses delivered by the Cliniporator TM by means of invasive or non-invasive electrodes. *EJC Suppl.* **4,** 14–25 (2006).
12. Kim, J. *et al.* Electro-gene therapy of collagen-induced arthritis by using an expression plasmid for the soluble p75 tumor necrosis factor receptor-Fc fusion protein. *Gene Ther.* 1216–1224 (2003). doi:10.1038/sj.gt.3301985
13. Forde, P. F. *et al.* Non-viral immune electrogene therapy induces potent antitumour responses and has a curative effect in murine colon adenocarcinoma and melanoma cancer models. *Gene Ther.* **22,** 29–39 (2015).
14. Murakami, T. *et al.* Vascular Endothelial Growth Factor Electro-Gene Therapy Improves Functional Outcome in a Mouse Model of ALS. *Immunol. Endocr. Metab. Agents Med. Chem.* **13,** 107–111 (2013).
15. Daud, A. I. *et al.* Phase I Trial of Interleukin-12 Plasmid Electroporation in Patients With Metastatic Melanoma. *J. Clin. Oncol.* **26,** 5896–5903 (2008).
16. Beebe, S. J. *et al.* Nanosecond pulsed electric fields: a new stimulus to activate intracellular signaling. *J. Biomed. Biotechnol.* **2005,** 297–300 (2005).
17. Beebe, S. J. *et al.* Diverse effects of nanosecond pulsed electric fields on cells and tissues. *DNA Cell Biol.* **22,** 785–96 (2003).
18. Beebe, S. J. *et al.* in *Treat. Metastatic Melanoma* (Morton, M. R.) (InTech, 2011).
19. Nuccitelli, R. *et al.* First-in-human trial of nanoelectroablation therapy for basal cell

carcinoma: Proof of method. *Exp. Dermatol.* **23,** 135–137 (2014).

20. Nuccitelli, R. *et al.* Non-thermal Nanoelectroablation of UV-induced Murine Melanomas Stimulates an Immune Response. *Pigment cell melanoma Res.* **25,** 618–629 (2012).
21. Beebe, S. J. *et al.* Nanosecond pulsed electric field (nsPEF) effects on cells and tissues: apoptosis induction and tumor growth inhibition. *IEEE Trans. Plasma Sci.* **30,** 286–292 (2002).
22. Napotnik, T. B. *et al.* Nanosecond electric pulses cause mitochondrial membrane permeabilization in Jurkat cells. *Bioelectromagnetics* **33,** 257–64 (2012).
23. Vernier, P. T. Mitochondrial membrane permeabilization with nanosecond electric pulses. in *33rd Annu. Int. Conf. IEEE Eng. Med. Biol. Soc.* **2011,** 743–5 (2011).
24. Beebe, S. J. *et al.* Transient features in nanosecond pulsed electric fields differentially modulate mitochondria and viability. *PLoS One* **7,** e51349 (2012).
25. Vernier, P. T. *et al.* Nanoelectropulse-induced phosphatidylserine translocation. *Biophys. J.* **86,** 4040–8 (2004).
26. Beebe, S. J. *et al.* Nanosecond, high-intensity pulsed electric fields induce apoptosis in human cells. *FASEB J.* **17,** 1493–5 (2003).
27. Pakhomova, O. N. *et al.* Two modes of cell death caused by exposure to nanosecond pulsed electric field. *PLoS One* **8,** e70278 (2013).
28. Hall, E. H. *et al.* Nanosecond pulsed electric fields induce apoptosis in p53-wildtype and p53-null HCT116 colon carcinoma cells. *Apoptosis* **12,** 1721–31 (2007).
29. Vernier, P. T. *et al.* Ultrashort pulsed electric fields induce membrane phospholipid translocation and caspase activation: differential sensitivities of Jurkat T lymphoblasts and rat Glioma C6 cells. *IEEE Trans. Dielectr. Electr. Insul.* **10,** 795–809 (2003).
30. Ren, W. *et al.* Nanosecond pulsed electric fields (nsPEFs) activate intrinsic caspase-dependent and caspase-independent cell death in Jurkat cells. *Biochem. Biophys. Res. Commun.* **421,** 808–12 (2012).
31. Semenov, I. *et al.* Primary pathways of intracellular Ca(2+) mobilization by nanosecond pulsed electric field. *Biochim. Biophys. Acta* **1828,** 981–9 (2013).
32. Vernier, P. T. *et al.* Calcium bursts induced by nanosecond electric pulses. *Biochem. Biophys. Res. Commun.* **310,** 286–295 (2003).
33. White, J. A. *et al.* Stimulation of capacitative calcium entry in HL-60 cells by nanosecond pulsed electric fields. *J. Biol. Chem.* **279,** 22964–72 (2004).
34. Weaver, J. C. *et al.* A brief overview of electroporation pulse strength-duration space: a region where additional intracellular effects are expected. *Bioelectrochemistry* **87,** 236–43 (2012).
35. Kohler, S. *et al.* Characterization of a TEM cell-based setup for the exposure of biological cell suspensions to high-intensity nanosecond pulsed electric fields (nsPEFs). *IEE MTT-S Int. Microw. Symp. Dig. (MTT),* 1–3 (2012).
36. Soueid, M. *et al.* Electromagnetic Analysis of an Aperture Modified TEM Cell Including an ITO Layer for Real-Time Observation of Biological Cells Exposed to Microwaves. *Prog. Electromagn. Res.* **149,** 193–204 (2014).
37. Wu, Y.-H. *et al.* Moveable wire electrode microchamber for nanosecond pulsed

electric-field delivery. *IEEE Trans. Biomed. Eng.* **60,** 489–96 (2013).

38. Tang, L. *et al.* Apoptosis induction with electric pulses - a new approach to cancer therapy with drug free. *Biochem. Biophys. Res. Commun.* **390,** 1098–101 (2009).
39. Beebe, S. J. Concepts of Cancer and a Novel Cancer Therapy: Treating Tumors as an Aggressive Organ. *J. Nanomedine. Biotherapeutic Discov.* **04,** 134–136 (2014).
40. Chen, X. *et al.* Long Term Survival of Mice With Hepatocellular Carcinoma after Pulse Power Ablation with Nanosecond Pulsed Electric Fields. *Technol. Cancer Res. Treat.* **11,** 83–93 (2012).
41. Chen, X. *et al.* Apoptosis initiation and angiogenesis inhibition : melanoma targets for nanosecond pulsed electric fields. *Pigment cell melanoma Res.* **23,** 554–563 (2010).
42. Stupp, R. *et al.* Radiotherapy plus Concomitant and Adjuvant Temozolomide for Glioblastoma. *New Engl. J. Med.* **352,** 987–996 (2005).
43. Wilson, T. A. *et al.* Glioblastoma multiforme : State of the art and future therapeutics. *Surg. Neurol. Int.* **5,** 64 (2014).
44. Agerholm-larsen, B. *et al.* Preclinical Validation of Electrochemotherapy as an Effective Treatment for Brain Tumors. *Cancer Res.* **71,** 3753–3762 (2011).
45. Linnert, M. *et al.* Multiple brain metastases - current management and perspectives for treatment with electrochemotherapy. *Radiol. Oncol.* **46,** 271–278 (2012).
46. Batista Napotnik, T. *et al.* Effects of high voltage nanosecond electric pulses on eucaryotic cells (in vitro): A systematic review. *Bioelectrochemistry* **110,** 1–12 (2016).
47. Yin, D. *et al.* Cutaneous papilloma and squamous cell carcinoma therapy utilizing nanosecond pulsed electric fields (nsPEF). *PLoS One* **7,** e43891 (2012).
48. Hu, Q. *et al.* Simulations of Transient Membrane Behavior in Cells Subjected to a High-Intensity Ultrashort Electric Pulse. *Phys. Rev. E* **71,** 031914 (2005).
49. Dehez, F. *et al.* Evidence of Conducting Hydrophobic Nanopores Across Membranes in Response to an Electric Field. *J. Phys. Chem.* **118,** 6752–57 (2014).
50. Vernier, P. T. *et al.* Nanopore Formation and Phosphatidylserine Externalization in a Phospholipid Bilayer at High Transmembrane Potential. *J. Am. Chem. Soc.* **128,** 6288–6289 (2006).
51. Kotnik, T. *et al.* Theoretical Evaluation of Voltage Inducement on Internal Membranes of Biological Cells Exposed to Electric Fields. *Biophys. J.* **90,** 480–491 (2006).
52. Tieleman, D. P. The molecular basis of electroporation. *BMC Biochem.* **5,** 10 (2004).
53. Sridhara, V. *et al.* Numerical study of lipid translocation driven by nanoporation due to multiple high-intensity, ultrashort electrical pulses. *Biochim. Biophys. Acta - Biomembr.* **1838,** 902–909 (2014).
54. Semenov, I. *et al.* Recruitment of the intracellular Ca2+ by ultrashort electric stimuli: the impact of pulse duration. *Cell Calcium* **54,** 145–50 (2013).
55. Bowman, A. M. *et al.* Analysis of plasma membrane integrity by fluorescent detection of Tl(+) uptake. *J. Membr. Biol.* **236,** 15–26 (2010).
56. Pakhomov, A. G. *et al.* in *Adv. Electroporation Tech. Biol. Med.* (Pakhomov, A. G. et al.) 177–194 (CRC Press, 2010).
57. Pakhomov, A. G. *et al.* Multiple nanosecond electric pulses increase the number but not the size of long-lived nanopores in the cell membrane. *Biochim. Biophys. Acta*

1848, 958–66 (2015).

58. Ibey, B. L. *et al.* Bipolar nanosecond electric pulses are less efficient at electropermeabilization and killing cells than monopolar pulses. *Biochem. Biophys. Res. Commun.* **443,** 568–73 (2014).

59. Virginio, C. *et al.* Kinetics of cell lysis , dye uptake and permeability changes in cells expressing the rat P2X7 receptor. *J. Physiol.* **519,** 335–346 (1999).

60. André, F. M. *et al.* Gadolinium blocks membrane permeabilization induced by nanosecond electric pulses and reduces cell death. *Bioelectrochemistry* **79,** 95–100 (2010).

61. Ledur, P. F. *et al.* Extracellular ATP reduces tumor sphere growth and cancer stem cell population in glioblastoma cells. *Purigenic Signal.* **8,** 39–48 (2012).

62. Lohman, A. W. *et al.* Differentiating connexin hemichannels and pannexin channels in cellular ATP release. *FEBS Lett.* **588,** 1379–1388 (2014).

63. Bhaskaracharya, A. *et al.* Probenecid blocks human P2X7 receptor-induced dye uptake via a pannexin-1 independent mechanism. *PLoS One* **9,** e93058 (2014).

64. Pelegrin, P. *et al.* Pannexin-1 mediates large pore formation and interleukin-1b release by the ATP-gated P2X7 receptor. *EMBO J.* **25,** 5071–5082 (2006).

65. Pelegrin, P. *et al.* The P2X 7 receptor – pannexin connection to dye uptake and IL-1 β release. *Purigenic Signal.* **5,** 129–137 (2009).

66. Mackenzie, A. B. *et al.* Pseudoapoptosis induced by brief activation of ATP-gated P2X7 receptors. *J. Biol. Chem.* **280,** 33968–76 (2005).

67. Niemeyer, B. A. Structure-function analysis of TRPV channels. *Naunyn. Schmiedebergs. Arch. Pharmacol.* **371,** 285–94 (2005).

68. Chung, M. *et al.* TRPV1 shows dynamic ionic selectivity during agonist stimulation. *Nat. Neurosci.* **11,** 555–564 (2008).

69. Banke, T. G. *et al.* Dynamic changes in the TRPA1 selectivity filter lead to progressive but reversible pore dilation. *Am. J. cell Physiol.* **298,** 1457–1468 (2010).

70. Chen, J. *et al.* Pore dilation occurs in TRPA1 but not in TRPM8 channels. *Mol. Pain* **5,** 2–7 (2009).

71. Nilius, B. *et al.* The transient receptor potential family of ion channels. *Genome Biol.* **12,** 218 (2011).

72. Tolstykh, G. P. *et al.* 600Ns Pulse Electric Field-Induced Phosphatidylinositol4,5-Bisphosphate Depletion. *Bioelectrochemistry* **100,** 80–87 (2014).

73. Goswami, C. *et al.* Rapid disassembly of dynamic microtubules upon activation of the capsaicin receptor TRPV1. *J. Neurochem.* **96,** 254–66 (2006).

74. Gowrishankar, T. R. *et al.* Electrical behavior and pore accumulation in a multicellular model for conventional and supra-electroporation. *Biochem. Biophys. Res. Commun.* **349,** 643–653 (2006).

75. Smith, K. C. *et al.* Active Mechanisms Are Needed to Describe Cell Responses to Submicrosecond , Megavolt-per-Meter Pulses : Cell Models for Ultrashort Pulses. *Biophys. J.* **95,** 1547–1563 (2008).

76. Tekle, E. *et al.* Selective Field Effects on Intracellular Vacuoles and Vesicle Membranes with Nanosecond Electric Pulses. *Biophys. J.* **89,** 274–284 (2005).

77. Buescher, E. S. *et al.* Effects of Submicrosecond , High Intensity Pulsed Electric Fields on Living Cells . Intracellular Electromanipulation. *IEEE Trans. Dielectr. Electr. Insul.* **10,** 788–794 (2003).

78. Schoenbach, K. H. *et al.* Intracellular Effect of Ultrashort Electrical Pulses. *Bioelectromagnetics* **22,** 440–448 (2001).

79. Roderick, H. L. *et al.* Calcium-induced calcium release. *Curr. Biol.* **13,** R425 (2003).

80. Winslow, R. L. *et al.* Extinguishing the sparks. *Biophys. J.* **104,** 2115–7 (2013).

81. Ren, W. *et al.* An apoptosis targeted stimulus with nanosecond pulsed electric fields (nsPEFs) in E4 squamous cell carcinoma. *Apoptosis* **16,** 382–93 (2011).

82. Morotomi-Yano, K. *et al.* Nanosecond pulsed electric fields activate AMP-activated protein kinase: implications for calcium-mediated activation of cellular signaling. *Biochem. Biophys. Res. Commun.* **428,** 371–5 (2012).

83. Ford, W. E. *et al.* Nanosecond pulsed electric fields stimulate apoptosis without release of pro-apoptotic factors from mitochondria in B16f10 melanoma. *Arch. Biochem. Biophys.* **497,** 82–9 (2010).

84. Kenaan, M. *et al.* Characterization of a 50- Ω Exposure Setup for High-Voltage Nanosecond Pulsed Electric Field Bioexperiments. *IEEE Trans. Biomed. Eng.* **58,** 207–214 (2011).

85. Kohler, S. *et al.* Experimental Microdosimetry Techniques for Biological Cells Exposed to Nanosecond Pulsed Electric Fields Using Micro fl uorimetry. *IEE Trans. Microw. Theory Tech.* **61,** 2015–2022 (2015).

86. Kohler, S. *et al.* Simultaneous High Intensity Ultrashort Pulsed Electric Field and Temperature Measurements Using a Unique Electro-Optic Probe. *IEE Microwaves Wirel. Components Lett.* **22,** 153–155 (2012).

87. Thomas, D. *et al.* A comparison of fluorescent Ca2+ indicator properties and their use in measuring elementary and global Ca2+ signals. *Cell Calcium* **28,** 213–23 (2000).

88. Knight, M. M. *et al.* Live cell imaging using confocal microscopy induces intracellular calcium transients and cell death. *Am. J. Physiol. Cell Physiol.* **284,** C1083–9 (2003).

89. Lohr, C. Monitoring neuronal calcium signalling using a new method for ratiometric confocal calcium imaging. *Cell Calcium* **34,** 295–303 (2003).

90. Wong, R. *et al.* Mitochondrial permeability transition pore and calcium handling. *Methods Mol. Biol.* **810,** 235–242 (2012).

91. Garcia-Marcos, M. *et al.* Role of sodium in mitochondrial membrane depolarization induced by P2X7 receptor activation in submandibular glands. *FEBS Lett.* **579,** 5407–13 (2005).

92. Li, J. *et al.* The effect of extracellular conductivity on electroporation-mediated molecular delivery. *Biochim. Biophys. Acta* **1828,** 461–70 (2013).

93. Vernier, P. T. *et al.* Nanoelectropulse-driven membrane perturbation and small molecule permeabilization. *BMC Cell Biol.* **7,** 37 (2006).

94. Ma, W. *et al.* Pharmacological Characterization of Pannexin-1 Currents Expressed in Mammalian Cells □. *J. Pharmacol. Exp. Ther.* **328,** 409–418 (2009).

95. Nelson, D. W. *et al.* Structure - Activity Relationship Studies on a Series of Novel , Substituted 1-Benzyl-5-phenyltetrazole P2X 7 Antagonists. *J. Med. Chem.* **49,** 3659–

3666 (2006).

96. Beier, H. T. *et al.* Resolving the spatial kinetics of electric pulse-induced ion release. *Biochem. Biophys. Res. Commun.* **423,** 863–6 (2012).

97. Beebe, S. J. Considering effects of nanosecond pulsed electric fields on proteins. *Bioelectrochemistry* **103,** 52–9 (2015).

98. Kim, T. *et al.* Active alignment of microtubules with electric fields. *Nano Lett.* **7,** 211–7 (2007).

99. Ramalho, R. R. *et al.* Microtubule behavior under strong electromagnetic fields. *Mater. Sci. Eng. C* **27,** 1207–1210 (2007).

100. Kirson, E. D. *et al.* Disruption of Cancer Cell Replication by Alternating Electric Fields. *Cancer Res.* **64,** 3288–3295 (2004).

101. Havelka, D. *et al.* Electro-acoustic behavior of the mitotic spindle: a semi-classical coarse-grained model. *PLoS One* **9,** e86501 (2014).

102. Etienne-Manneville, S. From signaling pathways to microtubule dynamics: the key players. *Curr. Opin. Cell Biol.* **22,** 104–11 (2010).

103. Moss, D. K. *et al.* Microtubules: forgotten players in the apoptotic execution phase. *Trends Cell Biol.* **16,** 330–8 (2006).

104. Feit, H. *et al.* Heterogeneity of Tubulin Subunits. *Proc. Natl. Acad. Sci. U. S. A.* **68,** 2028–2031 (1971).

105. Nogales, E. Structural insights into microtubule function. *Annu. Rev. Biochem.* **69,** 277–302 (2000).

106. Conde, C. *et al.* Microtubule assembly, organization and dynamics in axons and dendrites. *Nat. Rev. Neurosci.* **10,** 319–32 (2009).

107. Jordan, M. A. *et al.* Microtubules as a target for anticancer drugs. *Nat. Rev. Cancer* **4,** 253–265 (2004).

108. Amos, L. A. *et al.* Microtubules and maps. *Adv. Protein Chem.* **71,** 257–98 (2005).

109. van der Vaart, B. *et al.* Regulation of microtubule dynamic instability. *Biochem. Soc. Trans.* **37,** 1007–13 (2009).

110. Roll-Mecak, A. *et al.* Microtubule-severing enzymes. *Curr. Opin. Cell Biol.* **22,** 96–103 (2010).

111. Duellberg, C. *et al.* The size of the EB cap determines instantaneous microtubule stability. *Elife* **5,** e13470 (2016).

112. Mills, J. C. *et al.* Activation of a PP2A-like phosphatase and dephosphorylation of tau protein characterize onset of the execution phase of apoptosis. *J. Cell Sci.* **111 (Pt 5,** 625–36 (1998).

113. Moss, D. K. *et al.* A novel role for microtubules in apoptotic chromatin dynamics and cellular fragmentation. *J. Cell Sci.* **119,** 2362–74 (2006).

114. Deng, X. *et al.* Protein phosphatase 2A inactivates Bcl2 ' s antiapoptotic function by dephosphorylation and up-regulation of Bcl2-p53 binding. *Blood* **113,** 422–428 (2009).

115. Puthalakath, H. *et al.* Keeping killers on a tight leash: transcriptional and post-translational control of the pro-apoptotic activity of BH3-only proteins. *Cell Death Differ.* **9,** 505–12 (2002).

116. Bender, T. *et al.* Where killers meet--permeabilization of the outer mitochondrial membrane during apoptosis. *Cold Spring Harb. Perspect. Biol.* **5,** a011106 (2013).

117. Stacey, M. *et al.* Nanosecond pulsed electric field induced cytoskeleton, nuclear membrane and telomere damage adversely impact cell survival. *Bioelectrochemistry* **82,** 131–4 (2011).

118. Böhm, K. J. *et al.* Movement and Alignment of Microtubules in Electric Fields and Electric-Dipole-Moment Estimates. *Electromagn. Biol. Med.* **24,** 319–330 (2005).

119. Stracke, R. *et al.* Analysis of the migration behaviour of single microtubules in electric fields. *Biochem. Biophys. Res. Commun.* **293,** 602–609 (2002).

120. Kanthou, C. *et al.* The endothelial cytoskeleton as a target of electroporation-based therapies. *Mol. Cancer Ther.* **5,** 3145–52 (2006).

121. Kühn, S. *et al.* Nanosecond electric pulses affect a plant-specific kinesin at the plasma membrane. *J. Membr. Biol.* **246,** 927–38 (2013).

122. Thompson, G. L. *et al.* Calcium influx affects intracellular transport and membrane repair following nanosecond pulsed electric field exposure. *J. Biomed. Opt.* **19,** 055005 (2014).

123. Dhonukshe, P. *et al.* Phospholipase D Activation Correlates with Microtubule Reorganization in Living Plant Cells. *Plant Cell* **15,** 2666–2679 (2003).

124. Popova, J. S. *et al.* Muscarinic receptor activation promotes the membrane association of tubulin for the regulation of Gq-mediated phospholipase Cbeta(1) signaling. *J. Neurosci.* **20,** 2774–82 (2000).

125. Chae, Y. C. *et al.* Inhibition of muscarinic receptor-linked phospholipase D activation by association with tubulin. *J. Biol. Chem.* **280,** 3723–30 (2005).

126. Roychowdhury, S. *et al.* G Protein Subunits Activate Tubulin GTPase and Modulate Microtubule Polymerization Dynamics. *J. Biol. Chem.* **274,** 13485–13490 (1999).

127. Tolstykh, G. P. *et al.* Activation of intracellular phosphoinositide signaling after a single 600 nanosecond electric pulse. *Bioelectrochemistry* **94,** 23–9 (2013).

128. Zeghimi, A. *et al.* Involvement of cytoskeleton in sonoporation and drug delivery. in *2014 IEEE Int. Ultrason. Symp. Proc.* 850–853 (2014).

129. Kilinc, D. *et al.* Mechanically-induced membrane poration causes axonal beading and localized cytoskeletal damage. *Exp. Neurol.* **212,** 422–30 (2008).

130. Teissie, J. *et al.* Manipulation of Cell Cytoskeleton Affects the Lifetime of Cell Membrane Electropermeabilization. *Ann. N. Y. Acad. Sci.* **720,** 98–110 (1994).

131. Goswami, C. *et al.* Novel aspects of the submembraneous microtubule cytoskeleton. *FEBS J.* **275,** 4653 (2008).

132. Chen, X.-Z. *et al.* Submembraneous microtubule cytoskeleton: interaction of TRPP2 with the cell cytoskeleton. *FEBS J.* **275,** 4675–83 (2008).

133. Sellin, M. E. *et al.* Microtubules support a disk-like septin arrangement at the plasma membrane of mammalian cells. *Mol. Biol. Cell* **22,** 4588–601 (2011).

134. Wolff, J. Plasma membrane tubulin. *Biochim. Biophys. Acta* **1788,** 1415–33 (2009).

135. Mironov, S. L. *et al.* [Ca2+]i signaling between mitochondria and endoplasmic reticulum in neurons is regulated by microtubules. From mitochondrial permeability transition pore to Ca2+-induced Ca2+ release. *J. Biol. Chem.* **280,** 715–21 (2005).

136. Smyth, J. T. *et al.* Activation and Regulation of Store-operated Calcium Entry. *J. Cell. Mol. Med.* **14,** 2337–2349 (2010).

137. Bannai, H. *et al.* Kinesin dependent, rapid, bi-directional transport of ER sub-compartment in dendrites of hippocampal neurons. *J. Cell Sci.* **117,** 163–75 (2004).

138. Baba, Y. *et al.* Coupling of STIM1 to store-operated Ca 2 + entry through its constitutive and inducible movement in the endoplasmic reticulum. *PNAS* **103,** 1–6 (2006).

139. Smyth, J. T. *et al.* Role of the microtubule cytoskeleton in the function of the store-operated Ca2+ channel activator STIM1. *J. Cell Sci.* **120,** 3762–71 (2007).

140. Scrideli, C. a *et al.* Gene expression profile analysis of primary glioblastomas and non-neoplastic brain tissue: identification of potential target genes by oligonucleotide microarray and real-time quantitative PCR. *J. Neurooncol.* **88,** 281–91 (2008).

141. Brien, E. T. O. *et al.* How Calcium Causes Microtubule Depolymerization. *Cell Motil. Cytoskeleton* **36,** 125–135 (1997).

142. Billger, M. *et al.* Proteolysis of tubulin and microtubule-associated proteins 1 and 2 by calpain I and II . Difference in sensitivity of assembled and disassembled micro-tubules. 33–44 (1988).

143. Maldonado, E. N. *et al.* Free tubulin modulates mitochondrial membrane potential in cancer cells. *Cancer Res.* **70,** 10192–201 (2010).

144. Gurnev, P. a *et al.* Tubulin-blocked state of VDAC studied by polymer and ATP partitioning. *FEBS Lett.* **585,** 2363–6 (2011).

145. Rostovtseva, T. K. *et al.* VDAC regulation: role of cytosolic proteins and mitochondrial lipids. *J. Bioenerg. Biomembr.* **40,** 163–70 (2008).

146. Rostovtseva, T. K. *et al.* VDAC inhibition by tubulin and its physiological implications. *Biochim. Biophys. Acta* **1818,** 1526–35 (2012).

147. Lansbergen, G. *et al.* Microtubule plus end: a hub of cellular activities. *Traffic* **7,** 499–507 (2006).

148. Akhmanova, A. *et al.* Control of microtubule organization and dynamics: two ends in the limelight. *Nat. Rev. Mol. Cell Biol.* **16,** 711–26 (2015).

149. Stepanova, T. *et al.* Visualization of Microtubule Growth in Cultured Neurons via the Use of EB3-GFP (End-Binding Protein 3-Green Fluorescent Protein). **23,** 2655–2664 (2003).

150. Bieling, P. *et al.* Reconstitution of a microtubule plus-end tracking system in vitro. *Nature* **450,** 1100–5 (2007).

151. Akhmanova, A. *et al.* Tracking the ends: a dynamic protein network controls the fate of microtubule tips. *Nat. Rev. Mol. Cell Biol.* **9,** 309–22 (2008).

152. Hayashi, I. *et al.* Crystal structure of the amino-terminal microtubule-binding domain of end-binding protein 1 (EB1). *J. Biol. Chem.* **278,** 36430–4 (2003).

153. Zanic, M. *et al.* EB1 recognizes the nucleotide state of tubulin in the microtubule lattice. *PLoS One* **4,** e7585 (2009).

154. Seetapun, D. *et al.* Estimating the microtubule GTP cap size in vivo. *Curr. Biol.* **22,** 1681–7 (2012).

155. Maurer, S. P. *et al.* EBs recognize a nucleotide-dependent structural cap at growing

microtubule ends. *Cell* **149,** 371–82 (2012).

156. Semenova, I. *et al.* in *Microtubule Protcols* (Zhou, J.) **137,** 93–102 (Humana Press, 2007).

157. Shelden, E. *et al.* Observation and Quantification of Individual Microtubule Behavior In Vivo: Microtubule Dynamics Are Cell-Type Specific. *J. Cell Biol.* **120,** 935–945 (1993).

158. Vasquez, R. J. *et al.* Nanornolar Concentrations of Nocodazole Alter Microtubule Dynamic Instability In Vivo and In Vitro. **8,** 973–985 (1997).

159. Goodson, H. V *et al.* Methods for Expressing and Analyzing GFP-Tubulin and GFP-Microtubule-Associated Proteins. *Cold Spring Harb. Protoc.* 1–16 (2010). doi:10.1101/pdb.top85

160. Super-Resolution Tutorial. *Adv. Microsc.* (2016). at <http://advanced-microscopy.utah.edu/education/super-res/>

161. Macdonald, L. *et al.* in *Membr. Traffick. Methods Mol. Biol.* (Tang LB) **1270,** 255–275 (Springer Science and Business, 2015).

162. Gustafsson, M. G. L. *et al.* Three-dimensional resolution doubling in wide-field fluorescence microscopy by structured illumination. *Biophys. J.* **94,** 4957–70 (2008).

163. Shao, L. *et al.* Super-resolution 3D microscopy of live whole cells using structured illumination. *Nat. Methods* **8,** 1044–1046 (2011).

164. Gustafsson, M. G. L. Nonlinear structured-illumination microscopy : Wide-field fluorescence imaging with theoretically unlimited resolution. *Proc. Natl. Acad. Sci. U. S. A.* **102,** 13081–13086 (2005).

165. Stanton, R. *et al.* Drugs that target dynamic microtubules: A new molecular prospective. *Med. Res. Rev.* **31,** 443–481 (2012).

166. Pradhan, K. *et al.* Effect of addition of 'carrier' DNA during transient protein expression in suspension CHO culture. *Cytotechnology* **64,** 613–22 (2012).

167. Fiolka, R. *et al.* Time-lapse two-color 3D imaging of live cells with doubled resolution using structured illumination. *Proc. Natl. Acad. Sci. U. S. A.* **109,** 5311–5 (2012).

168. Shaner, N. C. *et al.* A bright monomeric green fluorescent protein derived from Branchiostoma lanceolatum. *Nat. Methods* **10,** 407–9 (2013).

169. Pakhomov, A. G. *et al.* Disassembly of actin structures by nanosecond pulsed electric field is a downstream effect of cell swelling. *Bioelectrochemistry* **100,** 88–95 (2014).

170. Silve, A. *et al.* Impact of external medium conductivity on cell membrane electropermeabilization by microsecond and nanosecond electric pulses. *Sci. Rep.* **6,** 19957 (2016).

171. Liu, X. *et al.* Altered fusion dynamics underlie unique morphological changes in mitochondria during hypoxia-reoxygenation stress. *Cell Death Differ.* **18,** 1561–72 (2011).

172. Crompton, M. *et al.* Evidence for the presence of a reversible Ca2+-dependent pore activated by oxidative stress in heart mitochondria. *Biochem. J.* **245,** 915–918 (1987).

173. Halestrap, A. P. *et al.* Inhibition of Ca2 + -induced large-amplitude swelling of liver and heart mitochondria by cyclosporin is probably caused by the inhibitor binding to mitochondrial-matrix peptidyl-prolyl cis-trans isomerase and preventing it interacting

with the adenine nuc. *Biochem. J.* **268,** 153–160 (1990).

174. Jensen, B. *et al.* Osmotic stress induces rapid cytoskeletal reorganization in human retinal pigment epithelial cells in a manner dependent on the microtubule plus end tracking proteins EB1 and EB3. *Acta Physiol.* **198,** (2010).

175. Sellin, M. E. *et al.* Global Regulation of the Interphase Microtubule System by Abundantly Expressed Op18 / Stathmin. **19,** 2897–2906 (2008).

176. Gigant, B. *et al.* The 4 A X-Ray Structure of a Tubulin : Stathmin-like domain complex. *Cell* **102,** 809–816 (2000).

177. Parker, A. L. *et al.* Microtubules and their role in cellular stress in cancer. *Front. Oncol.* **4,** 153 (2014).

178. Sharma, J. *et al.* Use of N , N ’. Polymethylenebis (lodoacetamide) Derivatives as Probes for the Detection of Conformational Differences in Tubulin Isotypes. *J. Protein Chem.* **13,** 165–176 (1994).

179. Schulze, E. *et al.* Posttranslational Modification and Microtubule Stability. *J. Cell Biol.* **105,** 2167–2177 (1987).

180. Togo, T. Disruption of the plasma membrane stimulates rearrangement of microtubules and lipid traffic toward the wound site. *J. Cell Sci.* **119,** 2780–6 (2006).

181. Larsen, T. H. *et al.* Cytoskeletal involvement during hypo-osmotic swelling and volume regulation in cultured chick cardiac myocytes. *Histochem Cell Biol.* **113,** 479–488 (2000).

182. Rassokhin, M. A. *et al.* Cellular Regulation of Extension and Retraction of Pseudopod-Like Blebs Produced by Nanosecond Pulsed Electric Field (nsPEF). *Cell Biochem. Biophys.* (2014). doi:10.1007/s12013-014-9831-9

183. Sozer, E. B. *et al.* Nanometer-Scale Permeabilization and Osmotic Swelling Induced by 5-ns Pulsed Electric Fields. *J. Membr. Biol.* Advance online publication. DOI: 10.1007/s00232–01 (2016). doi:10.1007/s00232-016-9918-x

184. Watkins, S. *et al.* Hydrodynamic Cellular Volume Changes Enable Glioma Cell Invasion. *J. Neurosci.* **31,** 17250–17259 (2011).

185. Cuddapah, V. A. *et al.* A neurocentric perspective on glioma invasion. *Nat. Rev. Neurosci.* **15,** 455–65 (2014).

186. Montana, V. *et al.* Bradykinin promotes the chemotactic invasion of primary brain tumors. *J. Neurosci.* **31,** 4858–67 (2011).

187. Kang, S. S. *et al.* Caffeine-mediated inhibition of calcium release channel inositol 1,4,5-trisphosphate receptor subtype 3 blocks glioblastoma invasion and extends survival. *Cancer Res.* **70,** 1173–1183 (2010).

188. Brangwynne, C. P. *et al.* Force fluctuations and polymerization dynamics of intracellular microtubules. *Proc. Natl. Acad. Sci. U. S. A.* **104,** 16128–16133 (2007).

189. Shekhar, N. *et al.* Fluctuating motor forces bend growing microtubules. *Cell. Mol. Bioeng.* **6,** 120–129 (2013).

190. Odde, D. J. *et al.* Microtubule bending and breaking in living fibroblast cells. *J. Cell Sci.* **112 (Pt 1,** 3283–8 (1999).

191. Brangwynne, C. P. *et al.* Microtubules can bear enhanced compressive loads in living cells because of lateral reinforcement. *J. Cell Biol.* **173,** 733–741 (2006).

192. Wu, J. *et al.* Effects of dynein on microtubule mechanics and centrosome positioning. *Mol. Biol. Cell* **22,** 4834–41 (2011).

193. Minoura, I. *et al.* Dielectric measurement of individual microtubules using the electroorientation method. *Biophys. J.* **90,** 3739–48 (2006).

194. Umnov, M. *et al.* Experimental evaluation of electrical conductivity of microtubules. *J. Mater. Sci.* **42,** 373–378 (2006).

195. Cifra, M. *et al.* Electric field generated by axial longitudinal vibration modes of microtubule. *Biosystems.* **100,** 122–31 (2010).

196. Tang-Schomer, M. D. *et al.* Mechanical breaking of microtubules in axons during dynamic stretch injury underlies delayed elasticity, microtubule disassembly, and axon degeneration. *FASEB J.* **24,** 1401–10 (2010).

197. Waterman-storer, C. M. *et al.* Actomyosin-based Retrograde Flow of Microtubules in the Lamella of Migrating Epithelial Cells Influences Microtubule Dynamic Instability and Turnover and Is Associated with Microtubule Breakage and Treadmilling. **139,** 417–434 (1997).

198. Pizzo, P. *et al.* Mitochondria-endoplasmic reticulum choreography: structure and signaling dynamics. *Trends Cell Biol.* **17,** 511–7 (2007).

199. Morris, R. L. *et al.* Axonal Transport of Mitochondria along Microtubules and F-Actin in Living Vertebrate Neurons. *J. Cell Biol.* **131,** 1315–1326 (1995).

200. Maldonado, E. N. *et al.* Voltage-dependent anion channels modulate mitochondrial metabolism in cancer cells: regulation by free tubulin and erastin. *J. Biol. Chem.* **288,** 11920–9 (2013).

201. Rovini, A. *et al.* Microtubule-targeted agents: when mitochondria become essential to chemotherapy. *Biochim. Biophys. Acta* **1807,** 679–88 (2011).

202. Tong, T. *et al.* Gadd45a Expression Induces Bim Dissociation from the Cytoskeleton and Translocation to Mitochondria. *Mol. Cell. Biol.* **25,** 4488–4500 (2005).

203. Puthalakath, H. *et al.* The Proapoptotic Activity of the Bcl-2 Family Member Bim Is Regulated by Interaction with the Dynein Motor Complex. *Mol. Cell* **3,** 287–296 (1999).

204. Tait, S. W. G. *et al.* Mitochondria and cell death: outer membrane permeabilization and beyond. *Nat. Rev. Mol. Cell Biol.* **11,** 621–32 (2010).

205. Li, H. *et al.* Activity-dependent targeting of TRPV1 with a pore-permeating capsaicin analog. *Proc. Natl. Acad. Sci. U. S. A.* **108,** 8497–502 (2011).

206. Goswami, C. *et al.* Submembraneous microtubule cytoskeleton: biochemical and functional interplay of TRP channels with the cytoskeleton. *FEBS J.* **275,** 4684–99 (2008).

207. Webster, D. R. *et al.* Differential turnover of tyrosinated and detyrosinated microtubules. *Proc. Natl. Acad. Sci. U. S. A.* **84,** 9040–9044 (1987).

208. Palazzo, A. F. *et al.* mDia mediates Rho-regulated formation and orientation of stable microtubules. *Nat. Cell Biol.* **3,** 723–729 (2001).

209. Schulze, E. *et al.* Microtubule Dynamics in Interphase Cells. *J. Cell Biol.* **102,** 1020–1031 (1986).

210. Katsetos, C. *et al.* Altered Cellular Distribution and Subcellular Sorting of gamma -

Tubulin in Diffuse Astrocytic Gliomas and Human Glioblastoma Cell Lines. *J. Neuropathol. Exp. Neurol.* **65,** 465–477 (2006).

211. Shu, H. *et al.* Gamma-Tubulin Can Both Nucleate Microtubule Assembly and Self-assemble into Novel Tubular Structures in Mammalian Cells. **130,** 1137–1147 (1995).
212. Zhai, Y. *et al.* Microtubule Dynamics at the G2 / M Transition : Abrupt Breakdown of Cytoplasmic Microtubules at Nuclear Envelope Breakdown and Implications for Spindle Morphogenesis. **135,** 201–214 (1996).
213. Thompson, G. L. *et al.* Permeabilization of the nuclear envelope following nanosecond pulsed electric field exposure. *Biochem. Biophys. Res. Commun.* **470,** 35–40 (2016).
214. Bree, J. W. M. Van *et al.* Novel Nanosecond Pulsed Electric Field Device for Noncontact Treatment of Cells in Native Culture Conditions. **41,** 2654–2658 (2013).
215. Berridge, M. J. *et al.* The versatility and universality of calcium signalling. *Nat. Rev. Mol. Cell Biol.* **1,** 11–21 (2000).
216. Bootman, M. D. *et al.* in *Enclyopedia Life Sci.* 1–7 (2001).
217. Berridge, M. J. *et al.* Calcium – a life and death signal. *Nature* **395,** 645–648 (1998).
218. Kraus, A. *et al.* in *Calcium A matter life or death* 199–218 (2007). doi:10.1016/S0167-7306(06)41008-5
219. Bootman, M. D. *et al.* in *Encylopedia Life Sci.* 1–9 (2006). doi:10.1038/npg.els.0003957
220. Marchi, S. *et al.* Alterations of calcium homeostasis in cancer cells. *Curr. Opin. Pharmacol.* **29,** 1–6 (2016).
221. Schwaller, B. Cytosolic Ca2+ Buffers. *Cold Spring Harb. Perspect. Biol.* **2,** a004051 (2010).
222. Berridge, M. J. Calcium signalling remodelling and disease. *Biochem. Soc. Trans.* **40,** 297–309 (2012).
223. Monteith, G. R. *et al.* Calcium Channels and Pumps in Cancer : Changes and Consequences. *J. Biol. Chem.* **287,** 31666–31673 (2012).
224. Shimomura, O. *et al.* Extraction , Purification and Properties of Aequorin , a Bioluminescent Protein from the Luminous. *J. Cell. Comp. Physiol.* **59,** 223–239 (1962).
225. Blinks, B. J. R. *et al.* Practical Aspects of the Use of Aequorin as a Calcium Indicator : Assay , Preparation , Microinjection , and Interpretation of Signals. *Methods Enzymol.* **57,** 292–328 (1978).
226. Grynkiewicz, G. *et al.* A New Generation of Ca2 + Indicators with Greatly Improved Fluorescence Properties *. *J. Biol. Chem.* **260,** 3440–3450 (1985).
227. Tsien, R. Y. *et al.* T-cell mitogens cause early changes in cytoplasmic free Ca2+ and membrane potential in lymphocytes. *Nature* **295,** 68–71 (1982).
228. Tsien, R. Y. A non-disruptive technique for loading calcium buffers and indicators into cells. *Nature* **290,** 527–528 (1981).
229. Paredes, R. M. *et al.* Chemical calcium indicators. *Methods* **46,** 143–51 (2008).
230. Etter, E. F. *et al.* Near-membrane [Ca2+] transients resolved using the Ca2+ indicator FFP18. *Proc. Natl. Acad. Sci. U. S. A.* **93,** 5368–5373 (1996).

231. Wang, Z. *et al.* Impact of Cytoplasmic Calcium Buffering on the Spatial and Temporal Characteristics of Intercellular Calcium Signals in Astrocytes. *J. Neurosci.* **17,** 7359–7371 (1997).

232. Koldenkova, V. P. *et al.* Genetically encoded Ca(2+) indicators: properties and evaluation. *Biochim. Biophys. Acta* **1833,** 1787–97 (2013).

233. Nakai, J. *et al.* A high signal-to-noise Ca(2+) probe composed of a single green fluorescent protein. *Nat. Biotechnol.* **19,** 137–41 (2001).

234. Tian, L. *et al.* Imaging neural activity in worms, flies and mice with improved GCaMP calcium indicators. *Nat. Methods* **6,** 875–881 (2009).

235. Akerboom, J. *et al.* Optimization of a GCaMP calcium indicator for neural activity imaging. *J. Neurosci.* **32,** 13819–40 (2012).

236. Akerboom, J. *et al.* Crystal structures of the GCaMP calcium sensor reveal the mechanism of fluorescence signal change and aid rational design. *J. Biol. Chem.* **284,** 6455–6464 (2009).

237. Hou, J. H. *et al.* Simultaneous mapping of membrane voltage and calcium in zebrafish heart in vivo reveals chamber-specific developmental transitions in ionic currents. *Front. Physiol.* **5,** 344 (2014).

238. Scarlett, S. S. *et al.* Regulation of intracellular calcium concentration by nanosecond pulsed electric fields. *Biochim. Biophys. Acta* **1788,** 1168–75 (2009).

239. Beebe, S. *et al.* Induction of Cell Death Mechanisms and Apoptosis by Nanosecond Pulsed Electric Fields (nsPEFs). *Cells* **2,** 136–162 (2013).

240. Roth, C. C. *et al.* Nanosecond pulsed electric field thresholds for nanopore formation in neural cells. *J. Biomed. Opt.* **18,** 035005 (2013).

241. Vernier, P. T. *et al.* Nanosecond electric pulse-induced calcium entry into chromaffin cells. *Bioelectrochemistry* **73,** 1–4 (2008).

242. Craviso, G. L. *et al.* Modulation of intracellular Ca2+ levels in chromaffin cells by nanoelectropulses. *Bioelectrochemistry* **87,** 244–252 (2012).

243. Oliver, A. E. *et al.* Effects of temperature on calcium-sensitive fluorescent probes. *Biophys. J.* **78,** 2116–2126 (2000).

244. Moreau, D. *et al.* Rhodamine B as an optical thermometer in cells focally exposed to infrared laser light or nanosecond pulsed electric fields. *Biomed. Opt. Express* **6,** 4105–17 (2015).

245. Tsai, J.-C. *et al.* Are buffers boring? Uniqueness and asymptotical stability of traveling wave fronts in the buffered bistable system. *J. Math. Biol.* **54,** 513–53 (2007).

246. Nuccitelli, R. *et al.* The Sperm-Induced Ca2+ Wave Following Fertilization of the Xenopus Egg Requires the Production of Ins(1,4,5)P3. *Dev. Biol.* **158,** 200–212 (1993).

247. Chen, T.-W. *et al.* Ultrasensitive fluorescent proteins for imaging neuronal activity. *Nature* **499,** 295–300 (2013).

248. Han, R. *et al.* Measurement of sub-membrane [Ca2+] in adult myofibers and cytosolic [Ca2+] in myotubes from normal and mdx mice using the Ca2+ indicator FFP-18. *Cell Calcium* **40,** 299–307 (2006).

249. Oheim, M. *et al.* New red-fluorescent calcium indicators for optogenetics, photoactivation and multi-color imaging. *Biochim. Biophys. Acta* **1843,** 2284–306

(2014).

250. Alonso, M. T. *et al.* Fura-2 antagonises calcium-induced calcium release. *Cell Biochem. Biophys.* **33,** 27–35 (2003).

251. Semenov, I. *et al.* Diffuse, non-polar electropermeabilization and reduced propidium uptake distinguish the effect of nanosecond electric pulses. *Biochim. Biophys. Acta* **1848,** 2118–25 (2015).

252. Wang, S. *et al.* Cardiac myocyte excitation by ultrashort high-field pulses. *Biophys. J.* **96,** 1640–8 (2009).

253. Engel, J. *et al.* Temperature Dependence of Ca2 + Wave Properties in Cardiomyocytes : Implications for the Mechanism of Autocatalytic Ca2 + Release in Wave Propagation. *Biophys. J.* **68,** 40–45 (1995).

254. Jaffe, L. F. Fast calcium waves. *Cell Calcium* **48,** 102–13 (2010).

255. Shigetomi, E. *et al.* TRPA1 channels regulate astrocyte resting calcium and inhibitory synapse efficacy through GAT-3. *Nat. Neurosci.* **15,** 70–80 (2012).

256. Hou, J. H. Dynamics in Biological Soft Materials. (2015).

257. Nesin, O. M. *et al.* Manipulation of cell volume and membrane pore comparison following single cell permeabilization with 60- and 600-ns electric pulses. *Biochim. Biophys. Acta* **1808,** 792–801 (2011).

258. Applegate, K. T. *et al.* plusTipTracker: Quantitative image analysis software for the measurement of microtubule dynamics. *J. Struct. Biol.* **176,** 168–84 (2011).

259. Osswald, M. *et al.* Brain tumour cells interconnect to a functional and resistant network. *Nature* **528,** 93–8 (2015).